TU Delft

Delft University of Technology

Measuring dynamic mechanical torque with fiber-optic sensors for geared wind turbines

Gutierrez Santiago, U.

DOI
10.4233/uuid:67ec64b8-c69e-4140-9019-cb33376f3622

Publication date
2025

Document Version
Final published version

Citation (APA)
Gutierrez Santiago, U. (2025). *Measuring dynamic mechanical torque with fiber-optic sensors for geared wind turbines*. [Dissertation (TU Delft), Delft University of Technology].
https://doi.org/10.4233/uuid:67ec64b8-c69e-4140-9019-cb33376f3622

Important note
To cite this publication, please use the final published version (if applicable).
Please check the document version above.

Copyright
Other than for strictly personal use, it is not permitted to download, forward or distribute the text or part of it, without the consent of the author(s) and/or copyright holder(s), unless the work is under an open content license such as Creative Commons.

Takedown policy
Please contact us and provide details if you believe this document breaches copyrights.
We will remove access to the work immediately and investigate your claim.

This work is downloaded from Delft University of Technology.
For technical reasons the number of authors shown on this cover page is limited to a maximum of 10.

Measuring dynamic mechanical torque with fiber-optic sensors for geared wind turbines

Unai Gutierrez Santiago

Measuring dynamic mechanical torque with fiber-optic sensors for geared wind turbines

Unai Gutierrez Santiago

Measuring dynamic mechanical torque with fiber-optic sensors for geared wind turbines

Measuring dynamic mechanical torque with fiber-optic sensors for geared wind turbines

Dissertation

for the purpose of obtaining the degree of doctor
at Delft University of Technology
by the authority of the Rector Magnificus prof. dr. ir. T.H.J.J. van der Hagen
chair of the Board of Doctorates
to be defended publicly on
Thursday, 27 March 2025 at 12:30 o'clock

by

Unai GUTIERREZ SANTIAGO

Ingeniero Industrial,
Euskal Herriko Unibertsitatea, Spain
born in Getxo, Spain.

This dissertation has been approved by the

promotor: Prof. dr. ir. J.W. van Wingerden
promotor: Dr. ir. H. Polinder

Composition of the doctoral committee:

Rector Magnificus,	chairperson
Prof. dr. ir. J.W. van Wingerden	Delft University of Technology, promotor
Dr. ir. H. Polinder	Delft University of Technology, promotor
Independent members:	
Prof. dr. Y. Guo,	Technical University of Denmark, DTU, Denmark
Prof. dr. S.J. Watson,	Delft University of Technology
Dr. ir. R.A.J. van Ostayen,	Delft University of Technology
Dr. C.L. Walters,	Delft University of Technology
Other members:	
Dr. J. Keller	National Renewable Energy Laboratory, USA

Dr. J. Keller has contributed to Chapters 4 and 6 of this dissertation as a coauthor.

The work in the dissertation was funded and supported by Gamesa Energy Transmission S.A.U., the gearbox business unit or Siemens Gamesa Renewable Energy.

Keywords: Wind, gearbox, fiber-optic strain, dynamic mechanical torque, planet load sharing, torque density, reliability.

Printed by: Ridderprint BV, The Netherlands.

Cover: Patrick Jakhari Sanders.

Style: TU Delft House Style, with modifications by Moritz Beller
`https://github.com/Inventitech/phd-thesis-template`

The author set this dissertation in LaTeX using the Libertinus and Inconsolata fonts.

ISBN 978-94-6522-060-4

An electronic version of this dissertation is available at
`http://repository.tudelft.nl/`.

Izan zirelako gara, garelako izango dira.
They were, and so, we are. We are, and so, they will be.
Basque proverb

For my family, thank you, this one is for you!!

Contents

Summary **ix**

Samenvatting **xi**

Acknowledgments **xiii**

1 Introduction **1**
- 1.1 Background . . . 3
- 1.2 Geared drivetrains . . . 5
- 1.3 Measuring torque in wind turbines . . . 9
- 1.4 The mesh load factor Kγ . . . 9
- 1.5 Fiber-optic strain sensors . . . 11
- 1.6 Goals of this dissertation . . . 12
- 1.7 Dissertation outline . . . 15

2 Input torque measurements for wind turbine gearboxes using fiber-optic strain sensors **19**
- 2.1 Introduction . . . 21
- 2.2 Background . . . 22
- 2.3 Torque estimation using peak-to-peak strain values . . . 28
- 2.4 Torque estimation using a coordinate transformation . . . 35
- 2.5 Discussion . . . 41
- 2.6 Conclusions . . . 45

3 Identification of operational deflection shapes of a wind turbine gearbox using fiber-optic strain sensors on a serial production end-of-line test bench **47**
- 3.1 Introduction . . . 49
- 3.2 Formulation of the subspace system identification method . . . 52
- 3.3 Experimental setup . . . 55
- 3.4 Identification of operational deflection shapes . . . 62
- 3.5 Conclusions . . . 72
- 3.6 Annex: Identification using signals from the second and third planetary stages . . . 73

4 Field validation of dynamic mechanical torque measurements using fiber-optic strain sensors for geared wind turbines **77**
- 4.1 Introduction . . . 79
- 4.2 Experimental setup . . . 80
- 4.3 Measuring dynamic mechanical torque with ring gear fiber-optic sensors . . . 88
- 4.4 Results . . . 95

4.5 Conclusions . . . 100

5 Experimental evaluation of the mesh load factor (K_γ) of a 6MW wind turbine gearbox 101
5.1 Introduction . . . 103
5.2 Experimental evaluation of the mesh load factor K_γ . . . 104
5.3 Discussion of results . . . 113
5.4 Conclusions . . . 114

6 Instantaneous mesh load factor (K_γ) measurements in a wind turbine gearbox using fiber-optic strain sensors 115
6.1 Introduction . . . 117
6.2 Experimental setup. . . . 118
6.3 Evaluation of the load mesh factor from ring gear outer surface strain . . . 120
6.4 Field validation campaign . . . 124
6.5 Conclusions . . . 127

7 Conclusion and recommendations 129
7.1 Conclusions and recommendations. . . . 131
7.2 Recommendations . . . 134

Bibliography 137

Glossary 150

Curriculum Vitæ 151

List of Publications 153

Summary

The devastating effects of climate change are becoming more evident each day. The time is now and we must spare no effort to revert the situation to ensure a sustainable and healthy future. Renewable energies play a vital role in the quest to reduce greenhouse gas emissions and limit the rise in global average temperature. Wind energy has become one of the leading renewable sources thanks to its remarkable progress in the last decades. Nevertheless, extraordinary efforts on all fronts are needed to meet the requirements for a net-zero scenario.

Many technological advancements have accelerated the staggering upscaling of wind turbine rotors and power ratings, significantly reducing the levelized energy cost from the wind (LCoE), and have allowed wind energy to become competitive against fossil fuels. Within the turbine, the drivetrain converts the mechanical energy in the rotor hub into electricity and makes an appreciable contribution to LCoE. Many wind turbine drivetrains use a gearbox to lower the overall capital cost of the drivetrain. The gearbox transfers the mechanical power from the rotor hub or the main shaft to the generator and increases rotational speed, lowering the torque. Ensuring gearboxes operate reliably remains a top priority because gearbox failures cause extended downtime with costly repairs and contribute appreciably to the turbine operation and maintenance costs.

The massive increase in torque associated with the up-scaling in rotor diameters, coupled with the pressure to lower costs and the size constraints, have translated into higher torque density demands for wind turbine gearboxes. A trend has emerged in new gearbox architectures towards more planetary stages and more planets per stage. One of the main challenges of next-generation gearbox designs is sharing the load evenly between the high number of planets. Maintaining or improving gearbox reliability with the increasing torque density demands is proving challenging. Accurate knowledge of the mechanical loads of wind turbine gearboxes has become essential for modern highly loaded gearbox designs with significant dynamic interactions.

The main contribution of this thesis is to develop a method to measure dynamic mechanical torque in geared wind turbines. A novel method based on strain measurements on the outer surface of the static first-stage ring gear is proposed. This approach eliminates the main limitation of conventional methods, which involve measuring the strain of rotating components and consequently require complex and costly data transfer mechanisms, such as wireless transmission or slip rings. Optical fiber strain sensors based on fiber Bragg gratings (FBGs) are used due to their advantages compared to electric resistance strain gauges, including a higher signal-to-noise ratio, immunity to electromagnetic interference, and a more straightforward installation process, as multiple strain sensors can be accommodated within a single fiber.

Three experimental campaigns were conducted to achieve the primary goal of this thesis. Initially, a 6 MW gearbox equipped with 54 fiber-optic strain sensors was tested in a back-to-back gearbox test bench to evaluate the capabilities of fiber-optic strain sensors

in measuring the deformations caused on the outer surface of the ring gear by the planet passages. Two signal processing strategies were investigated to correlate the strain signals measured on the static ring gear with dynamic mechanical torque. The first strategy is based on the peak-to-peak strain values associated with the planet gear passage events. The second strategy combines the strain signals from different sensors using a Coleman coordinate transformation and tracks the magnitude of the harmonic component corresponding to the number of planets. In a second test campaign, the measurement setup was extended to 129 fiber-optic strain sensors distributed around the ring gears of the three planetary stages of a state-of-the-art gearbox. Operational deflection shapes were identified by applying data-driven methods to the strain signals. The contribution of the deflection shapes produced by the passing of planets and their harmonics was found to be controlled by the amount of input torque applied to the gearbox. Finally, an extensive field experiment was conducted on a 2 MW wind turbine at the National Renewable Energy Laboratory's Flatirons Campus to evaluate the accuracy of the torque measurements and research how the turbine operating conditions affect the quality of the torque measurements. These experiments have advanced the technology readiness level and demonstrated the accuracy and robustness of the proposed method, which is now deemed ready for commercial implementation.

The proposed measurement system can also be used to measure additional gearbox performance features. By comparing the deformations caused by the different planets, it is possible to evaluate the planet-load sharing behavior. The fiber optical strain measurements from the initial test bench experiments provided equivalent planet load-sharing results compared to the traditional method based on strain gauges located in the roots of the sun gear teeth. Additional fiber-optic strain sensors with an enhanced spacing definition were deployed during the field validation campaign on the 2-MW wind turbine. An instantaneous evaluation of the mesh load factor was achieved by defining the number of sensors as an integer multiple of the number of planets. As a result, the planet load-sharing behavior was investigated across a wide range of turbine operating conditions.

An accurate measurement of the input torque throughout the service history of every gearbox in a fleet would enable an improved assessment of the consumed fatigue life. This is important because the loading conditions are site-specific, and allowing an individual evaluation of each gearbox can lead to a better understanding of current gearbox failure modes. Future research is needed to understand the effect of torque fluctuations and investigate the possibility of improving gearbox loading through advanced wind turbine controllers. This would facilitate future gearbox design improvements, which would, in turn, lead to higher reliability and lower LCoE.

Samenvatting

De verwoestende effecten van klimaatverandering worden met de dag duidelijker. Het is de hoogste tijd om alles in het werk stellen om de situatie te veranderen en een duurzame en gezonde toekomst te garanderen. Hernieuwbare energie speelt een cruciale rol bij het verminderen van de uitstoot van broeikasgassen om zo de gemiddelde stijging van de temperatuur op aarde te beperken. Windenergie is een van de belangrijkste hernieuwbare bronnen geworden dankzij de opmerkelijke vooruitgang in de afgelopen decennia. Toch zijn er op alle fronten buitengewone inspanningen nodig om te voldoen aan de vereisten voor een klimaatneutraal scenario.

Technologische ontwikkelingen hebben de schaalvergroting van windturbines aanzienlijk versneld, en hebben de kosten van wind aanzienlijk doen dalen zodat windenergie beter concurreren met fossiele brandstoffen. In de turbine wordt mechanische energie via de aandrijflijn omgezet in elektrische energie en levert zo een aanzienlijke bijdrage aan de gemiddelde kosten van windenergie. Veel aandrijflijnen van windturbines maken gebruik van een tandwielkast om de totale kapitaalkosten van de aandrijflijn te verlagen. De tandwielkast brengt het mechanische vermogen van de rotornaaf over naar de generator en verhoogt de rotatiesnelheid, waardoor het aandrijfkoppel daalt. Het blijft een topprioriteit om er voor te zorgen dat tandwielkasten betrouwbaar werken omdat defecten aan de tandwielkasten leiden tot lange stilstandtijden met dure reparaties en aanzienlijke bijdragen aan de bedrijfs- en onderhoudskosten van de turbine.

De enorme toename in aandrijfkoppel die gepaard gaat met het vergroten van de rotordiameter, in combinatie met de druk om de kosten te verlagen en de beperkte afmetingen, hebben geleid tot hogere eisen aan de koppeldichtheid van tandwielkasten voor windturbines. Er is een trend ontstaan in nieuwe tandwielkast ontwerpen naar meer planetaire trappen en meer planeetwielen per trap. Een van de belangrijkste uitdagingen van de volgende generatie tandwielkastontwerpen is het gelijkmatig verdelen van de belasting over het grote aantal planeetwielen. Het blijkt een uitdaging om de betrouwbaarheid van de tandwielkast te handhaven of te verbeteren met het oog op de toenemende koppeldichtheid. Nauwkeurige kennis van de mechanische belasting van tandwielkasten voor windturbines is essentieel geworden voor moderne, zwaar belaste tandwielkastontwerpen met aanzienlijke dynamische interacties.

De belangrijkste bijdrage van dit proefschrift is het ontwikkelen van een methode voor het meten van dynamisch mechanisch koppel in windturbines met tandwieloverbrenging. Er wordt een nieuwe methode voorgesteld die gebaseerd is op rekmetingen aan het buitenoppervlak van het statische ringtandwiel van de eerste trap. Deze benadering elimineert de belangrijkste beperking van conventionele methoden, waarbij de spanning van roterende componenten wordt gemeten en dus complexe en kostbare mechanismen voor gegevensoverdracht nodig zijn, zoals draadloze transmissie of sleepringen. Optische vezelsensoren op basis van fiber Bragg roosters (FBG's) worden gebruikt vanwege hun voordelen ten opzichte van elektrische weerstandsrekmeters, waaronder een hogere

signaal-ruisverhouding, immuniteit voor elektromagnetische interferentie en een eenvoudiger installatieproces doordat er meerdere reksensoren in één vezel passen.

Er werden drie experimentele campagnes uitgevoerd om het primaire doel van dit proefschrift te bereiken. Allereerst, werd een 6 MW tandwielkast uitgerust met 54 optische vezelsensoren en getest in een back-to-back tandwielkast testbank om de mogelijkheden van optische vezelsensoren voor het meten van de vervormingen aan het buitenoppervlak van de ringtandwielkast te evalueren. Twee signaalverwerkingsstrategieën werden onderzocht om de reksignalen gemeten op de statische tandring te correleren met het dynamische mechanische koppel. De eerste strategie is gebaseerd op de piek-tot-piek vervormingswaarden die geassocieerd zijn met de passage van de planeetwielen. De tweede strategie combineert de reksignalen van verschillende sensoren met behulp van een Coleman coördinatentransformatie en volgt de grootte van de harmonische component die overeenkomt met het aantal planeten. In een tweede testcampagne werd de meetopstelling uitgebreid met 129 optische vezelsensoren verdeeld over de ringtandwielen van de drie planetaire trappen. Operationele doorbuigingsvormen werden geïdentificeerd door datagedreven methoden toe te passen op de reksignalen. De bijdrage van de doorbuigingsvormen geproduceerd door het passeren van planeten en hun harmonischen bleek gecontroleerd te worden door de hoeveelheid ingaand koppel dat op de tandwielkast wordt aangebracht. Tot slot werd er een uitgebreid veldexperiment uitgevoerd op een 2 MW windturbine op de Flatirons Campus van het National Renewable Energy Laboratory om de nauwkeurigheid van de koppelmetingen te evalueren en om te onderzoeken hoe de bedrijfsomstandigheden van de turbine de kwaliteit van de koppelmetingen beïnvloeden. Deze experimenten hebben het technologieniveau verhoogd en de nauwkeurigheid en robuustheid van de voorgestelde methode aangetoond, zodat deze nu klaar wordt geacht voor commerciële inzet.

Het voorgestelde meetsysteem kan ook worden gebruikt om aanvullende prestatiekenmerken van de tandwielkast te meten. Door de vervormingen veroorzaakt door de verschillende planeten te vergelijken, is het mogelijk om de verdeling van belastingen over de planeetwielen te evalueren. De vezeloptische vervormingsmetingen van de eerste experimenten leverden gelijkwaardige resultaten op in vergelijking met de traditionele methode gebaseerd op rekmetingen van de zonnetandwielen. Tijdens de veldvalidatiecampagne op de 2-MW windturbine werden extra optische vezelsensoren met een verbeterde afstandsdefinitie ingezet. Door het aantal sensoren te definiëren als een geheel veelvoud van het aantal planeetwielen werd een onmiddellijke evaluatie van de belastingsfactor bereikt. Hierdoor werd het belastingsgedrag van de planeetwielen onderzocht over een breed bereik van bedrijfsomstandigheden van de turbine.

Een nauwkeurige meting van het ingangskoppel gedurende de hele gebruiksgeschiedenis van een tandwielkast zou een betere beoordeling van de verbruikte vermoeiingslevensduur mogelijk maken. Dit is belangrijk omdat de belastingsomstandigheden locatiespecifiek zijn en een individuele evaluatie van elke tandwielkast kan leiden tot een beter begrip van de huidige faalwijzen van tandwielkasten. Verder onderzoek is nodig om het effect van koppelfluctuaties te begrijpen en de mogelijkheid te onderzoeken om de belasting van de tandwielkast te verbeteren door middel van geavanceerde windturbineregelaars. Dit zou toekomstige verbeteringen aan het ontwerp van de tandwielkast mogelijk maken, wat weer zou leiden tot een hogere betrouwbaarheid en lagere kosten van windenergie.

Acknowledgments

Over the past seven years, I've pursued a PhD in Mechanical Engineering at TU Delft, part-time with my "regular" job and remotely from Bilbao. Reflecting on these years brings a big smile to my face. Writing journal papers has proven to be far more challenging than I anticipated. Yet, it has been such a rewarding journey that my overwhelming feeling is one of deep gratitude.

When I finished my Master's degree many many years ago, I had a sense of needing to rush into industry to do "real" hands-on engineering. I moved to England and found a job testing plastic gears, where I could design, inject mold, and test them to failure. Our test gears had a pitch diameter of 60 mm and weighed just a few grams. After several years, when the lack of vitamin D kicked in, homesickness prompted my return. It was then that I started my journey in wind energy in the gearbox business unit of the former Gamesa. My first assignment was testing four 2 MW gearboxes weighing approximately 14 tonnes. Since then, I have tested countless gearbox designs on test benches and wind turbines in multiple locations, including Spain, Belgium, Germany, China, India, USA, and Denmark. Over time, the desire to dig deeper and understand some of the experimental observations grew, and a Ph.D. seemed like the perfect framework for doing so.

I consider myself a very lucky person. One of my most remarkable "lucky moments" was meeting Jan-Willem on a very rainy day back in the winter of 2018. Jan-Willem, your passion for science is stunning and inspiring. You never hesitated to support my research proposal, even without prior gearbox experience. Your brilliant mind, kindness, and support make you a truly special person. Being part of your research group has been a great honor for me. During this time, I have also been incredibly fortunate to have Henk as my second promotor. Thank you, Henk, for consistently challenging my intuitions with every new experimental finding; you have been an excellent guide in critical thinking. I will definitely miss your direct and sometimes ruthless Dutch sense of humor. Another pivotal person who helped me accomplish this degree is my manager at Siemens Gamesa Alfredo, who not only understood my bold idea of doing a PhD part-time remotely with a Dutch university but later convinced the director of the gearbox business unit, José Luis, to support it. It has been amazing and I will be forever in your debt.

I started my PhD journey with the broad title of data-driven gearbox modeling. While I was still exploring research directions and potential contributions, Jan-Willem introduced me to a small Dutch company specializing in fiber-optic sensing. This marked my first encounter with this fantastic technology. In 2019, we performed the first "proof-of-concept" test, from then Sensing360 has always remained enthusiastic about applying this technology to wind turbine gearboxes. Thank you, Eric, Georgo, Mats, Sandra, and Gertjan, for your continued support in all subsequent test campaigns.

Testing wind turbine gearboxes is definitely a collaborative effort that requires the dedication and support of many people. The help of my teammates in the gearbox validation section, Iñaki, Dani, Martín, Santi, and Javi, has been invaluable. Thanks again

for all your help with sensor installation, test execution, and data logging throughout the various test campaigns. Sometimes, we were under very strange circumstances, such as when we had to carry on testing in the middle of the COVID-19 pandemic. The gearbox test benches have become highly complex and need constant "encouragement" from our test bench engineers and technicians to run smoothly. I am also thankful to my colleagues in the engineering department for the fruitful discussions on design, calculation, and manufacturing processes.

Another one of those outstanding lucky moments was receiving a collaboration proposal from Jon at the National Renewable Energy Laboratory (NREL) after reviewing our first journal paper. Thank you so much, Jon, for enabling the field validation campaign and hosting me on the beautiful Flatirons campus in Colorado. Jerry, Brian, and Anna, thanks for your support during the up-tower sensor installation and for looking after the instrumentation throughout the experiment. The G97 is the turbine with the best music and food I have ever worked on! Jason and Scott, thanks for helping with the data acquisition process, and Nick, thanks for your simulation work. Getting the good old Gamesa turbine working was not easy and could not have been accomplished without the support of the US SGRE service team. Visiting the US with my family created some of the best memories, highlighted by an epic road trip and many fun activities around Boulder, like slacklining in North Boulder Park or climbing the third Flatiron at night!

By far, the most rewarding and enjoyable part of my PhD has been meeting so many incredible people along the way. Interacting with fellow PhD candidates, post-docs, and professors in the Delft Center for Systems and Control has been amazing. Thank you, Amr, for all the great moments we shared and for introducing me to Syrian sweets! Thanks for agreeing to be my paranymph hermano; I am sure you will succeed in the remainder of your PhD. Mees, I am sorry I could never pronounce your name correctly; thanks for helping me with the second journal paper when I needed it the most. Working with you and the undergraduate students on the small wind turbine competition was great fun. To the ever-growing super-motivated climbing and slacklining crew: Jonas, David, Emanuel, Marcus, Maarten, Tim, Alex, Claudia, Dani, Frida... It was definitely worth being told off for stepping on the mattress at Delfts Bleau, and highlining at Amsterdam was unforgettable! You are always welcome on the cliffs around Bilbao. I look forward to organizing a deep-water solo trip to Mallorca soon. Daan, thanks for your help with the Dutch translation. Atin, Daniel, Sebastiaan, Marion, Jesse, Bert, Bart, Joeri, Livia, Jean, Dimitris, Kim, Manon, Riccardo, Sander, Twan, Rogier, Guido, Mateo... the list is immense, thank you all! The amount of talent in the group is astronomical. After my sister, you are the most intelligent people I know; please go out there and do something remarkable! Of course, a special mention is needed for the staff who make it all run smoothly and were always willing to help me: Marieke, Heleen, Kiran, Mascha, Francy, and Sandra. Thank you all!

During my trips to Delft, I stayed on Avontuur, a historic boat located in the heart of Rotterdam's city center. Premala and Alexandra, thanks for hosting me and making me feel so welcome. Thanks for all your wise words, encouragement, and inspiration. Never a dull moment aboard, it was great fun meeting fellow travelers, including some hairy moments like when I got stranded in February 2022 by storm Eunice, the wind blew off a roof slate, and a tree fell onto the neighbor's boat. I will miss playing "Mensch ärgere dich nicht" by the fire.

For my dedication page at the beginning of the dissertation, I chose the Basque proverb "Izan zirelako gara, garelako izango dira," which loosely translates to "They were, and so, we are. We are, and so, they will be." To me, it beautifully conveys my feeling of gratitude to past generations and the connection and responsibility towards our descendants. Ama, Aita, I surely wouldn't be here without you. Thank you for providing me with all the opportunities and the freedom to choose my own path. Combining the PhD with other obligations was a lot of hard work and plenty stressful at times. I have given it my best, and it was only possible to do so because of Edurne. Thanks for taking care of everything while I was away. You have supported me unconditionally during all this time, the long hours, catching up on the weekends, and all the trips. I definitely could not have done it without you. My only regret now, is that to undertake the PhD, I had to take time away from you, Ander, and Iraide. I hope to be able to make it up to you! The doctoral degree may have my name, but it no doubt belongs to you. Thank you.

Unai
Berango, January 2025

1

Introduction

The devastating effects of climate change are becoming more evident each day. We are running out of time, and our best collective effort is needed to revert the situation and ensure a sustainable and healthy future. Renewable energies are a key enabler for such a future. This chapter presents the remarkable progress attained by wind energy in the last decades and the extraordinary growth required to meet future net-zero scenarios. Wind turbine technology is rapidly evolving towards larger rotors and power ratings, which have resulted in much higher torque density demands for the drivetrain in general and the gearbox in particular. Maintaining or even improving gearbox reliability with increasing torque density demands is proving to be challenging. Accurate knowledge of the mechanical loads of wind turbine gearboxes has become essential for modern highly loaded gearbox designs with significant dynamic interactions. The contribution of this dissertation can be summarized by its goal: to develop a method to measure dynamic mechanical torque in geared wind turbines.

1

Isaac Newton (1643-1727), was the first person to decompose white light and name the spectral colors. In 1671, he introduced the term “spectrum” while describing his optical experiments. Newton noticed that when a narrow beam of sunlight hits a glass prism at an angle, it splits into different-colored bands. He suggested that light is made up of particles of different colors, each moving at different speeds in transparent matter. Red light, which moves faster than violet in glass, bends less sharply, creating a spectrum of colors. Newton initially identified six colors: red, orange, yellow, green, blue, and violet. He later added indigo to make seven, a number he considered perfect, connecting the colors to musical notes, known objects in the Solar System, and the days of the week. Newton was not able to measure the wavelength of the light, but his experiments were repeated contemporarily to estimate wavelengths where the boundaries of his color terms lay. In this dissertation, fiber-optic strain sensors have been used, which reflect narrow bands of wavelength from a full spectrum of light. The working principle of these sensors has inspired the association of each of the seven chapters of the thesis with a color from the so-called Newton’s rainbow. The first color, arranged by ascending wavelength, is violet, with wavelengths from 380 nm to 420 nm.

1.1 Background

The scientific community has long warned us regarding the catastrophic impact of human activities on Earth. The frightening effects of climate change are becoming ever more evident. António Guterres, the Secretary-General of the United Nations, summarized these effects accurately in a letter addressed to his great-great-granddaughter, dated April 20, 2023: "relentless temperature rise, deadly droughts and famines, melting glaciers and rising seas. Communities ravaged and erased by floods and wildfires. Extinction and biodiversity loss on an epic scale". Now is the moment, and it is our responsibility to collectively ensure breathable air, better health, sustainable food systems, clean water, and robust, circular economies for future generations. António Guterres envisioned an alternative path for such a desirable outcome as "a future powered by renewable energy and high-quality green jobs".

1.1.1 The evolution and future of wind energy

Renewable energy is derived from natural unlimited sources, such as the sun, tides, and wind, in contrast to finite sources, like coal, natural gas, and oil. It can be used to generate electricity, for heating and cooling, and for transportation. The growth of wind energy in the last decades has been truly remarkable. The Global Wind Energy Council (GWEC) reported a "record-breaking" 116.6 GW of new wind energy capacity installed in 2023, bringing the worldwide cumulative wind power capacity to 1021 GW [1]. This implies that the installed capacity has more than tripled in the last 10 years from a global capacity of 318.1 GW in 2013 [2], and a staggering 25-fold increase in 20 years from the 39.4 GW in 2001 [3]. The share of electricity produced by wind energy worldwide varies significantly depending on the country. Denmark leads with 57.7 %, while countries like the United States of America and China have shares of 10 % and 9.4 %, respectively [1]. In the European Union (EU) wind farms generated 466 TWh of electricity in 2023, which accounted for 19 % of the EU's electricity demand [4]. Overall, in the year 2023, wind energy supplied 7.8 % of the electricity generated worldwide [5]. The progress attained by wind energy to date is truly remarkable, and the projected growth for the coming years and decades is even larger. In 2022, the International Renewable Energy Agency (IRENA) and International Energy Agency (IEA) published a road map for the energy sector to become net-zero by 2050, to limit the rise in global temperatures to 1.5℃ [6]. According to these master plans, solar photovoltaic (PV) and wind shall become the leading sources of electricity globally before 2030. In 2050, combining wind and solar with bioenergy, hydroelectricity, and geothermal, renewables will provide two-thirds of energy use for a net-zero scenario. The worldwide annual capacity additions of wind energy should reach 390 GW by 2030, 310 GW onshore and 80 GW offshore. That means increasing the yearly installations more than three times compared to the ones accomplished in 2023 [6].

1.1.2 Turbine technology trends

To facilitate such rapid growth, the main focus of industry and academia has been lowering the levelized cost of energy from wind (LCoE) [7]. This push to lower the LCoE has resulted in a race from wind turbine manufacturers to increase the rotor diameter, power rating, and hub height of wind turbines. Wind turbines are generally classified into land-based and offshore because this has significant implications in the design requirements. The

1

size evolution in offshore turbines has been even more dramatic because they have less stringent logistic constraints [8]. Figure 1.1 illustrates the extraordinary pace of upscaling of wind turbines. The trend to increase power ratings, rotor diameter, and hub heights can be understood from a wind turbine's fundamental power generation equation [9]:

$$P = \frac{1}{2}\rho A v^3 C_p, \tag{1.1}$$

where ρ is the air density, A is the area swept by the rotor, v is the wind speed and C_p is the power coefficient. Power is proportional to the swept area and, therefore, grows with the square of the rotor diameter. Increasing the hub height reduces the influence of surface friction on the wind conditions witnessed by the rotor, allowing wind turbines to operate in higher-quality resource regimes where wind velocities are higher. There are several reasons for the increase in the rotor diameter of wind turbines. Larger rotors capture more energy. The increase in energy captured by the rotor is bigger than the increase in overall turbine costs because blade lengths can be increased while many other costs remain fixed, generally leading to lower LCoE in larger turbines. More powerful turbines allow fewer turbine installations for a given power plant capacity, lower balance-of-system costs, and fewer moving parts, therefore enhancing the reliability of the wind plant. In addition, increasing the size of the rotor relative to the generator rating allows for lowering the rated wind speed and operating more frequently at full power, resulting in a higher capacity factor.

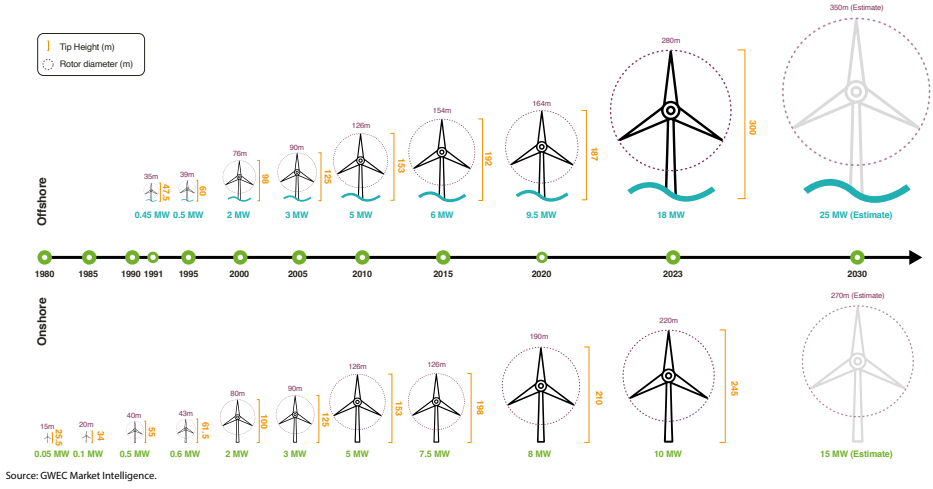

Figure 1.1: Turbine size trend from 1980 to 2030, source GWEC [1].

This rate of development is unprecedented in any other industry or engineering application. Ensuring turbines operate in a reliable manner over their entire service life remains a top priority [10]. The technology race to upscale new turbines requires expensive investments in R&D, and entails high risks jeopardizing a sustainable supply chain. In

this context, several OEMs have faced quality issues with alarming financial consequences due to warranty provisions over the last five years [11].

1.2 Geared drivetrains

The wind turbine drivetrain converts mechanical power to electrical power and transmits the rotor loads to the bedplate and tower [12]. Therefore, it includes all the components downstream of the rotor hub associated with power conversion, i.e., main bearing, shafts, generator, and power converter, and makes an appreciable contribution to the capital expenditure of the turbine [13]. Many wind turbine drivetrains use a gearbox to lower the overall capital cost of the drivetrain. This has led to two main drivetrain configurations, geared drivetrains and drivetrains without a gearbox, which are widely referred to as direct drive. The benefits and drawbacks of both configurations have been frequently addressed in literature [12, 14–18]. Up to this point, there has been no convergence towards a single best wind turbine drivetrain, and both configurations co-exist in commercial turbines. Geared turbines with a doubly-feed induction generator (DFIG) have dominated the global onshore market below 3 MW rated power output [19]. In the offshore wind energy market, leading manufacturers have favored either a direct-drive permanent-magnet synchronous generator (DD-PMSG) or a medium-speed gearbox coupled to a compact PMSG (MS-PMSG) [20]. According to the 2023 Global Wind Turbines Technology Trends report from Wood Mackenzie, the direct-drive market share of drivetrains connected to the grid in 2023 was 8 %, geared drivetrains with a high-speed generator accounted for 72 % and the remaining 20 % were medium-speed geared drivetrains with PMSG [21]. In the coming decade, direct-drive drivetrains are forecasted to maintain their market share between 8-10 %, while medium-speed geared drives will gradually increase their share up to 36 % at 2032 [21].

Reliability, in the context of this dissertation and specifically regarding wind turbines and gearboxes, is defined as the probability of performing the intended function without failure under specified operational conditions [22]. For wind turbines, the primary function is producing electricity, while for gearboxes, it is to transfer the power generated by the wind from the rotor hub or main shaft to the generator, providing the necessary increase in rotational speed. Several metrics quantify reliability, including failure rates, stop rates, downtime, and lost production. Ensuring wind turbine gearbox reliability remains a top priority because gearbox failures cause long downtime with costly repairs and contribute appreciably to the turbine operation and maintenance costs [10, 23, 24]. Thanks to internationally recognized gearbox wind turbine design standards like IEC 61400-4 and AGMA 6006 and collaborative efforts like the Drivetrain Reliability Collaborative between turbine manufacturers, gearbox designers, bearing suppliers and research institutions like the National Renewable Energy Laboratory (NREL) and Argonne National Laboratory, average annual gearbox failure rates for the U.S. land-based fleet have dropped from 5 % to 10 % 20 years ago [25] to 2.5 % more recently [26]. Yet, there is room for improvement because gearboxes still generally do not reach their desired design life [27]. These standards have placed greater rigor on the design and gearbox verification process, including the effects of rotor nontorque loads [28], transient events [29, 30], and electrical currents [31].

Torque is the critical sizing factor for wind turbine gearboxes and drives their dimensions and weight [32]. If we assume a limitation to maintain the tip speed of the blades

1

constant, the rotational speed decreases linearly with the rotor diameter, and therefore from Equation (1.1), rotor torque grows with the cubic exponential of the rotor diameter:

$$T \propto \rho R^3 v^3 C_p, \tag{1.2}$$

where R is the rotor radius.

NREL publishes the yearly average power rating and rotor diameter values of turbines installed in the United States [33–35]. For each year the associated average rotor torque values can be derived from Equation (1.2), showing that the rotor torque of the installed turbines has increased more than 3 times in a decade[36]. The vast increase in torque associated with the upscaling in rotor diameters, coupled with the pressure to lower costs and the size constraints due to handling and logistic limitations, have translated into higher torque density demands for wind turbine gearboxes. Thanks to multiple technological innovations, torque densities have experienced a remarkable 2.5-fold increase over the past decade [21], with values of 200 Nm/kg now regarded as state-of-the-art in the industry [37–39]. For such high torque ratings and torque density values, a trend has emerged in new gearbox architectures towards more planetary stages and more planets per stage. In wind turbines with a power rating of up to 2.5 MW, the most widely used gearbox architecture is shown in Figure 1.2 and comprises a single planetary stage and two parallel gear stages [40]. An example of this gearbox architecture is the G97 2MW gearbox shown in Figure 1.3, which was used for the experiments presented in Chapter 4 and Chapter 6 of this dissertation. In the power range from approximately 2 MW to 6 MW, gearboxes with two planetary stages and a single parallel stage have become mainstream. Figure 1.5 shows the gearbox architecture of a Siemens Gamesa Renewable Energy (SGRE) 5X gearbox employed in turbines with rotor diameters up to 170 meters and rated powers up to 6.6 MW. This gearbox was used in the experiments presented in Chapter 2. The field assembly process where the gearbox, the main shaft and the rotor hub are lifted into the nacelle is shown in Figure 1.4. For even higher power ratings, gearboxes with three planetary stages like the one depicted in Figure 1.6 are expected to become dominant. This gearbox architecture was tested in Chapter 3. Due to the high torque increase in these power ratings, the trend is to employ more planets in the input stages. Because of limitations in outer diameter, the space available for planet bearings has decreased to a point where journal bearings must be adopted, as there is not enough space for roller element bearings [12].

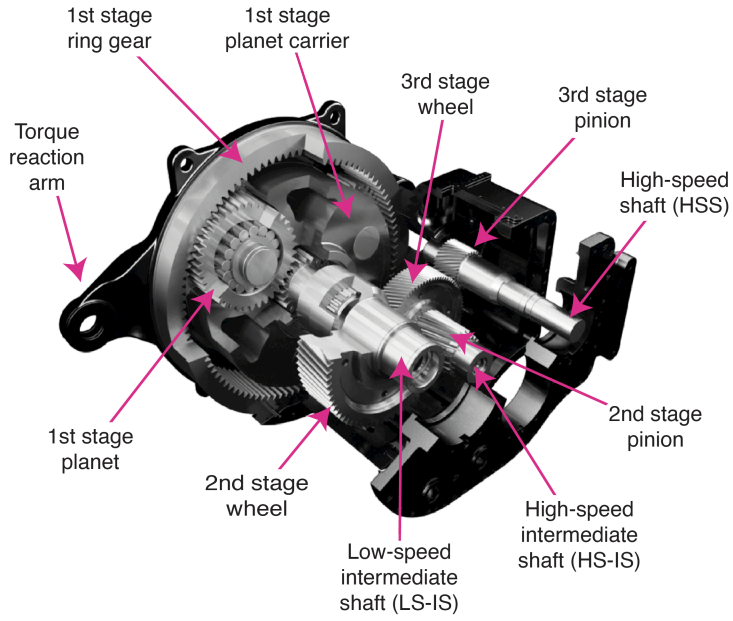

Figure 1.2: Exploded view drawing of a 3-stage gearbox with one planetary stage (PHH architecture). Adapted from Gamesa Gearbox (`https://www.gamesagearbox.com/wind-technology/`.

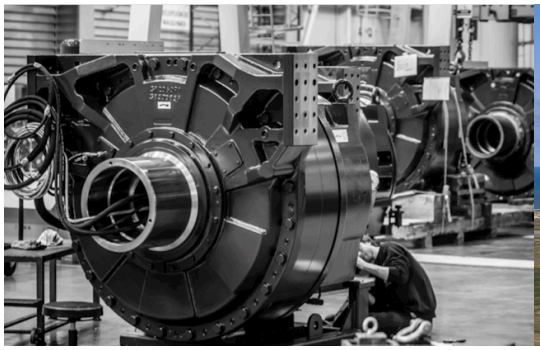

Figure 1.3: G97 gearbox in its final assembly stage.

Figure 1.4: SGRE 5X - 170 drivetrain installation in prototype turbine.

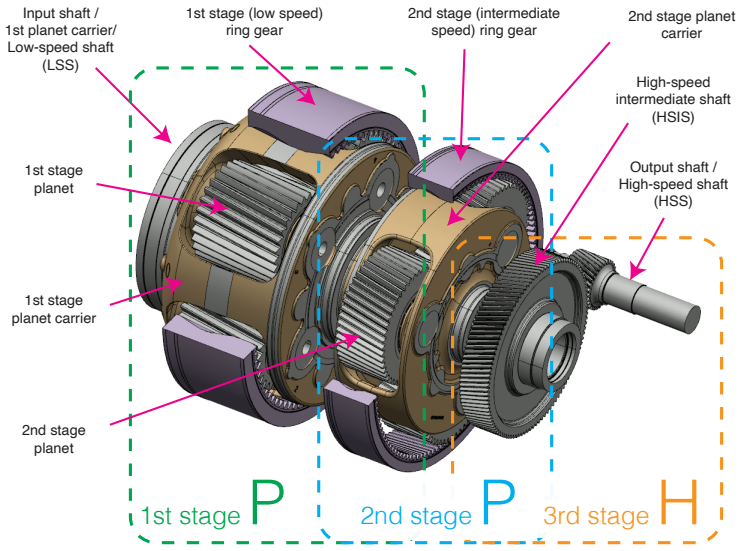

Figure 1.5: Assembly drawing of shafts and gears from the 3-stage Siemens Gamesa Renewable Energy gearbox (PPH configuration).

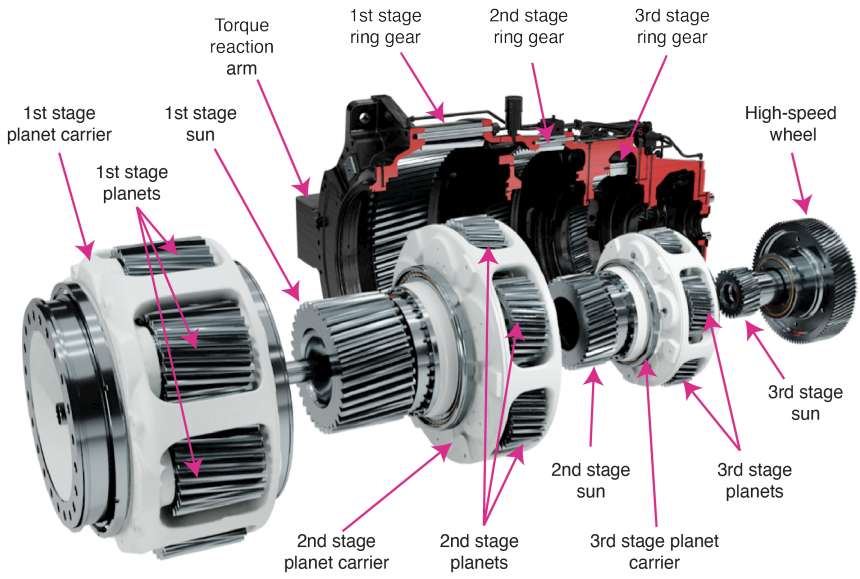

Figure 1.6: Exploded view representation of a 4-stage gearbox with three planetary stages (PPPH). Adapted from Gamesa Gearbox (`https://www.gamesagearbox.com/wind-technology/`

1.3 Measuring torque in wind turbines

Accurate knowledge of the dynamic mechanical torque in wind turbine gearboxes is crucial to meet the increased torque density demands and additional requirements, such as more significant dynamic interactions and stricter noise regulations, while maintaining or even enhancing their reliability. Dynamic mechanical torque measurements of every gearbox in a fleet can enhance drivetrain usage monitoring because the consumed fatigue life can be assessed more precisely using the measured torque values throughout their entire commercial operation. The wind turbine controller can also potentially use dynamic torque measurements to improve wind turbine control and reduce torque oscillations (i.e., torsional damping). Additionally, dynamic mechanical torque measurements can be used to quantify drivetrain efficiency. Unfortunately, sensors that provide detailed direct load measurements of the turbine during commercial operation are generally not available [41]. It is feasible to estimate the mechanical gearbox torque from the electric currents in the generator and the power converter. However, this process necessitates assumptions about the variable efficiencies of the gearbox and generator, which are generally unknown and dependent on the applied torque. Additionally, other operating conditions, such as temperature, can further increase the uncertainty of these measurements. Typically, this information is only available in commercial wind turbines through the supervisory control and data acquisition (SCADA) system. Due to the limited frequency capability of SCADA, it cannot capture the torque fluctuations induced by dynamic wind turbine operations [30, 42–44]. This limitation is especially critical during high-load, highly dynamic events, such as emergency stops and low-voltage ride-throughs, when the generator must handle brief periods of reduced electric network voltage. The conventional method to make a direct measurement of dynamic mechanical torque is based on bonding strain gauges to a rotating drive shaft. The strain gauges convert the torsional deformation caused by the torque into a change in electrical resistance. Transferring the resulting signal from the rotating shaft to a stationary data logging system and powering the data acquisition devices is difficult and costly. In wind turbines, the main-shaft's torsional deformation is also small because of its high stiffness, which typically results in a low signal-to-noise ratio. The torsional deformation of the gearbox output shaft is higher, but this shaft can require special provisions to access the shaft [30]. These drawbacks have limited the use of such measurements to laboratory environments [28], validation and certification of experimental wind turbines [45], and troubleshooting exercises [46]. Other researchers have focused on indirect techniques or so-called virtual sensors where a model of the system is combined with data from sensors in other locations of the turbine to obtain an estimate of dynamic mechanical torque [47–53].

1.4 The mesh load factor Kγ

As presented in Section 1.2, the increase in torque density of wind turbine drivetrains has resulted in a trend to increase the number of planetary stages and the number of planet gears per stage. One of the main challenges of next-generation gearbox designs is sharing the load evenly between the high number of planets, especially when subjected to rotor nontorque loads and in the presence of any manufacturing errors [54]. The load-sharing behavior of planetary gears has been extensively studied the literature. Kahraman et al. re-

searched its dependency on manufacturing errors and the associated dynamic effects [55] and presented an experimental study in [56]. Singh proposed an analytical formulation for the relationship between planet load sharing behavior and positional errors [57]. These studies are based on smaller module gears for automotive or helicopter applications. Guo and Keller generalized this analytical formulation for wind turbine gearboxes with a three-planet, floating epicyclic configuration [28, 54]. Little evidence can be found in the literature for a higher number of planets. New analytical tools are needed to predict the load-sharing behavior in modern wind turbine gearboxes. These tools need to be demonstrated and validated through experimental evaluation.

The gear rating standard ISO 6336-1 [58] defines the mesh load factor, K_γ, as the quotient between the highest load carried by a single planet divided by the average load of all planets. Within the design requirements for wind turbine gearboxes, the standard IEC 61400–4 [59] sets K_γ as a function of the number of planets, see Table 1.1.

Table 1.1: Mesh load factor K_γ values for planetary stages given by the standard IEC 61400-4 according to their number of planets.

Number of planets	3	4	5	6	7
Mesh load factor K_γ	1.10	1.25	1.35	1.44	1.47

For a high number of planets, the mesh load factors presented in Table 1.1 are conservative and would lead to gearbox designs with poor torque density values. The standard allows using lower mesh load factors if they are experimentally demonstrated by gear tooth root strain gauge measurements. Examples of practical implementations of such measurement systems can be found in [60–62]. Strain gauges must be placed in a root of the rotating sun gear to extract planet load-sharing behavior, which requires either a slip ring or telemetry system and significant planning and installation. Each time the instrumented sun tooth engages with a planet, the mesh intensity can be evaluated as a weighted sum of all the strains measured along the root. The instrumented tooth will mesh with all the planets because the sun rotates faster than the carrier. However, the mesh events do not coincide in time. Therefore, the effect of the torque fluctuations must be addressed, and only an average value of the mesh load factor can be obtained. A more elaborate way of evaluating the mesh load factor has been used to overcome this limitation, based on planet bearing loads [28]; however, this method is complex and requires modifications to the gearbox and planet bearings.

The mesh load factor, K_γ, directly impacts gear rating and life calculations. A lower value of K_γ implies sharing the load more evenly between the planet gears. This allows a more optimized gearbox design, and therefore significant improvements in torque density are expected. Furthermore, currently, the results obtained from a single prototype are extrapolated to the entire fleet, assuming that the manufacturing class of the gears and the accuracy of the serial production gearbox components are controlled so that their effect on planet load sharing is negligible compared to the instrumented prototype.

1.5 Fiber-optic strain sensors

Fiber-optic sensors (FOS) can measure several physical quantities using optical fibers as the sensing element by exploiting changes in the reflected light. There are several fiber optic sensing technologies available, which are generally divided into two categories: discrete and distributed sensors. Distributed sensors measure over the entire length of the optical fiber whereas discrete sensors provide isolated measurement points. An example of discrete sensors is fiber Bragg gratings (FBGs). FBGs have become very popular for sensing applications because they offer several advantages compared to electrical strain gauges [63]. FBGs are modifications to the fiber's core in discrete, short segments that reflect particular wavelengths of the full light spectrum and transmit all others, as shown in Figure 1.7. When FBGs are strained, the wavelength of the reflection peaks shifts as illustrated in Figure 1.8. The reflected wavelength λ_{Bragg} is the wavelength that satisfies the Bragg condition according to the following relationship:

$$\lambda_{\text{Bragg}} = 2n\Delta, \tag{1.3}$$

with n the index of refraction and Δ the period of the index of refraction variation of the FBG.

Stretching a FBG causes a change in the grating period, resulting in a change in the reflected wavelength to λ'_{Bragg}. The spectral shift is the difference between the unstrained and strained wavelengths $\lambda'_{\text{Bragg}} - \lambda_{\text{Bragg}}$. The spectral shift depends on the axial strain at the grating but also exhibits a high dependence on temperature. Temperature compensation is required for accurate strain measurements with FBG. Throughout the dissertation, we exploit that strain variations due to the planet passing occur much faster than temperature gradients in the gearbox. We detrended the spectral shift signals to remove the low-frequency content, and the remaining filtered signal is assumed to be produced only by the planet passage effect. Consequently, we assume that temperature variations during each planet's passage are negligible and that the filtered signal can be converted to strain using a linear conversion factor.

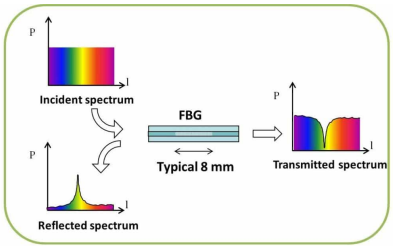

Figure 1.7: Working principle of a fiber Bragg grating (FBG), source https://fbgs.com/.

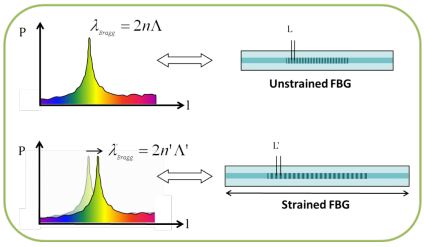

Figure 1.8: Spectral shift response in a FBG as a consequence of strain, source https://fbgs.com/.

FBGs offer a higher signal-to-noise ratio than strain gauges and are immune to electromagnetic interference. The FBG is transparent for the light at wavelengths other than the grating wavelength, making it possible to integrate a large number of sensors in one

fiber. They remain stable over long-term periods and possess good corrosion resistance. A single optical fiber can accommodate multiple sensors (FBGs), simplifying the installation process. In practice, the total number of sensors per fiber has to be chosen, considering the deformations to be measured to prevent wavelengths from different gratings from overlapping. The gratings are sensitive to the strain in the axial direction of the fiber. Because of these properties, they have become popular in other wind turbine components, especially in blades [64].

The fiber-optic sensors must be fixed to the specimen to measure strain, typically by gluing. An optical interrogator sends a full spectrum of light into each fiber and analyzes the reflected light to quantify the wavelength shift from each grating. Interrogator instruments for FBG sensors are still expensive. However, with many sensors per interrogator, the channel cost, including installations, can be lower than traditional strain gages. Using a single interrogator to monitor several wind turbine components, e.g., main frame, main bearings, gearbox and tower, could be an avenue to leverage this advantage. Promising developments in interrogator technology, like single-chip FBG read-out systems based on silicon photonics technology, would enable making FBG sensing more accessible and suitable for high-volume applications like wind turbine gearboxes.

1.6 Goals of this dissertation

The previous sections highlighted the current challenges in wind turbine drivetrains and gearboxes. Maintaining or even improving gearbox reliability with increasing torque density demands has proven to be challenging. This dissertation contributes to providing accurate knowledge of dynamic mechanical torque. Accurate knowledge of the mechanical loads of wind turbine gearboxes has become essential for modern highly loaded gearbox designs with significant dynamic interactions. The traditional method of measuring torque using strain gauges placed on the outer surface of a rotating shaft and transmitting the resulting signal is unsuitable for serial deployment due to technical and economic reasons. To be more precise, the following goal is defined:

Dissertation goal: Develop a method to measure dynamic mechanical torque in geared wind turbines.

A key requirement of the new method to measure torque is that it should enable fleet-wide implementation, and it should be able to operate during the complete service life of the wind turbines. The method presented in this dissertation should apply to geared drivetrains with gearbox configurations where the first stage is an epicyclic planetary stage with a stationary ring gear, regardless of the number and topology of downstream stages. This gearbox configuration represents the vast majority of current and future commercial wind turbines. In these gearboxes, the main shaft of the wind turbine is connected to the input or low-speed shaft (LSS), which is the first-stage planet carrier. Figure 1.9 shows a section view of a gearbox where the first stage is an epicyclic planetary stage. This gearbox was used for the experiments presented in Chapter 4 and Chapter 6. When the planet carrier rotates, it transfers the input torque to the planet shafts. The planet wheels can rotate around the planet shafts and mesh simultaneously with the ring gear and the sun gear to

achieve an increase in speed between the input (planet carrier) and the output (sun gear). The mesh force acting on the ring gear has been denoted as F_p shown in Figure 1.9. The axial component of the gear mesh forces, resulting from the helix angle, has been omitted in this representation. These gear mesh forces deform the teeth of the ring gear and are then transmitted through the body of the ring to the reacting interfaces.

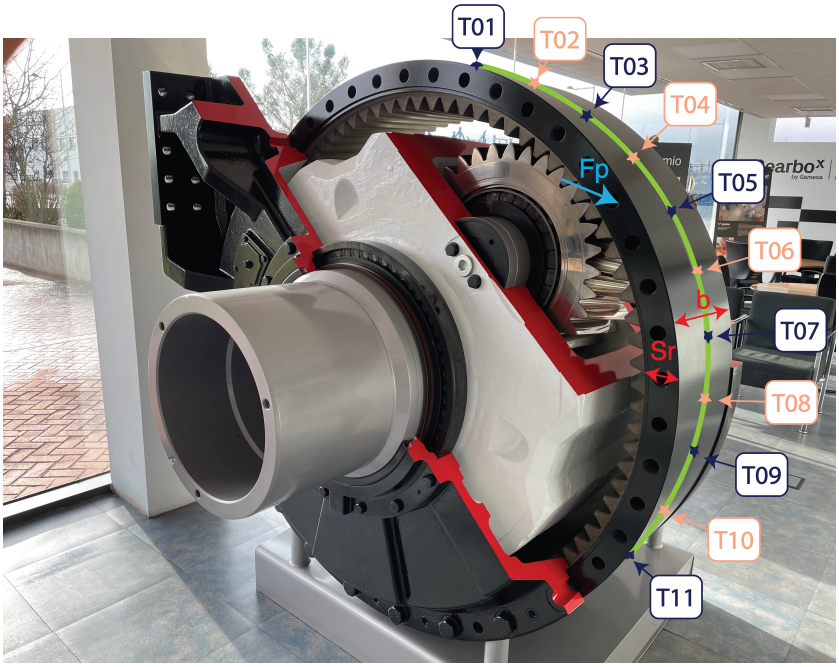

Figure 1.9: G97 2-MW gearbox with the representation of fiber-optic strain sensors on the outer surface of the first stage ring gear installed for torque measurements with the angular location of discrete fiber-optic strain sensors T01 to T11 (adaptation of figure from Gamesa Gearbox (https://www.gamesagearbox.com/wind-technology/).

The first stage ring gear is the most expensive component of the gearbox. Gearbox manufacturers strive to make the rim of the ring gear as thin as possible while complying with the minimum thickness requirements set by their design rules and gear rating standards like ISO 6336-1 and AGMA 6006. The rim thickness for the first stage ring gear is defined as S_r (see Figure 1.9). The deformations on the outer surface of the ring gear, caused by the planets-ring mesh forces, are directly related to the mechanical torque. This leads to the first research question in this dissertation, formalized as:

Research question 1: Is the magnitude of the deformations on the outer surface of the ring gear within the sensing capabilities of commercial fiber-optic strain sensors?

By measuring strain on the static or fixed frame, the difficulties related to data transfer

from a rotating shaft and the power supply of the electronic components on the shaft are avoided. However, a second research question arises and that is formalized as:

Research question 2: How can the dynamic mechanical torque be quantified from the strain readings in discrete fiber-optic strain sensors distributed on the outer surface of the ring gear?

One of the key advantages of fiber-optic strain sensors exploited in this dissertation is the fact that they can accommodate a large number of discrete sensors in a single fiber. This simplifies physical installation and allows deploying multiple sensors to achieve a large spatial resolution. Fiber-optic sensors also provide high-frequency content. With such a rich mapping of strains throughout the gearbox, a third research question is formulated:

Research question 3: Using the fiber-optic strain signals, can the periodic modes that describe the dynamic behavior of the gearbox be identified using data-driven methods?

A key consideration when measuring physical quantities is the errors and uncertainties associated with the sensors used. All sensors have errors that affect the accuracy and uncertainty of the measurements. This leads to the following research question:

Research question 4: How accurate are torque measurements taken by fiber-optic strain sensors in the ring gear?

During the development of new technologies, it is standard practice to utilize test benches that replicate the operating conditions of the final application as closely as possible. A large proportion of the validation and certification process of wind turbine gearboxes is conducted using back-to-back gearbox test benches. In these test benches, the low-speed shafts of two gearboxes are connected, which enables the reproduction of the torques generated by wind turbine rotors in a cost-effective manner. These test benches have been used extensively throughout this dissertation and are considered appropriate for the previous research questions. However, such test benches typically have limited capabilities for producing dynamic torque and generally cannot create controlled nontorque loads, such as axial loads and bending moments induced by the wind turbine rotors. Field testing provides the most realistic platform for performance evaluation of this torque measurement method, as certain problems related to the interaction of multiple drivetrain components can only be discovered after deployment in the field. More explicitly, the following research question is formulated:

Research question 5: How do the turbine operating conditions affect the quality of the torque measurements? Especially what is the effect of speed fluctuations and non-torque loads, i.e. bending moments and thrust axial loads?

Since the method to measure torque using fiber optic strain sensors on the outer surface of the ring gear is based on the deformations caused by the planet passages, it is possible to compare the deformations caused by the different planets and evaluate the planet-load sharing behavior. The way the load is shared between the planets is quantified by the mesh load factor and has become one of the key challenges of next-generation gearbox designs with higher number of planets per stage.

Research question 6: How accurate are mesh load factor results based on fiber-optic strain measurements on the outer surface of the ring gear compared to values obtained from strain gauge measurements in the gear teeth roots?

Gear tooth root strain gauge measurements can only provide an average value of load sharing. The distance between FBGs can be selected as a sensor design variable in discrete fiber-optic sensors.

Research question 7: If the number of strain sensors (FBGs) on the ring gear is selected as an integer multiple of the number of planets, can the mesh load factor be evaluated instantaneously?

This dissertation covers the development process from proof of concept tests all the way up to a technology readiness level (TRL) of 7 (field demonstration on a full-scale prototype). Using fiber-optic sensors for wind turbine gearbox dynamic mechanical torque measurements was demonstrated by conducting extensive test bench experiments and a field validation campaign. Field testing provided the most realistic platform for performance evaluation and enabled investigation of the effects of wind turbine operating conditions on the quality of dynamic mechanical torque measurements, focusing on the effects produced by non-torque loads and temperature.

1.7 Dissertation outline

This section presents the outline of this dissertation, illustrated in Figure 1.10. This dissertation comprises five core chapters, based on previously published articles, allowing an independent reading of each chapter. Each of the chapters contains an introduction reviewing the literature at the time of writing the article. Therefore, some of the concepts and literature presented in Chapter 1 are repeated in the core chapters. A brief summary of the content of each chapter is given below.

Chapter 2 presents test bench experiments conducted to answer research questions one and two. The first stage ring gear of a 6 MW gearbox with a PPH configuration, shown in Figures 1.4 and 1.5, was instrumented with fifty-four fiber-optic strain sensors and tested on a back-to-back test bench to investigate the relationship between measured strain signals and mechanical input torque.

Chapter 3 addresses research question three with an extended measurement setup covering all three planetary stages of a gearbox with a PPPH configuration. The multivariable output-error state space method (MOESP) was successfully applied to identify the periodic modes, referred to as operational deflection shapes, which enable quantifying the unknown periodic excitations and has been found to provide another estimator of the input torque of the gearbox

Chapter 4 presents the results of an extensive field validation of dynamic mechanical torque measurements in a Gamesa G97 2-MW wind turbine at the National Renewable Energy Laboratory's Flatirons Campus which investigate research questions four and five.

In **Chapter 5**, research question six is addressed through an experimental evaluation of the mesh load factor of a modern 6MW wind turbine gearbox with five planets in the first planetary stage. Average results from the traditional method, based on tooth root strain gauges are compared to values derived from strain measurements in the outer surface of the ring gear.

Finally, **Chapter 6** investigates research question number seven by selecting the number of strain sensors on the ring gear as an integer multiple of the number of planets to achieve an instantaneous evaluation of the mesh load factor. The effect of operating conditions on the planet load-sharing behavior of the gearbox was also investigated.

Each chapter contains a conclusions section of its own. In **Chapter 7**, the overall conclusions of this dissertation are presented, and recommendations for future research in wind turbine geared drivetrains are provided.

Disclaimer: The contents of Chapter 2 to Chapter 6 are identical to the scientific articles upon which they are based. While this makes reading the chapters as independent documents possible, it also means that information and figures may be repeated between chapters.

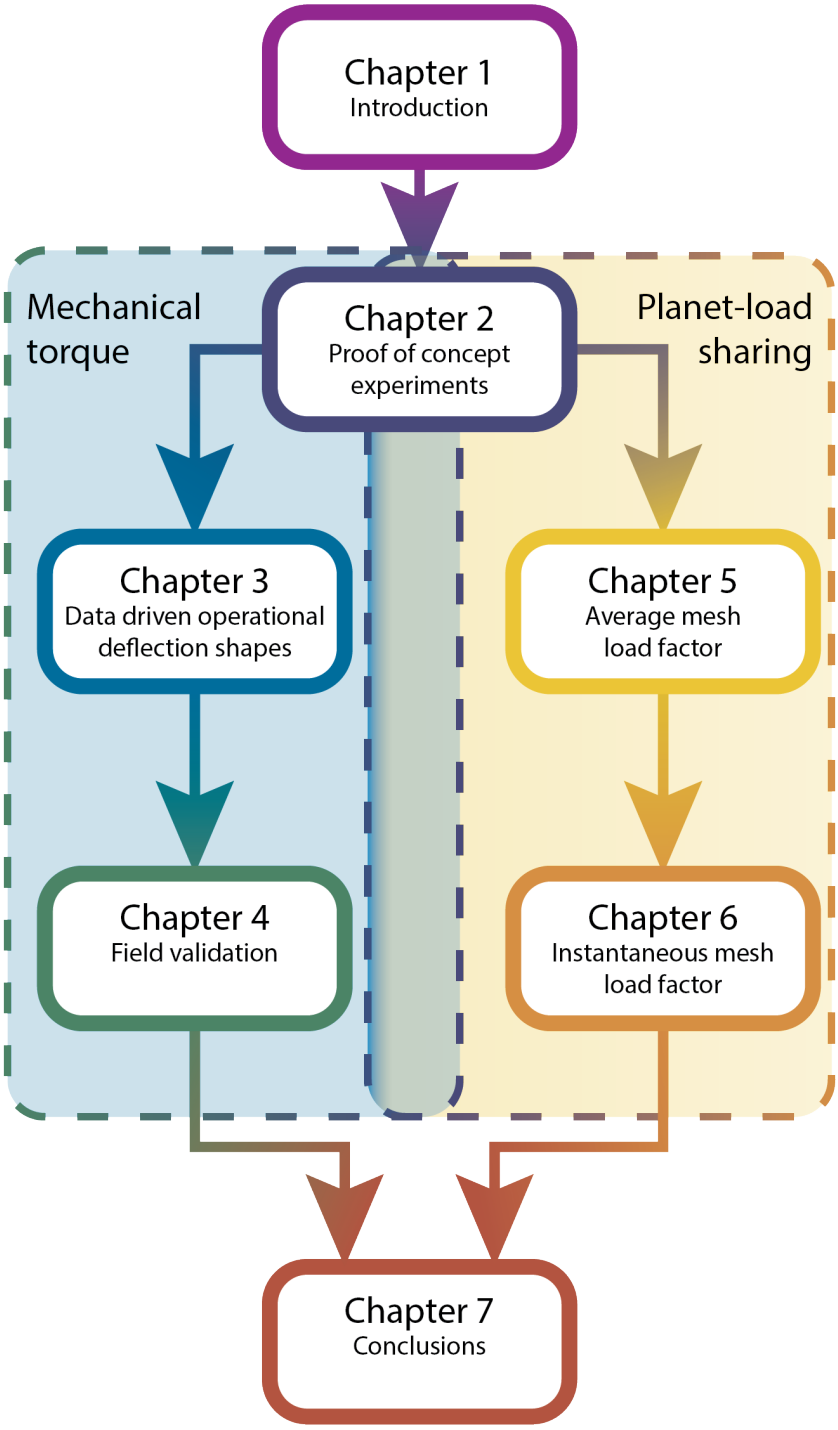

Figure 1.10: Outline of the dissertation

2

Input torque measurements for wind turbine gearboxes using fiber-optic strain sensors

Accurate knowledge of the input torque in wind turbine gearboxes is key to improving their reliability. Traditionally, rotor torque is measured using strain gauges bonded to the main shaft. Transferring the resulting signal from the rotating shaft to a stationary data acquisition system while powering the sensing devices is complex and costly. The magnitude of the torques involved in wind turbine gearboxes and the high stiffness of the input shaft pose additional difficulties. This chapter presents a new alternative method to measure the input torque in wind turbine gearboxes based on deformation measurements of the static first-stage ring gear. The present study was conducted on a Siemens Gamesa Renewable Energy gearbox with a rated power of 6 MW, in which a total of 54 fiber-optic strain sensors were installed on the outer surface of the first-stage ring gear. The gear mesh forces between the planets and the ring gear cause measurable deformations on the outer surface of the stationary ring gear. The measured strains exhibit a dynamic behavior. The strain values change depending on the angular position of the planet carrier, the instantaneous input torque, and the way load is shared between planets. A satisfactory correlation has been found between the strain signals measured on the static ring gear and torque. Two signal processing strategies are presented in this chapter. The first procedure is based on the peak-to-peak strain values computed for the gear passage events, and therefore torque can only be estimated when a gear mesh is detected. The second signal processing procedure combines the strain signals from different sensors using a Coleman coordinate transformation and tracks the magnitude of the fifth harmonic component. With this second procedure, it is possible to estimate torque whenever strain data of all sensors are available, leading to an improved frequency resolution up to the sampling frequency used to acquire strain data.

2

This chapter is based on the following publication: *U. Gutierrez Santiago. Input Torque Measurements for Wind Turbine Gearboxes Using fiber-optic Strain Sensors* [65]. Indigo is the second color of the rainbow when arranged by increasing wavelength. Indigo has a wavelength between 420 nm and 450 nm. The human eye is relatively insensitive to indigo's frequencies, which has led to a debate on whether indigo should be regarded as a distinct colour or a shade of blue and violet. Historical evidence suggests that Newton's definitions of indigo and blue differ from modern interpretations. Newton's indigo aligns with today's blue, while his blue corresponds to cyan. The ancient Greek philosopher Aristotle (384-322 BC) formulated the earliest known theory of color. He proposed that all colors originated from white and black (lightness and darkness) and linked them to the four elements: water, air, earth, and fire. Aristotle's views on color were widely accepted for over 2000 years until they were eventually replaced by Newton's theories. The Dutch scientist Christiaan Huygens (1629–1695) challenged Newton's corpuscular theory of light by proposing a wave theory of light in his *Traité de la Lumière* (1690). Huygens' theory was initially rejected in favor of Newton's corpuscular theory. However, in 1821, Augustin-Jean Fresnel (1788–1827) adapted Huygens' principle to explain the rectilinear propagation and diffraction effects of light. Today, this principle is known as the Huygens–Fresnel principle.

2.1 Introduction

Scientists have long been warning us that we face a significant challenge regarding our climate. Renewable energies can play a pivotal role in reducing carbon emissions to enable a sustainable future. In the last decades, wind energy has seen a remarkable growth. Wind energy is already the second source of power generation in the EU when ranked according to installed capacity [66]. In Europe (EU27 + UK), the total installed capacity of wind power reached 220 GW in 2020, of which 194 GW is onshore wind. With 458 TWh generated, wind power covered 16 % of Europe's electricity demand in 2020 [67]. It is essential to reduce the levelized cost of energy (LCoE) from wind to guarantee further deployment of wind turbines towards the needed energy transition. Therefore, the LCoE has become one of the critical drivers for wind energy research in industry and academia.

In onshore wind energy, 75 % of turbines have a geared drivetrain [68]. The gearbox transfers the torque generated by the blades from the slow-speed rotor to the higher-speed generator. In the overall breakdown of costs, the gearbox is one of the main contributors because of the associated capital expenditure and the considerable contribution to operation and maintenance costs [69]. Gearbox reliability is improving, but gearboxes continue to be the largest wind turbine downtime source [70] and generally do not reach the desired design life of 20 years [71, 72]. Therefore, improving gearbox reliability would lead to a significant reduction in the LCoE from the wind.

Drive train subsystem interactions and the effect of control strategy on gearbox loading are not fully known [68]. The flexibility of the gearbox components influences the drivetrain's dynamic behavior and, therefore, the loading [73]. Traditional engineering models used for the simulation of gearbox input loads do not include this influence. Complex physically derived models have been built to study gearbox dynamics but have not been used together with whole turbine models [74–76]. Current wind turbine design codes lack insight into the dynamic behavior of the internal drive train components. It is, therefore, highly desirable to be able to measure the dynamic torque from the rotor acting on the gearbox accurately and reliably. This torque will be referred to as the gearbox input torque.

A case study presented by Winergy and Siemens PLM Software [43] showed that data from the supervisory control and data acquisition (SCADA) were not able to precisely capture the torque fluctuations caused by the dynamic wind turbine operation, for example during a brake event, and concluded that it is necessary to perform a direct measurement of the actual torque. The traditional method to measure torque is based on bonding strain gauges to the rotating shaft. The strain gauges convert the deformation caused by the torque into a change in electrical resistance. Transferring the resulting signal from the rotating shaft to a stationary data logging system and powering the data acquisition devices is difficult and costly. In wind turbine gearboxes, the main shaft's deformation is small because of its high stiffness, which typically results in a low signal-to-noise ratio. These drawbacks have limited the use of such measurements to laboratory environments [77], validation and certification of experimental wind turbines, and troubleshooting exercises [46]. More recently, Zhang et al. explored different alternatives to measure torque in wind turbine drivetrains and added that a long-term measurement of torque is considered to be nonpractical or economically not feasible [78].

Fiber-optic sensors have several advantages compared to electrical strain gauges [63],

the main ones for wind turbine applications are the following: (1) the signal-to-noise ratio of optical sensors is higher compared to conventional sensors, (2) they are immune to electromagnetic interference because they use light, and (3) many strain sensors can be accommodated in a single fiber. Because of these qualities, fiber-optic sensors have become popular in other wind turbine components. For example, fiber-optic sensors are used in wind turbine blades for condition monitoring and design optimization purposes [64].

The present chapter develops a new method to measure the input torque of wind turbine gearboxes. The proposed method measures strain directly in the fixed frame. In this study, a total of 54 strain sensors were installed on the outer surface of the first-stage ring gear. We have used fiber-optic strain sensors to overcome the main limitations of electrical strain gauges. The study was conducted using a Siemens Gamesa Renewable Energy (SGRE) gearbox manufactured by Gamesa Energy Transmission (GET). The gearbox is a 3-stage gearbox, where the first and second are planetary stages, and the third is a parallel stage, with a rated power of 6 MW and a weight of approximately 44000 kg.

The main contribution of this chapter is to develop a new method to measure input torque in wind turbine gearboxes based on deformations in the fixed frame. The difficulties related to measuring on a rotating shaft are overcome by measuring on the outer surface of the ring gear using fiber-optic strain sensors to explore their advantages compared to conventional electric strain gauges. An experimental demonstration was performed on a full-scale wind turbine gearbox in a back-to-back test bench. The applicability of this method to determine the load sharing between planet gears is also explored.

The remainder of this chapter is organized as follows: Section 2.2 gives a background on the fundamental principles used to measure torque from a static part in the gearbox, optical fiber sensing, and the test setup used for the experiments. Section 2.3 describes a signal processing procedure to estimate torque based on peak strain values of each individual sensor and Section 2.4 describes an alternative procedure based on a Coleman coordinate transformation to combine the instantaneous strain values of all sensors. Section 2.5 discusses the results obtained with both signal processing procedures. Finally, Section 2.6 draws the main conclusions of this work and suggests recommendations for future work.

2.2 Background

2.2.1 Gearbox fundamentals

The primary function of the gearbox is to transfer the power generated by the wind from the main shaft supporting the rotor hub to the generator. In this transfer, the gearbox has to provide the needed increase in rotational speed. This speed increase is achieved in several stages. A variety of gearbox architectures have been used in commercial wind turbines, most of which combine planetary and parallel gear stages. Up to a rated power of around 2 MW, the most widely used configuration consist of an epicyclic planetary stage followed by two helical parallel stages, also known in the industry as PHH or 1P2H. For more powerful turbines with larger rotor diameters (from around 3 MW to 8 MW), a gearbox configuration with two planetary stages and a single parallel stage has become dominant and is referred to as PPH or 2P1H.

The present study was conducted on a SGRE gearbox manufactured by GET with a

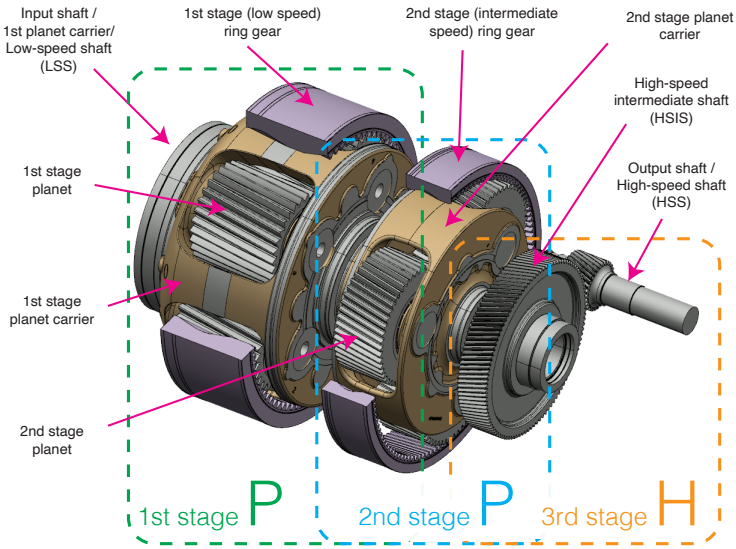

Figure 2.1: Assembly drawing of shafts and gears from the 3-stage Siemens Gamesa Renewable Energy gearbox (PPH configuration).

rated power of 6 MW. This gearbox has a PPH configuration. A drawing of the shafts and gears in this gearbox is shown in Figure 2.1. The structural housings of the gearbox have been omitted for clarity. For even more powerful turbines, due to several factors like size constraints and the need to increase torque density, the industry is evolving to gearbox architectures with three planetary stages.

Regardless of the number of downstream planetary stages, the method presented in this chapter can be applied to all gearbox configurations where the first stage is an epicyclic planetary stage with a stationary ring gear. In these gearboxes, the main shaft of the wind turbine is connected to the input or low-speed shaft (LSS) of the gearbox, which is the first-stage planet carrier. Figure 2.2 shows a section view of the first stage of the gearbox used in this study. When the planet carrier rotates, it transfers the input torque to the planet shafts. The planet wheels can rotate around the planet shafts and mesh simultaneously with the ring gear and the sun gear to achieve an increase in speed between the input (planet carrier) and the output (sun gear). The radial and tangential components of the mesh forces acting on the ring gear, resulting from the pressure angle of the gears, are shown in Figure 2.2, where they are denoted as F_{ti} for the tangential component and F_{ri} for the radial component of the i^{th} planet. The axial component of the gear mesh forces, resulting from the helix angle, has been omitted in this representation. These gear mesh forces deform the teeth of the ring gear and are then transmitted through the body of the ring to the reacting interfaces.

The first-stage ring gear is the most expensive component of the gearbox in modern

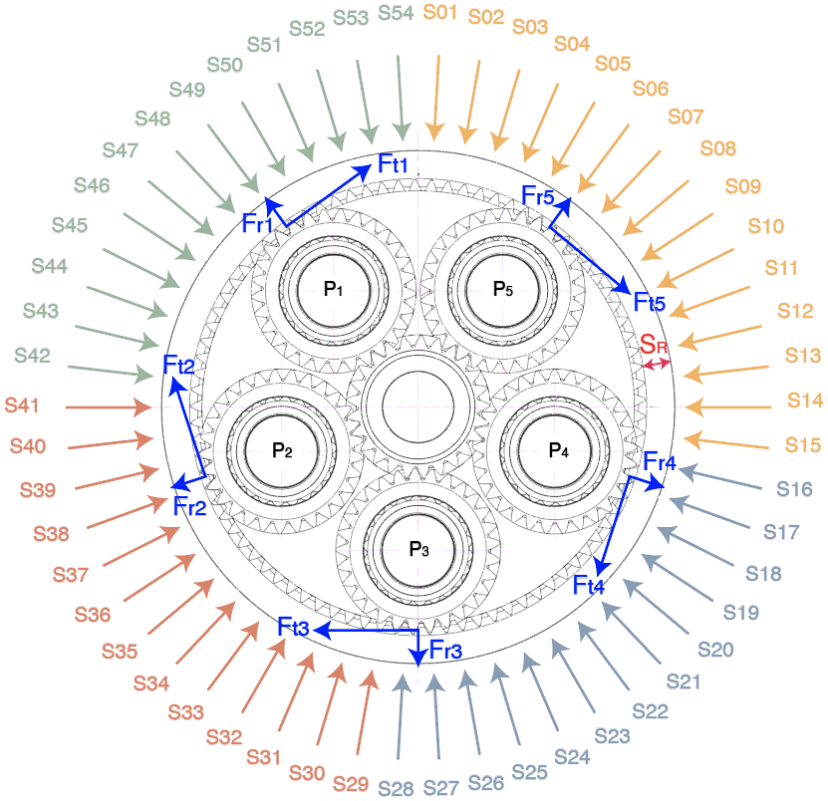

Figure 2.2: Rotor side view of the middle section of the first planetary stage with the angular location of the strain sensors (S01 to S54). S_R is the ring gear rim thickness, and F_{ti} and F_{ri} are the tangential and radial gear mesh loads from the i^{th} planet (P_i).

wind turbine gearboxes. Gearbox manufacturers strive to make the rim of the ring gear as thin as possible while complying with the minimum thickness requirements set by their design rules and gear rating standards like ISO 6336-1. The rim thickness for the first-stage ring gear is defined as S_R (see Figure 2.2). Significant deformations are expected on the outer surface of the ring gear when the planets mesh with the ring gear because the rim is relatively thin. The research presented in this chapter explores if and how strain measurements in the outer surface of the first ring gear can be used to derive the gearbox input torque.

2.2.2 Test bench setup

Wind turbine gearboxes are typically tested in a back-to-back arrangement. Two gearboxes are connected through the low-speed shaft (LSS) to reproduce the torques generated by wind turbine rotors in a cost-effective manner. Figure 2.3 shows the layout of the back-to-back test bench used for the present study, where electric motors produce the driving

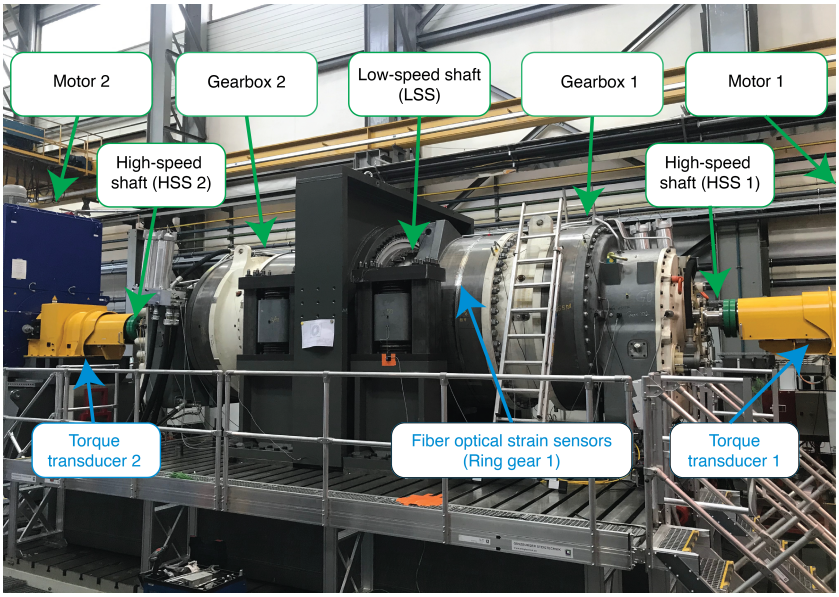

Figure 2.3: SGRE gearboxes on a back-to-back test bench (property of DMT GmbH & Co. KG). The first-stage ring gear of gearbox 1 was instrumented with fiber-optic strain sensors.

and braking torques. In the back-to-back configuration, a second gearbox is needed to reduce the rotating speed of the electric motor that acts as a driver and to increase the torque (referred to as "Gearbox 2" in Figure 2.3). The input or driving motor is typically controlled to reach the desired running speed, and the driven motor is controlled to provide the specified braking torque, thus achieving the desired test conditions on "Gearbox 1".

Nevertheless, the gearbox operates at different boundary conditions compared to the wind turbine drivetrain configuration. The three main differences between a wind turbine and a back-to-back test bench are the following: (1) in a back-to-back test bench torque is the only controlled input load excitation; (2) the stiffness of the mechanical interfaces are different from the ones used in the nacelle of a wind turbine (mainframe, input or main shaft, and high-speed shaft coupling); (3) there is a lack of a tilt angle in the test bench, and the gearboxes are positioned with the main axis in a horizontal plane. Despite these differences, we consider the back-to-back test bench results representative of the wind turbine behavior when it comes to input torque.

A full-scale gearbox with a rated nominal power of 6 MW was instrumented using optical fiber sensors. The position of the fiber-optic sensors can be seen in Figure 2.3 on the outer surface of the first-stage ring gear of "Gearbox 1". All tests presented in this study were performed on the back-to-back test bench shown in Figure 2.3, property of the company DMT GmbH & Co. KG [79] at Krefeld (Germany) with electric motors of a rated power of 7.5 MW.

2.2.3 Fiber-optic sensors

The fiber-optic strain sensors used in the present study are based on fiber Bragg gratings (FBGs). These FBGs are a periodic variation of the refractive index of the fiber's core. At each refraction change, a small amount of light is reflected, and all the reflected light combines into one large reflection at the wavelength where the grating period satisfies the Bragg condition. The FBG is transparent for the light at wavelengths other than the grating wavelength, making it possible to integrate a large number of sensors in one fiber. The Bragg relation is

$$\lambda_{\text{Refl}} = 2n\Delta\,, \tag{2.1}$$

with n the index of refraction and Δ the period of the index of refraction of the FBG. The parameters n and Δ depend on the temperature and axial strain at the grating. When a full spectrum is inserted into the fiber, a specific wavelength is reflected at each FBG sensor. Strain and temperature changes at each FBG shift the reflected wavelength. The FBGs used in this study have a theoretical sensitivity to strain of 1.19 pm wavelength shift per µm/m strain and the sensitivity to temperature is 27.9 pm/°C. Several FBGs can be integrated into a single optical fiber. In practice, the total amount of sensors per fiber has to be chosen taking into account the deformations and temperatures to be measured to prevent wavelengths from different gratings from overlapping. The gratings are sensitive to the strain in the axial direction of the fiber.

For the present study, four optical fibers were installed with 14 FBGs accommodated on each fiber. Out of the resulting 56 gratings, 54 gratings were used to measure strain in the positions shown in Figure 2.2. The remaining two gratings were dedicated to temperature measurements. These two gratings were placed in the vicinity of strain sensors S02 and S29 with a small tube around the FBGs to prevent straining the fiber. However, the installation was not successful, and it was not possible to gather reliable temperature data from these two FBGs. The four optical fibers were installed on the outer surface of the first-stage ring gear, at the middle section along the width of the ring gear in the axial direction, as shown in Figure 2.3. The middle section was chosen to minimize the local effects of the bolted joints at the rotor and generator side. The fibers were installed tangentially to the middle section, covering a complete revolution along the outer perimeter of the ring gear. Figure 2.2 shows the radial and angular location of all the strain sensors with the corresponding labels in a rotor side section view. Due to the placement of the fibers, the FBGs measure the deformation of the outer surface of the ring gear in the tangential direction of Figure 2.2. The four different colors for the sensor labels indicate how the FBGs were grouped into separate fibers (S01 to S15 in fiber number 1, S16 to S28 in fiber number 2, S29 to S41 in fiber number 3, and S42 to S54 in fiber number 4). The four optical fibers were connected to an optical interrogator. The interrogator sends a full spectrum of light into each fiber and acquires the reflected light to quantify the shift of wavelength from each grating. Three analog signals were added to associate the fiber-optic strain measurements with the gearbox operating conditions: two torque transducers installed at the high-speed shaft (HSS) couplings (see Figure 2.3) and an inductive sensor providing a once-per-revolution pulse of the input shaft (see Figure 2.4). The purpose of this inductive sensor is to provide information on the angular position of the input shaft and, therefore, the relative position of the planet carrier and the planets.

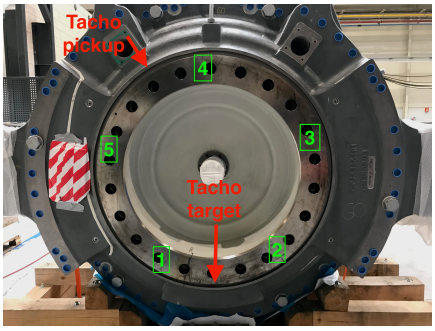

Figure 2.4: Position of planets and input shaft marker, stationary inductive sensor, and rotating target. Tacho is short for tachometer.

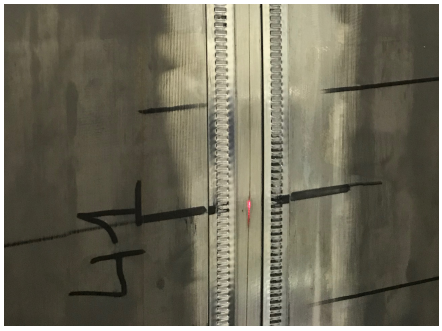

Figure 2.5: Detail view of an optical fiber where a Bragg grating is illuminated in red (S41).

The fiber-optic sensors were supplied and installed by the company Sensing360 B.V. [80]. Before installing the fibers, the outer surface of the ring gear was sanded to improve the bonding between the fiber and the ring gear. The fibers were glued to the ring gear's outer surface using a cyanoacrylate adhesive. Figure 2.5 shows a naked optical fiber with an illuminated fiber Bragg grating (S41) due to the exposure to a colored laser beam. The polished surface needed for the installation can be observed in Figure 2.5.

2.2.4 Experiments

The results presented in this study were obtained during tests performed for the validation campaign of the SGRE gearboxes. In order to characterize the relationship between torque and strain, the instrumented gearbox was run under different stationary speed and torque conditions. During this torque vs. strain calibration process, 20 short tests were performed where the torque level was increased in 5 % increments from 5 % to 100 % of the nominal, while the gearbox rotational speed was kept constant and equal to the nominal value.

After the stationary calibration tests, the gearbox was run under dynamic torque conditions to collect strain data and evaluate the torque estimation procedures. In particular, two different tests with variable torque will be presented. First, a test with a linearly increasing torque reference command was performed. Then, a second test was conducted where the torque level was changed in steps as the test bench controller allowed. During both variable torque tests, the reference speed command was kept constant.

2.2.5 Data acquisition and signal pre-processing

Data from the fiber-optic sensors were logged directly by an optical interrogator, and data from the analog signals were logged by a separate data acquisition system. Both systems are independent, but the data were time-stamped using the POSIX [81] time which allowed for time synchronization of sufficient accuracy. A sampling frequency of 2500 Hz was used to collect data from all 54 strain sensors.

Two preprocessing steps were applied to the signals from fiber-optic sensors. First,

the data were cleaned from glitches caused by the interrogator. A sudden drop in the value was observed in some of the logged signals. These drops were due to hardware communication errors and could be easily detected and removed. After the glitches in the data were removed, a moving average filter was applied. The combined resolution of each strain sensor and the data acquisition system was found to be approximately 0.6 $\mu\epsilon$. The strain data signal can jump from one sample to the next in a set of fixed values separated by the sensor resolution. A moving average filter was applied to the 54 strain signals to filter this effect. The moving average was realized using a window size of seven samples.

After the above-mentioned preprocessing steps, strain signals were detrended to remove the effect of temperature on the measured shifts in wavelengths of the FBSs; see Section 2.2.3. Once the long-term shift caused by temperature had been removed, the remaining signal was considered to be caused entirely by the strain imposed from the planet gear mesh events.

2.3 Torque estimation using peak-to-peak strain values

For each of the tests performed in the back-to-back test bench, described in Sections 2.2.2 and 2.2.4, data were acquired and logged from the 54 fiber-optic strain sensors and the three analog signals described in Section 2.2.3.

2.3.1 Identification of strain peaks caused by gear mesh events

When the gearbox was tested under stationary torque and speed conditions, the individual signals from each fiber-optic strain sensor exhibited a positive or tensile strain peak every time a planet meshed with the ring gear in the vicinity of the sensor. Figure 2.6 shows the acquired strain signal of the individual sensor "S01" during one revolution of the low-speed shaft. Each full revolution of the input shaft is marked by a pulse from the inductive sensor in orange, five positive or tensile strain peaks are observed corresponding to the passing of the five planets in blue. A large tensile deformation occurs when a planet passes below the measurement location. As the low-speed shaft keeps turning, the strain diminishes, reaching compression. First, a local minimum is observed; then, the strain briefly recovers but drops again until a global minimum is reached. The strain keeps increasing from this global minimum until the next tensile peak.

In order to study the relationship between torque and strain, 20 tests were performed running the gearbox under stationary speed and torque conditions. While the gearbox rotational speed was kept constant and equal to the nominal speed, the torque was increased in 5 % increments from 5 % to 100 %. In each test step, the strain signals of all 54 sensors were measured and logged for 4 minutes. The magnitude of the strain difference or peak-to-peak value between the detected maxima and local minima peaks was computed for each of the 54 strain sensors for all 20 test steps. This magnitude will be referred to as the peak-to-peak value. The local minima were chosen because the time difference from the maxima to the corresponding local minima is in the range of the gear mesh cycle, and it is believed to be more representative of the gear mesh forces. Figure 2.7 shows the average peak-to-peak values computed for five tests at different torque levels using the local minima. The peak-to-peak value of each sensor is plotted according to the corresponding sensor angular location (rotor side view) shown in Figure 2.2.

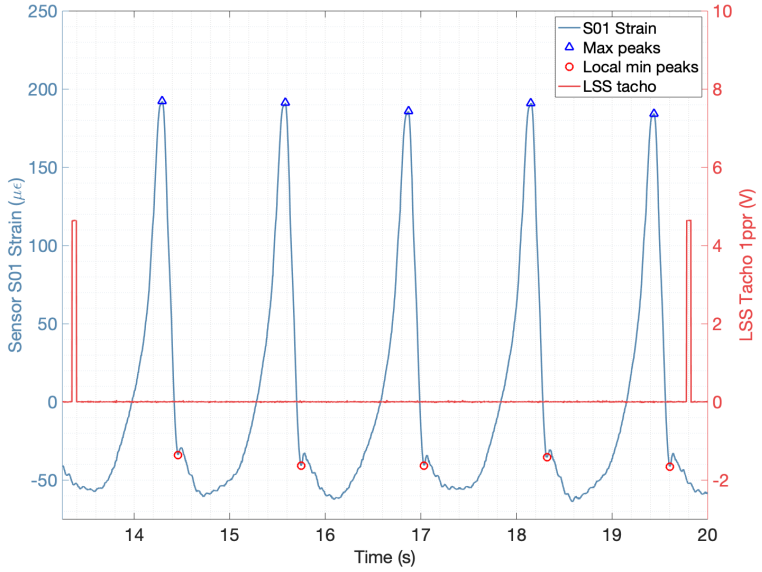

Figure 2.6: Sensor S01 strain signal (left axis) during a single revolution of the input shaft (right axis) with detected peaks.

The input torque was not measured directly and was calculated using the torque data from the torque transducers installed in the high-speed shafts (see Figure 2.3). The efficiency of both gearboxes was assumed to be the same, and the LSS or input torque was computed as the average of both HSS torques multiplied by the gear ratio. The torque signals were averaged for the time segments between the tensile and compression peaks.

2.3.2 Relationship between peak-to-peak strain values and torque

Having measured strain on 54 locations on the outer surface of the static first-stage ring gear, and with the simultaneous data available from the torque transducers installed at both high-speed shafts, the following section shows how the measured strain signals can be correlated with the input torque.

Each measurement location has its own individual behavior with respect to torque, as can be seen in Figure 2.7. A regression polynomial can be computed using the least-squares criterion for each individual strain sensor to fit the peak-to-peak values with the torque. A linear, a quadratic, and a cubic fit of torque vs. peak-to-peak were investigated for comparison purposes. Figure 2.8 shows the average peak-to-peak values vs. torque for three different measurement positions together with the cubic polynomial approximations. Only cubic regressions are shown for clarity purposes, and similar regressions can be produced for every individual sensor as described in Section 2.3.1. When analyzing the different order regressions, the linearity of the peak-to-peak vs. torque behavior was observed to be different in each measurement location. The sensors S04, S17, and S53

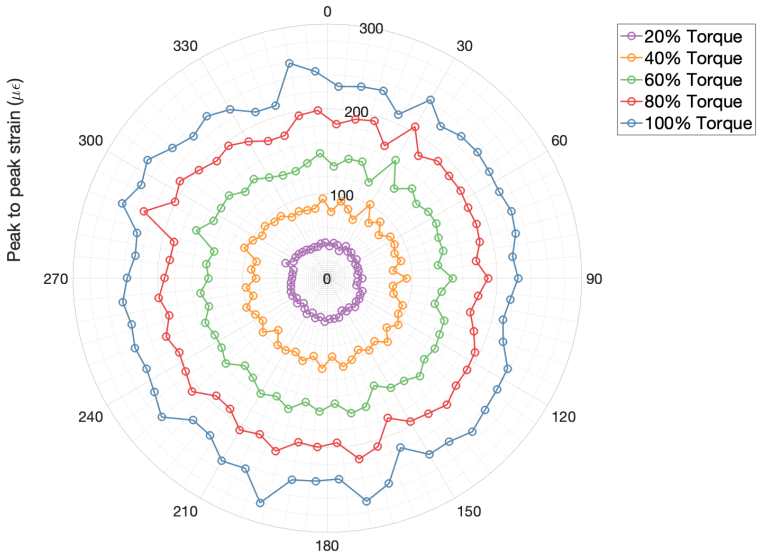

Figure 2.7: Average peak-to-peak strain values of all 54 sensors for five different torque levels (20 %, 40 %, 60 %, 80 %, and 100 % torque).

were chosen for Figure 2.8 because the difference in their behavior is representative of the largest differences observed. Several factors were expected to play a role in the torque to deformation relationship, e.g., the lack of symmetry of the housings connected to the ring gear, the different relative position between the strain sensors and the gear teeth, and the possibility to have different load distributions across the face width for different angular positions. However, the differences in linearity observed for different sensors are not fully understood by the authors yet. Sensors S04, S17, and S53 were chosen for Figure 2.8 because the difference in the peak-to-peak vs. torque behavior was more pronounced. Sensor S04 exhibited a lower more linear response, while sensors S17 and S53 had a larger response but lower linearity. However, it is possible to achieve a satisfactory fit for all points by increasing the order of the regression polynomial.

2.3.3 Load sharing between planets

A polynomial fit of the average torque can be derived using the peak-to-peak values from each strain sensor. To extend this result for a dynamic situation, the load sharing between planets has to be known. The strain signals exhibit a highly dynamic nature, and peak-to-peak values change with time. These changes can be due to changes in torque and possibly also due to changes in load sharing between planets.

The gear rating standard ISO 6336-1 (2019) [58] defines the planet load share factor K_γ as the load carried by the planet gear carrying the higher load divided by the average

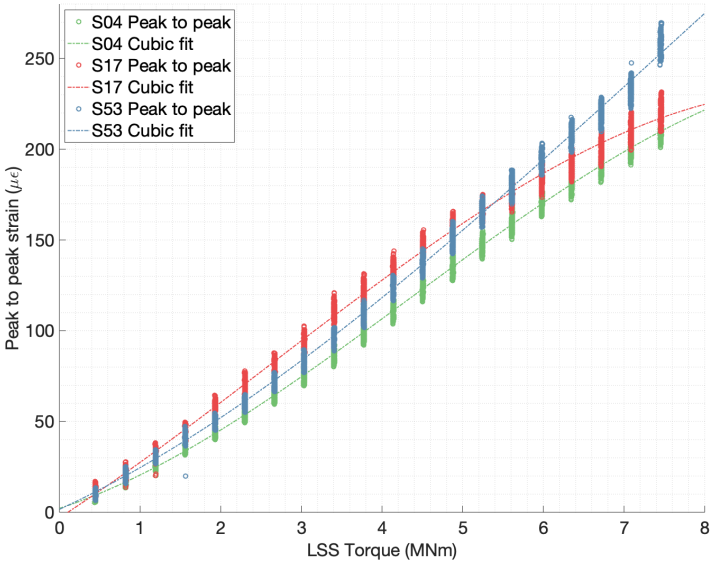

Figure 2.8: Peak-to-peak strain values of all detected gear mesh events of strain sensors S04, S17, and S53 vs. torque in the low-speed shaft.

load of all planets. Since a satisfactory fit has been found between the average torque and the average peak-to-peak values, the following expression is proposed to derive K_γ of a particular planet from the measured peak-to-peak strain values

$$K_{\gamma i} = \frac{\overline{\Delta}_i}{\overline{\Delta_{all}}}, \tag{2.2}$$

where $\overline{\Delta}_i$ is the average peak-to-peak value from a particular planet i, and $\overline{\Delta_{all}}$ is the average peak-to-peak value of all planets. It is possible to assign peak-to-peak values to individual planets because the position of the planets relative to the once-per-revolution pulse is known (see Figure 2.4). The meshing sequence of the planets is fixed if the sense of rotation is known. The spacing between strain sensors is not an integer multiple of the number of planets, so with the instrumentation setup used in this study, it is not possible to compare strain peaks in different positions simultaneously. Figure 2.9 shows the resulting average K_γ for each strain sensor position obtained computing Eq. (2.2) with the average peak-to-peak values.

Using the correlation of peak-to-peak values vs. torque and the average planet load share K_γ, an approximation of the instantaneous torque can be made. Figure 2.10 shows the average K_γ values of the five planets for their corresponding average torque values. As can be seen in Figure 2.10, the load sharing coefficient between planets depends on the gearbox input torque value. An improvement of K_γ was observed when increasing torque in the gearbox, with K_γ values approaching the optimal value of one. In order to

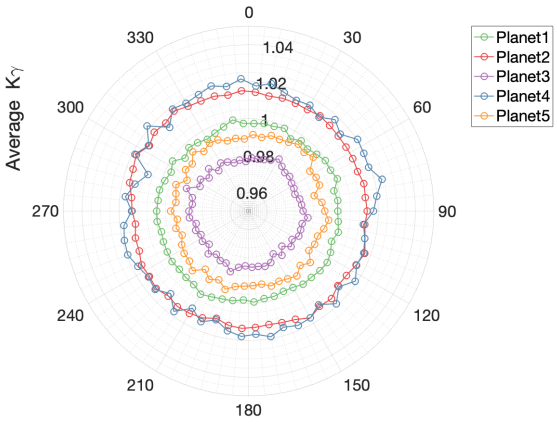

Figure 2.9: Average K_γ per planet for each sensor.

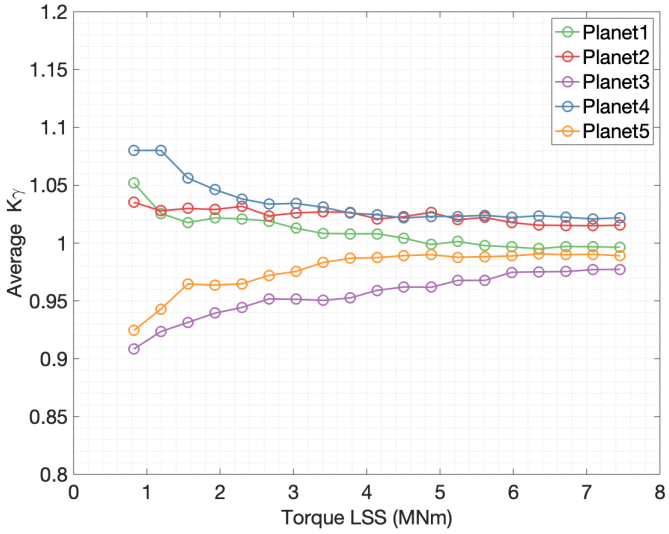

Figure 2.10: Average K_γ vs. torque for the strain sensor S52.

avoid a second linear regression, both data fitting steps can be merged into one. First, each detected mesh event is assigned to its corresponding planet. Then a regression polynomial is computed from the peak-to-peak strain values to torque for each individual planet.

2.3.4 Torque estimation procedure using peak-to-peak strain values

With the approximation to K_γ presented in Section 2.3.3, torque can be estimated when a mesh event is detected. The procedure is represented in Figure 2.13 and can be summarised as follows.

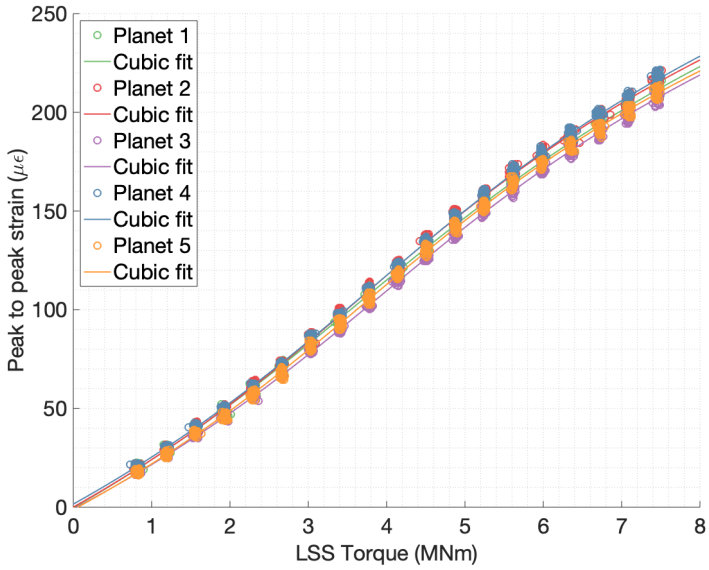

Figure 2.11: Peak-to-peak strain values of sensor S52 vs. torque in the low-speed shaft separated for each planet and their corresponding cubic fit.

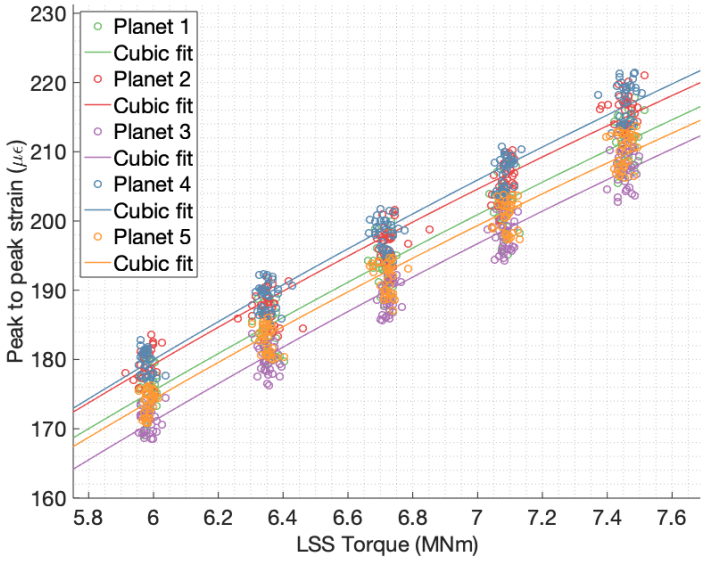

Figure 2.12: Peak-to-peak strain values of sensor S52 vs. torque in low-speed shaft separated for each planet (zoom for higher torque range).

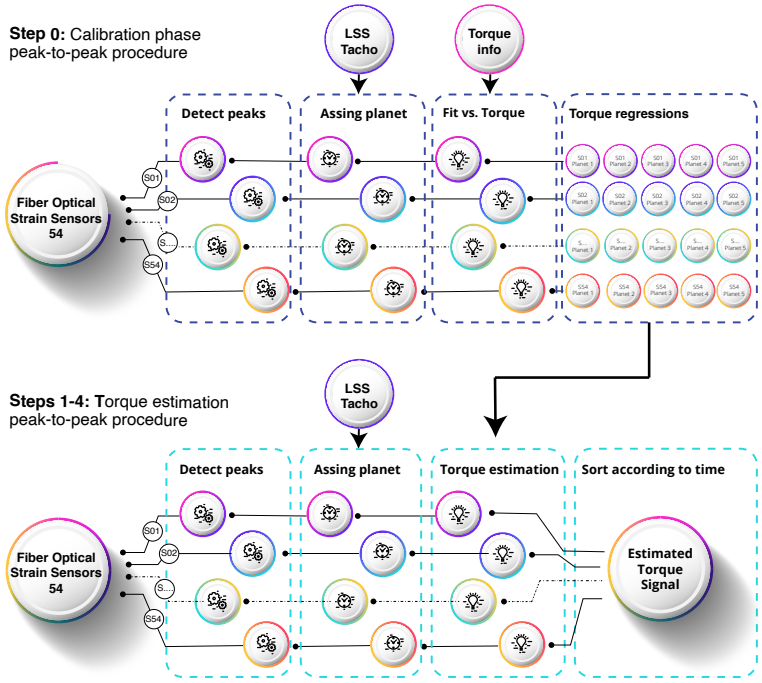

Figure 2.13: Torque estimation procedure based on peak-to-peak strain values.

- **Step 0** *Calibration phase.* Learn the peak-to-peak vs. torque correlation for each planet and each measurement location to produce $n \cdot p$ regression polynomials, n is the number of strain sensors and p is the number of planets.

- **Step 1** *Detect peaks.* For a new data set of strain signals, for every individual strain signal, detect gear mesh events and identify their associated maximum and minimum peak strain values to compute the peak-to-peak value.

- **Step 2** *Assign planet.* With the information from the once-per-revolution input shaft pulse, assign the detected gear mesh event to the corresponding planet that caused the strain.

- **Step 3** *Torque estimation.* Evaluate the corresponding regression polynomial to compute a torque value from the peak-to-peak value (taking into account the strain sensor and the individual planet involved in the gear mesh).

- **Step 4** *Sort according to time.* Repeat steps 1 to 3 for all mesh events detected in all strain sensors and sort the estimated torque values from individual mesh events according to the time when the gear mesh event was detected.

2.4 Torque estimation using a coordinate transformation

With the data processing strategy for torque estimation based on peak-to-peak values presented in Section 2.3, torque can only be evaluated when a gear mesh event between a planet and the ring gear is detected. To overcome this limitation, an alternative procedure has been developed based on a coordinate transformation of the strain signals, followed by an analysis and tracking of the harmonic components. This procedure combines the information from different strain sensors to exploit the signal information between mesh events.

The Coleman transformation or Fourier coordinate transformation can transform the equations of motion from a rotating coordinate system to a non-rotating coordinate system. In wind turbines, the Coleman transformation is also referred to as the multi-blade coordinate transformation (MBC). The term MBC was adopted from helicopter theory [82] and is widely used to analyze the dynamics of the wind turbine rotors [83, 84].

For the instrumentation setup used in the present study with 54 strain sensors, the Coleman transformation can be particularized to the following equations:

$$p_{nc}(t) = \frac{2}{54} \sum_{s=1}^{54} \delta_s(t) \cos\left(n\psi_s(t)\right), \tag{2.3}$$

$$p_{ns}(t) = \frac{2}{54} \sum_{s=1}^{54} \delta_s(t) \sin\left(n\psi_s(t)\right), \tag{2.4}$$

where $\delta_s(t)$ is the strain of the s^{th} FBG sensor for a given time t and $\psi_s(t)$ is the assigned angular position of the sensor at that time t (see Section 2.2.3). The angle $\psi_s(t)$ is defined as the relative angle between the angular location of each sensor according to Figure 2.2 and the angular location of the input shaft. The angular location of the input shaft determines the angular position of the planet carrier and, therefore, the five planets. The angular location of the input shaft is also known as the azimuth angle of the rotor. The coefficients $P_{nc}(t)$ and $P_{ns}(t)$ can be computed for any integer multiple of n and for any time t when strain data of all sensors are available.

For low values of n, where the Nyquist criterion is satisfied, the expressions in Eqs. (2.3) and (2.4) are equivalent to the sine and cosine coefficients of a Fourier series decomposition of the resulting periodic function $\delta(\psi)$. The function $\delta(\psi)$ is a discrete representation of the strain of the 54 measurement points δ as a function of their assigned angle ψ. Figure 2.14 shows the signal values δ_s for all 54 strain sensors against their assigned angle ψ_s for a given time sample t_0. In this case, t_0 corresponds to a time sample when the start of the once-per-revolution pulse was detected. The strain values of tests with different torque levels are shown in Figure 2.14 using strain data samples that correspond to the same angular position.

The 54 strain sensors are equally spaced around the full revolution of the ring gear, and therefore the function $\delta(\psi)$ is a periodic function with a period of 2π. Its Fourier series decomposition is defined as a sum of the basis functions $\phi_n(\psi)$ times complex coefficients

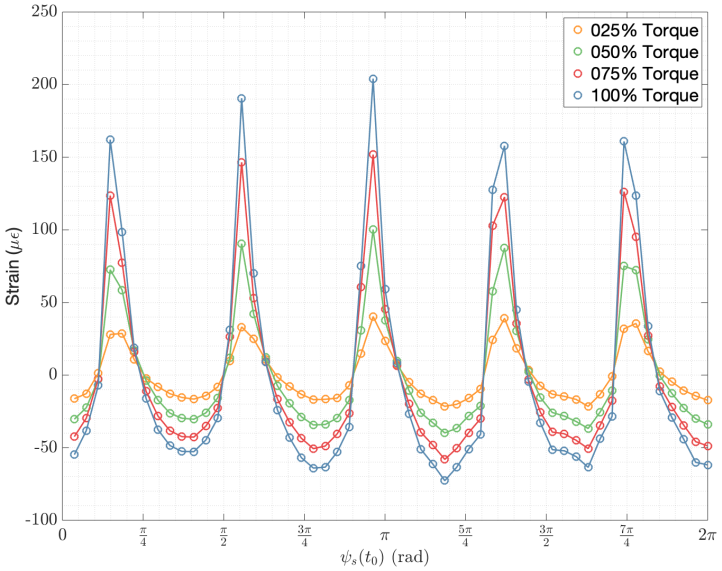

Figure 2.14: Instantaneous signal values of all 54 strain sensors for four different torque levels (25 %, 50 %, 75 %, and 100 % Torque).

p_n:

$$\delta(\psi) = \sum_{n=-\infty}^{\infty} p_n \phi_n(\psi) = \sum_{n=-\infty}^{\infty} p_n e^{jn2\pi\psi} = p_0 + \sum_{n=1}^{\infty} (p_{nc} \cos n2\pi\psi + p_{ns} \sin n2\pi\psi) \tag{2.5}$$

In the field of rotating machinery, the frequency defined by the time needed to complete a full revolution of the shaft (2π rad) is called the fundamental frequency, and the integer multiples of this frequency are called harmonic frequencies. The magnitude and phase of the complex coefficients p_n can be computed as follows:

$$|p_n| = \sqrt{p_{nc}^2 + p_{ns}^2} \tag{2.6}$$

$$\angle p_n = \arctan\left(\frac{p_{ns}}{p_{nc}}\right) \tag{2.7}$$

It is shown in Section 2.3.2 that each strain sensor has an individual relationship to torque. The Coleman transformation, Eqs. (2.3) and (2.4), combines the information from different strain sensors. A scaling or weighting factor was introduced to guarantee that all sensors have an equal contribution. To achieve these scaling factors the signals of each sensors were evaluated for complete revolutions of the input shaft. The strain signal from an individual strain sensor during a complete revolution of the input shaft is shown in Figure 2.6. The power spectrum of an individual strain signal is dominated by the fifth harmonic

component. This harmonic component can also be obtained from a Fourier series decomposition if we consider $\delta_s(t)$ is a periodic function of time with fundamental frequency of $\omega_0 = \frac{2\pi}{T}$, where T is the time needed to complete a full rotation of the input shaft. The Fourier series decomposition for the strain of each individual sensor as a function of time can be expressed as

$$\delta_s(t) = \sum_{n=-\infty}^{\infty} a_{sn}\phi_{sn}(t) = \sum_{n=-\infty}^{\infty} a_{sn}e^{jn\omega_0 t} = a_{s0} + \sum_{n=1}^{\infty}(a_{snc}\cos n\omega_0 t + a_{sns}\sin n\omega_0 t) \tag{2.8}$$

The complex coefficients a_{sn}, are the n^{th} harmonic component of the s^{th} strain sensor. Figure 2.15 shows a comparison between the raw strain signal of a single FBG, sensor number 01 (S01), and the fifth harmonic component during a complete revolution of the low-speed input shaft. Two different torque levels (25 % and 100 %) are plotted in Figure 2.15 to illustrate the effect of torque. Higher integer multiples of the fifth harmonic have a lower but significant contribution. For the calibration phase, tests were performed at 20 different torque levels, and the magnitude ($|a_{sn}|$) was computed for every full revolution measured using the following equation:

$$|a_{sn}| = \sqrt{a_{snc}^2 + a_{sns}^2} \tag{2.9}$$

The relationship between torque and the magnitude of the fifth harmonic of each sensor was investigated for all the 20 torque levels. Again, the low-speed shaft torque value was derived from the measurements of the test bench torque transducers located at the high-speed shafts. A regression polynomial was computed for each individual strain sensor fitting the $|a_5|$ values to the torque using the leas-squares criterion. Figure 2.16 shows the $|a_5|$ magnitude values of four different FBGs, for all revolutions of the input shaft measured during the 20 different load steps, against the average torque in the low-speed shaft during those revolutions. A linear, a quadratic, and a cubic fit of torque vs. $|a_{s5}|$ for each sensor s were realized to evaluate the linearity of each sensor; however, for clarity only the cubic fit is shown in Figure 2.16.

A good correlation was found for all 54 strain sensors between torque and the magnitude value of the fifth harmonic component, and therefore these $|a_{s5}|$ values were used to scale or weight the strain signals. For a full revolution of the input shaft, all sensors witnessed the same torque, and the signals of each strain sensors were scaled to have the same magnitude of the fifth harmonic component. The weighting factors were computed using the following expression:

$$w_s = \frac{1}{54}\frac{\sum_{i=1}^{54}|a_{i5}|}{|a_{s5}|} \tag{2.10}$$

Once every sensor is multiplied by its corresponding scaling factor, the weighted Coleman transformation can be written as follows:

$$p_{wnc}(t) = \frac{2}{54}\sum_{s=1}^{54} w_s\delta_s(t)\cos(n\psi_s(t)) \tag{2.11}$$

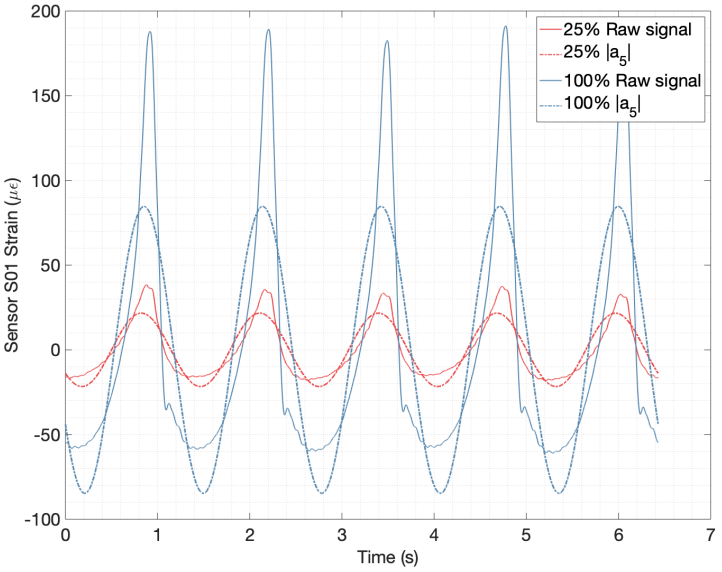

Figure 2.15: Original strain signal of sensor S01 for one shaft revolution vs. reconstructed signal using the fifth harmonic component a_5 (two load cases are compared with 25 % torque in red and 100 % torque in blue).

$$p_{wns}(t) = \frac{2}{54} \sum_{s=1}^{54} w_s \delta_s(t) \sin(n\psi_s(t)) \tag{2.12}$$

The magnitude and phase of the weighted complex coefficients p_{wn} can then be computed with equivalent expressions to Eqs. (2.6) and (2.7) as follows:

$$|p_{wn}| = \sqrt{p_{wnc}^2 + p_{wns}^2} \tag{2.13}$$

$$\angle p_{wn} = \arctan\left(\frac{p_{wns}}{p_{wnc}}\right) \tag{2.14}$$

The once-per-revolution pulse signal is obtained from the inductive sensor shown in Figure 2.4. The azimuth of the shaft is known when a pulse is detected, but it can only be interpolated between pulses. The assigned angle ψ_s was linearly interpolated between full revolutions of the input shaft. Attempts made to correlate the phase $\angle p_{wn}$ Eq. (2.14) with torque were not successful. A phase delay caused by the torsional deformation of the planet carrier was expected because the once-per-revolution pulse is measured at the rotor side flange of the planet carrier, and the strain sensors are placed in the middle section of the ring gear. However, the accuracy of the angular position was not good enough to characterize the effect of torque on $\angle p_{wn}$.

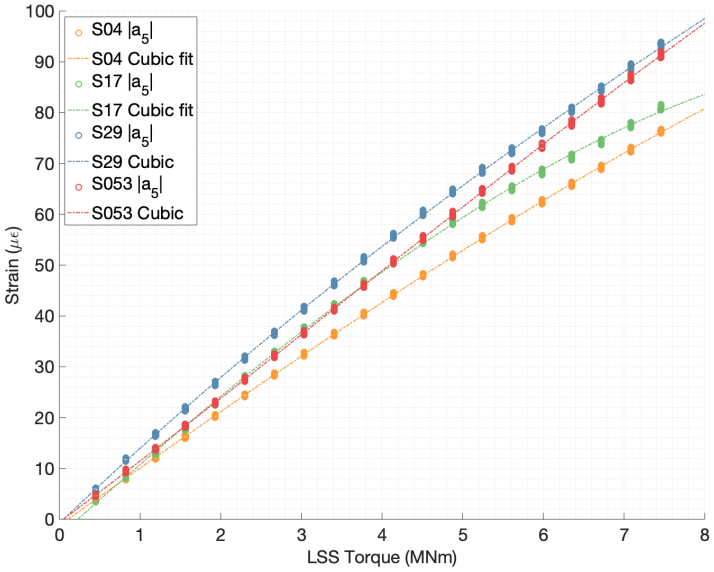

Figure 2.16: Magnitude of fifth harmonic $|a_5|$ of four strain sensors S04, S17, S29, and S53 vs. torque in low-speed shaft.

The azimuth angle of the shaft is not strictly needed to compute the magnitudes of the harmonic components. Since the 54 strains sensors are equally spaced around the outer circumference of the ring gear, the relative angle between the angular location of the sensors and the azimuth of the shaft ($\psi_s(t)$) can be substituted in Eqs. (2.11) and (2.12) by the fixed angular location of each sensor, denoted as ψ_{0s}. Figure 2.17 shows the magnitudes of the 5^{th}, 10^{th}, 15^{th}, and 20^{th} harmonic components ($|p_{w5}|$, $|p_{w10}|$, $|p_{w15}|$ and $|p_{w20}|$) plotted against the torque levels measured by the test bench torque transducers for all the revolutions measured during the calibration tests. A satisfactory correlation was found between the magnitude values of these harmonic components and torque.

2.4.1 Torque estimation procedure with a coordinate transformation

A graphical representation of the procedure to estimate torque using the Coleman coordinate transformation and the $|p_{w5}|$ magnitude value of all 54 weighted sensors is shown in Figure 2.18. The full procedure to estimate torque for every time sample can be summarized as follows.

- **Step 0** *Calibration phase.* Perform tests with known torque to learn the strain vs. torque behavior. For each test, compute the magnitude of the 5th harmonic component $|a_{s5}|$ of all the individual strain signals. Compute the scaling factors w_s. Weight scale the strain sensors so that all sensors have an equal magnitude of the fifth harmonic component for a given torque. Combine the weighted strain values of all 54 sensors and compute the magnitude of the fifth harmonic component for each

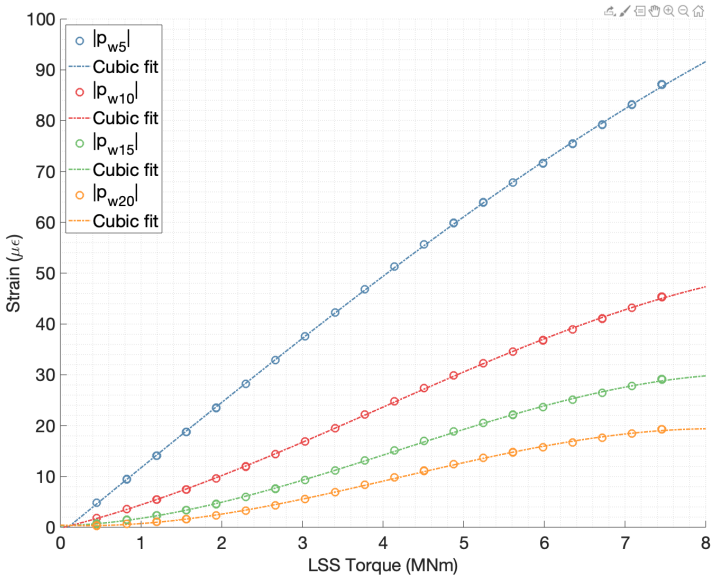

Figure 2.17: Magnitudes of the 5^{th}, 10^{th}, 15^{th}, and 20^{th} harmonic components of all 54 weighted sensors vs. torque in low-speed shaft.

available time sample $|p_{w5}|$. Find a regression polynomial between LSS torque and the magnitude of the fifth harmonic component of the combined strains.

- **Step 1** *Weight signals.* For a new test where strain data have been logged, apply the weighting factor to all the strain sensors.
- **Step 2** *Coordinate transformation.* For each time sample, apply the Coleman transformations to the weighted strain values to obtain $p_{wnc}(t)$ and $p_{wns}(t)$ using Eqs. (2.11) and (2.12) and compute the magnitude of the fifth harmonic component $|p_{w5}(t)|$ using Eq. (2.13).
- **Step 3** *Torque estimation.* Evaluate the regression polynomial to estimate torque from the combined magnitude of the fifth harmonic component of all 54 weighted instantaneous strain values.

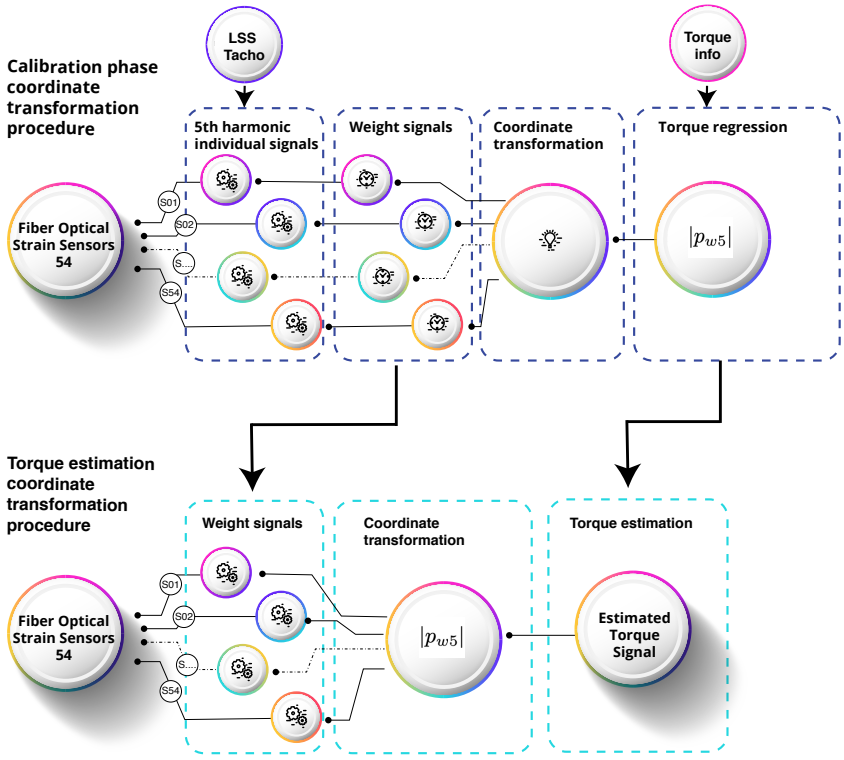

Figure 2.18: Torque estimation procedure based on a coordinate transformation.

2.5 Discussion

This section will discuss the main findings gathered during the development of the proposed method to measure input torque in wind turbine gearboxes. Torque estimation results obtained using data from two dynamic load tests will be analyzed to illustrate the key differences between the two alternative procedures presented in Sections 2.3 and 2.4.

Both procedures rely on a calibration phase, where the instrumented gearbox was operated under torque conditions known from other measurements. In the present study, 20 short tests with different stationary reference torque levels were performed to fit the strain to torque relationship (see Sections 2.3 and 2.4). Once the calibration phase had been accomplished, strain data were collected for tests with dynamic torque conditions. Figure 2.19 shows the estimated torque measurements during a test with a linearly increasing torque command. The torque estimate using peak-to-peak strain values is shown in blue, and the torque estimate using the coordinate transformation is shown in red. Figure 2.20 shows the torque estimates achieved for a test where the torque level was changed in steps. Starting from a middle value, the torque reference was changed to a lower and upper value. During both dynamic tests, the reference speed was kept constant. For clarity, a detailed window of 1 s is shown to compare the estimates of both tests.

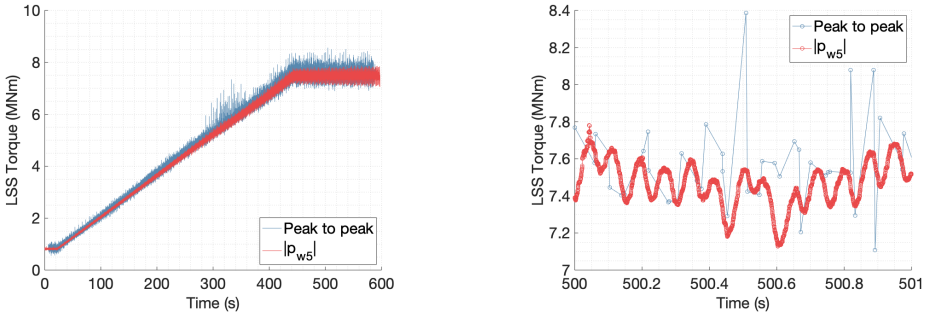

Figure 2.19: Torque estimates for a test with variable torque (ramp); results for entire test on in panel **(a)** and 1 s detail in panel **(b)**.

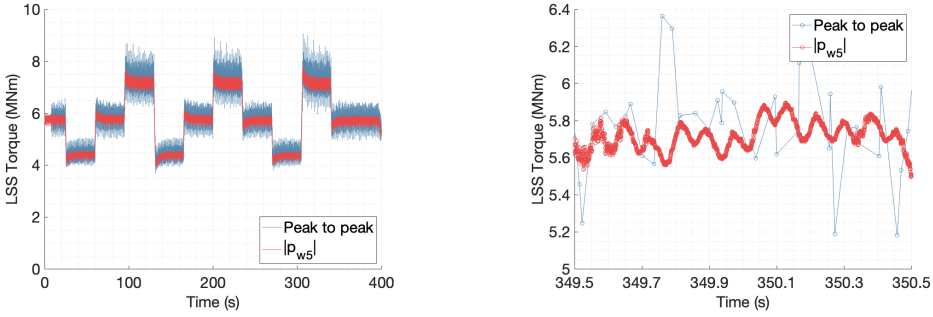

Figure 2.20: Torque estimates for a test with variable torque (steps); results for entire test on in panel **(a)** and 1 s detail in panel **(b)**.

- *Temporal resolution.*

  In the signal processing alternative based on peak values of strain, torque can only be evaluated when there is a gear mesh event between a planet and the ring. Therefore, the frequency resolution of the estimated torque depends on the planet-passage frequency of the first stage and the number of strain sensors used. The second signal processing strategy combines the simultaneous information of different strain sensors using a coordinate transformation. This allows tracking the magnitude of the harmonic components of the combined weighted strain values. With a total of 54 strain sensors equally spaced around the first-stage ring gear (see Figure 2.2), the gearbox input torque can be estimated for each available time sample, which results in a frequency resolution equal to the sampling frequency used to acquire the strain data. The difference in frequency resolution of the estimated torque from both procedures can be seen in the 1 s windows of Figure 2.19 and 2.20.

For future implementations of the method presented in this chapter, it is possible to achieve a trade-off between spatial resolution and frequency resolution, selecting the sampling frequency and the number of sensors. If a lower number of strain sensors was to be used, for example, if we halve the number of sensors to 26, then by taking two consecutive strain samples of each sensor, we can still compute the magnitude of the fifth harmonic component, and the resulting frequency resolution of the torque estimate would be half the sampling frequency used to acquire strain data. If the number of sensors is low, the accuracy of the magnitude of the fifth harmonic component has to be considered. In the extreme, with a single strain sensor, it would only be possible to evaluate the input torque once every revolution, which would result in a significantly lower temporal resolution.

- *Load sharing between planets (average and instantaneous K_γ).*

  The procedure based on peak-to-peak strain values allows for exploration of how the load is shared between planets. An inductive sensor was added to the instrumentation to provide a once-per-revolution pulse, making the mesh sequence of planets known. Therefore, it is possible to assign peak-to-peak values to individual planets. The load share between planets can be computed using Eq. (2.2). However, in the setup presented in this chapter, the number of strain sensors is not an integer multiple of the number of planets. When a strain peak caused by the gear mesh of a planet is detected in a given strain sensor, the rest of the strain sensors do not observe the peaks caused by the mesh of the other planets simultaneously. Therefore, only an average K_γ (planet load share factor) can be extracted for each measurement position, and the true instantaneous load sharing between planets could not be evaluated. In the procedure based on peak-to-peak strain values, knowledge of the instantaneous load sharing between planets is needed to estimate the dynamic torque value. The instantaneous torque value was approximated, assuming that the instantaneous value of K_γ is equal to the average. A larger variation of torque was observed in the torque estimates produced by the peak-to-peak procedure shown in Figs. 2.19 and 2.20. The authors believe that the approximation made for K_γ is the main reason to justify the larger torque variations. Since the average K_γ is used, if the instantaneous load sharing between planets is worse than the average (higher instantaneous K_γ values), the torque variations would be overestimated.

- *Sensing of shaft's azimuth angle and real-time capability.*

  The fact that a complete revolution of the input shaft has to be measured in the signal processing alternative based on peak-to-peak strain values to assign the suitable planet to the detected strain peaks is also responsible for the delay in the peak-to-peak torque estimates shown in Figs. 2.19 and 2.20. Torque can only be evaluated after the first pulse of the input shaft inductive sensor is detected when the peak-to-peak procedure is used. On the other hand, the procedure based on the coordinate transformation can be accomplished without the inductive sensor because the azimuth angle of the shaft is not needed to compute the magnitude of the harmonic components. This can simplify the instrumentation setup and enable estimating torque in real-time.

- *Weighting of individual strain sensors.*

  An important finding during the calibration phase of both processing strategies was that each measurement location showed a slightly different sensitivity to torque (see Figs. 2.8, 2.10, 2.14, and 2.17). Several factors can play a role in explaining this. On one hand, installing the strain sensors is a manual process, and differences in how the fibers are glued to the surface of the ring gear and small positioning errors are expected. On the other hand, the ring gear is connected to structural gearbox components with highly asymmetric stiffness. This lack of symmetry is most pronounced for the FBG sensors close to the torque reaction arms in the housing on the rotor side of the ring gear, shown in Figs. 2.3 and 2.4. Because of the reasons mentioned above, differences in stiffness are expected. However, the difference in the linearity of the torque-strain relationship is not fully understood by the authors yet. In any case, it is possible to achieve a satisfactory fit for all measurement points by increasing the order of the regression polynomial, and therefore an accurate torque estimate can be achieved. To compensate for the different sensitivity of each measurement location, we have used the average magnitude of the fifth harmonic component of the individual strain signals as a basis for weighting the strain values. All 54 sensors are weighted to exhibit the same relationship to torque. This makes it possible to combine the sensors.

- *Accuracy.*

  In the experimental setup used for this study, a direct torque measurement in the input shaft was not available, the torque transducers were installed in the high-speed shafts, and therefore a quantitative evaluation of the torque estimates could not be performed. For future work, a direct comparison between the method presented in this study and a calibrated direct measurement is suggested.

  In the signal processing alternative based on the Coleman transformation, the weighted strain values of all the sensors are combined to compute the magnitude of the fifth harmonic component for each available time sample $|p_{w5}(t)|$. The torque is estimated using the regression polynomial between LSS torque and $|p_{w5}|$. Figure 2.17 shows that higher-order harmonics (10, 15, and 20) can also be correlated with torque. The procedure presented in this chapter could be extended to consider these magnitudes and combine them to achieve higher accuracy torque estimates. Again, a quantitative analysis of the accuracy of the estimates could not be performed with the instrumentation setup available and is recommended for future work.

Finally, it is worth noting that the potential effect that non-torque loads could have on the method presented in this study could not be evaluated. The test bench used to run the experiments (see Section 2.2.2) is a back-to-back gearbox test bench where only torque and speed can be controlled. The effect of these non-torque loads in four-point-mount gearboxes is expected to be small. However, to fully demonstrate the applicability of the presented methodology in a wind turbine installation, it is suggested to investigate the behavior of the presented method in a test bench with non-torque loading capabilities, i.e., axial forces and bending moments. Other research topics like the real-time processing capability and the long-term behavior of the calibration also need to be addressed to develop this method for use in serial production wind turbines.

2.6 Conclusions

This chapter develops a new method to measure the input rotor torque of wind turbine gearboxes. The proposed method is based on strain measurements of the static first-stage ring gear. Measuring in the static frame overcomes the main drawback of traditional methods, which measure the strain of rotating components. Fiber-optic strain sensors were used because they offer a higher signal-to-noise ratio, are immune to electromagnetic interference, and allow a more straightforward installation because multiple strain sensors can be accommodated in a single fiber.

A satisfactory correlation was found between the strain signals measured on the static first-stage ring gear and torque. Two signal processing strategies have been presented in this chapter for determining input rotor torque. The first is based on the peak-to-peak strain values assigned to the gear mesh events. The second is based on a coordinate transformation of all the strain signals, followed by tracking the magnitude of the fifth harmonic component. Torque estimation results obtained using both signal processing alternatives were presented and analyzed in Section 2.5 for two tests with dynamic torque conditions. The procedure based on the peak-to-peak strain values of the gear mesh events can only estimate torque when a gear mesh event is detected. The strain peak-to-peak values can be assigned to individual planets using an additional inductive displacement sensor that provides a once-per-revolution pulse, and therefore the load sharing between planets can be explored. With the second procedure, based on a Coleman coordinate transformation, it is possible to estimate torque whenever strain data of all sensors are available, leading to an improved frequency resolution up to the sampling frequency used to acquire strain data.

For future work, a direct comparison between the method presented in this study and a calibrated direct torque measurement, on the input shaft, is suggested to assess the accuracy of the new method quantitatively. The present study is based on measurements taken on a gearbox back-to-back test bench where only torque and speed can be controlled. The effects of non-torque loads, i.e., axial forces and bending moments, need to be researched to fully demonstrate the applicability of the presented methodology in a wind turbine installation.

The method presented in this chapter could make measuring gearbox torque more cost-effective, facilitating its adoption in serial wind turbines. This is important since accurate knowledge of the input torque is key to improving gearbox reliability. Furthermore, implementing a torque measurement on each serial wind turbine would permit novel data-driven control strategies, which can improve drivetrain loading. Having an accurate measurement of the input torque throughout the service history of the gearbox would also enable an improved assessment of the consumed fatigue life of the gearbox components. This knowledge could lead to future design improvements, which would, in turn, lead to higher reliability and lower cost of energy.

3

Identification of operational deflection shapes of a wind turbine gearbox using fiber-optic strain sensors on a serial production end-of-line test bench

Wind energy has witnessed a staggering development race, resulting in higher torque density demands for the drivetrain in general and the gearbox in particular. Accurate knowledge of the input torque and suitable gearbox models are essential to ensure reliability, but neither of them is currently available in commercial wind turbines. The present study explores how a subspace identification algorithm can be applied to fiber-optic strain sensors on a four-stage gearbox to obtain operational deflection shapes. An innovative measurement setup with 129 fiber-optic strain sensors has been installed on the outer surface of the ring gears to research the deformations caused by planet gear passage events. Operational deflection shapes have been identified by applying the multivariable output-error state space (MOESP) subspace identification method to strain signals measured on a serial production end-of-line test bench. These operational deflection shapes, driven by periodic excitations, account for almost all the energy in the measured strain signals. Their contribution is controlled by the torque applied to the gearbox. From this contribution, a torque estimate for dynamic operating conditions has been derived. Accurate knowledge of the input torque throughout the entire service life allows for future improvements in assessing the remaining useful life of wind turbine gearboxes.

3

This chapter is based on the following publication: *U. Gutierrez Santiago. Identification of operational deflection shapes of a wind turbine gearbox using fiber-optic strain sensors on a serial production end-of-line test bench* [36]. Blue is the third color of the rainbow when arranged by increasing wavelength. Blue has a wavelength between 450 nm and 495 nm. Humans have used minerals as colorants for aesthetic purposes since prehistoric times. The bonding properties of materials determine the wavelength and efficiency of light absorption, while light of other wavelengths is reflected, defining the color we observe. The appearance of pigments is sensitive to the source of light, with sunlight being the standard for white light due to its high color temperature and uniform spectrum. One of the most special pigments ever used is ultramarine blue, which is derived from *lapis lazuli* gemstones. These stones, primarily found in the mines of Afghanistan, undergo an intricate process of grinding and separation to extract the coveted blue pigment. This labor-intensive method, combined with the limited availability of the gemstone, made ultramarine blue an exclusive and exorbitantly priced commodity. It was reserved for elite European painters, including Reinsassance artists Raphael (1483 – 1520), Leonardo da Vinci (1452 - 1519), and Michelangelo (1475 - 1564). The celebrated artist from Delft, Johannes Vermeer (1632 – 1675), made extensive use of ultramarine in his paintings. The turban of the *Girl with a Pearl Earring* is painted with a mixture of ultramarine and lead white, with a thin glaze of pure ultramarine over it.

3.1 Introduction

The growth of wind energy in the last few decades has been remarkable. The Global Wind Energy Council (GWEC) reported 93.6 GW of new wind energy capacity installed in 2021, 72.5 GW onshore and 21.1 GW offshore, bringing the worldwide cumulative wind power capacity to 837 GW [85]. That is a 3.5 times increase in the last 10 years from a global capacity of 237.7 GW in 2011 and a staggering 35 times increase in 20 years from a total capacity of 23.9 GW in 2001 [3]. The projected market growth for the coming years and decades is even larger. In 2022, the International Renewable Energy Agency (IRENA) and International Energy Agency (IEA) published a road map for the energy sector to become net zero by 2050, with the aim of limiting the rise in global temperatures to 1.5℃ [6]. According to this proposal, the annual capacity additions of wind energy should reach 390 GW by 2030, 310 GW onshore and 80 GW offshore. This means increasing the yearly installations more than 4 times compared to the ones recorded in 2021 and more than 5 times compared to the average over the last 3 years [6].

To facilitate such rapid growth, the main focus of industry and academia has been lowering the levelized cost of energy (LCoE) from wind [7]. This push to lower the LCoE has resulted in a race from wind turbine manufacturers to increase the rotor diameter, power rating, and hub height of wind turbines. The evolution of size in offshore turbines has been even more dramatic because they have less stringent logistic constraints [8]. To illustrate the pace of growth, the average values of wind turbines installed during the years 2011, 2016, and 2021 are summarized in Table 3.1. Power rating, rotor diameter and hub heights were provided in the yearly cost of energy reviews [33–35]. The trend to increase power ratings, rotor diameter, and hub heights can be understood from a wind turbine's fundamental power generation equation [9]. The power produced by a wind turbine is proportional to the air density, the power coefficient, the cubic exponent of the wind speed and the area swept by the rotor. Increasing the hub height reduces the influence of surface friction on the wind conditions witnessed by the rotor, allowing wind turbines to operate in higher-quality resource regimes where wind velocities are higher. There are several reasons for the increase in the rotor diameter of wind turbines. Larger rotors capture more energy. The increase in energy captured by the rotor is bigger than the increase in overall turbine costs because blade lengths can be increased while many other costs remain fixed, generally leading to lower LCoE in larger turbines. More powerful turbines allow for fewer turbine installations for a given power plant capacity, lower balance-of-system costs, and fewer moving parts, therefore enhancing the reliability of the wind plant. In addition, increasing the size of the rotor relative to the generator rating allows for lowering the rated wind speed and operating more frequently at full power, resulting in a higher capacity factor.

If we assume a constant blade tip speed, torque will increase with the cube of the rotor diameter. From the yearly average power rating and rotor diameter values provided by [33], [34], and [35] we estimated the associated rotor torque using the maximum tip speed figures provided in the yearly reviews, which are 80 m/s for onshore turbines and 90 m/s for offshore turbines. These torque values have been added to Table 3.1 and show that the rotor torque of the installed turbines has increased more than 3 times onshore and more than 3.3 times offshore in a time period of just 10 years. This rate of development is unprecedented in any other industry or engineering application and ensuring turbine

reliability remains a top priority [10].

Table 3.1: Average onshore and offshore wind turbine power rating, rotor diameter, hub height, input torque, and torque density.

	Onshore			Offshore		
Year	2011	2016	2021	2011	2016	2021
Power rating (MW)*	1.5	2.2	3.0	3.6	4.71	8.0
Rotor diameter (m)*	82.5	108	127	107	128	159
Hub height (m)*	80	84	95	90	93.7	102
Rotor torque (MNm)**	0.77	1.46	2.38	2.14	3.35	7.07
Torque density (kg/Nm)**	70	100	130	140	150	200

* Power rating, rotor diameter and hub height data from [33], [34], [35].

** Input torque and torque density estimated by the authors.

Torque is the main sizing factor for the drivetrain and the gearbox. The drivetrain makes a large contribution to the capital expenditure of the turbine and also affects other turbine costs because increasing the tower-top mass has an impact on the main frame, tower, and foundation. The pressure to lower costs and the size constraints due to handling and logistic limitations have translated into higher torque density demands for wind turbine gearboxes. The torque density values in Table 3.1 have been estimated using equivalent-gearbox models for such power ratings and hub diameters [39]. The increase in torque density witnessed in just a decade is enormous. Thanks to multiple technological innovations, torque densities of 200 Nm/kg are now considered state-of-the-art by different gearbox manufacturers [37–39]. For such high torque ratings and torque density values, a trend has emerged in new gearbox architectures towards more planetary stages and more planets per stage. In wind turbines with a power rating of up to 2 MW, the most widely used gearbox architecture comprises a single planetary stage and two parallel gear stages [40]. In the range from around 2 MW to 6 MW, gearboxes with two planetary stages and a single parallel stage have become mainstream. For higher power ratings, gearboxes with three planetary stages are expected to become dominant. Due to the large number of planets in the input stages and the limitations in outer diameter, the space available for planet bearings has decreased to a point where journal bearings have to be adopted because there is not enough space for roller element bearings [12].

Overall, gearbox complexity is increasing in the pursuit of lighter designs, while maintaining gearbox reliability is mandatory to ensure low operational expenses. Two key factors are essential to achieve successful designs. On the one hand, accurate knowledge of the loading conditions throughout the complete service life of the gearbox is crucial. On the other, accurate models are required to predict its performance and maintenance requirements. Unfortunately, sensors that provide detailed load measurements of the turbine during commercial operation are not generally available [41]. It is possible to estimate the input gearbox torque from the electric currents in the generator, but normally, this information is only available through the supervisory control and data acquisition (SCADA) system, and it cannot capture the torque fluctuations caused by the dynamic wind turbine

operation, especially in damaging events like emergency brake events [43]. Even in normal operation, relatively large errors are expected when using generator currents because the power losses in the generator and the gearbox vary with torque and other operating conditions and are generally unknown.

As a consequence, a direct measurement of the actual torque is needed. The traditional method to measure torque, based on strain gauges on the rotating shaft, is considered impractical for commercial wind turbines due to the expensive nature of the equipment required and is not suitable for long-term applications [47]. The need for novel sensing technologies and measurement techniques that facilitate a fleet-wide implementation of torque measurements has resulted in great research interest. Zhang et.al. explored alternative direct measuring techniques and discussed the associated technical and economic difficulties [78]. An alternative direct measurement method, based on deformation measurements on the outer surface of the first-stage ring gear of the gearbox, was proposed by the authors of this work [86]. Other researchers have focused on indirect techniques or so-called virtual sensors where a model of the system is combined with data from sensors in other locations of the turbine to obtain estimated data of the input torque [47–51]. These virtual sensing approaches require accurate wind turbine and drivetrain models but the complexity of current designs exceeds modeling capabilities [10]. Costly experimental evaluation is needed to achieve the desired degree of confidence [87]. Data-driven modeling techniques, also referred to as system identification in the systems and controls community, provide a framework to estimate models of dynamical systems when the accuracy of physical models derived from first principles is unsatisfactory. System identification is well-established in mechanical structures [88], where it is more widely referred to as experimental modal analysis (EMA). EMA relies on measuring a controlled applied force, either with an instrumented impact tool or with a shaker, to identify frequency response functions and modal parameters from the system response. However, in the case of large structures, it is difficult to excite the system with enough energy to produce measurable outputs. Operational modal analysis (OMA) is an alternative output-only approach that overcomes the difficulty of exciting the system by relying on ambient broadband excitation. There is a trend to replace EMA with OMA because in OMA the excitation and boundary conditions of the system are those seen in operation and are deemed more representative of the structure's real use in service [89]. In the specific case of rotating machinery like wind turbine gearboxes, several factors impede using OMA [90]. Most notably, the input excitation is unknown and may not adequately excite all modes of interest [91], and the premise of having a white noise excitation in the frequency range of interest is violated because periodical loads due to rotating elements act on the system and typically dominate the system response [92]. Research interest in overcoming these difficulties has increased recently, and many different algorithms have been proposed. The main algorithms used for wind turbines were reviewed by Van Vondelen et al. [93] and classified using nine suitability criteria. These criteria included the accuracy of the algorithms, the ability to distinguish closely spaced modes, computational complexity, and the ability to handle periodic stationary and non-stationary excitation or harmonics. When structural modes and harmonics are widely separated and when the rotor speed is constant over time, harmonics are identified by the OMA algorithms as artificial modes with zero damping.

The main contributions of this chapter are as follows:

- We develop and describe a novel measurement setup for a wind turbine gearbox comprising 129 fiber-optic strain sensors installed and distributed around the ring gears of the three planetary stages, and we present the results of measurements performed in a serial end-of-line test bench.
- We apply the multivariable output-error state space (MOESP) method to identify the periodic modes, referred to as operational deflection shapes, which has enabled quantifying the unknown periodic excitations and has been found to provide an estimation of the input torque of the gearbox.

Accurate knowledge of the input torque throughout the entire service life is paramount to assessing the consumed fatigue life of the gearbox, and tracking operational deflection shapes recursively over time can potentially be used as an indicator of fault detection. The remainder of the chapter is structured as follows. In Section 3.2, the chosen identification framework is motivated, and the key definitions and formulation are provided. In Section 3.3, we describe the measurement setup and the test wind turbine gearbox together with the experimental conditions. In Section 3.4, the key findings of using subspace identification on strain signals are described, and finally, Section 3.5 presents the main conclusions of this work, and recommendations are given for future work.

3.2 Formulation of the subspace system identification method

This section describes the theoretical formulation used to identify operational deflection shapes from strain data collected by fiber-optic sensors. Starting from the state space representation used, we justify how the periodic inputs can be modeled within the system matrix, leading to a stochastic identification problem. Once the system matrices describing the dynamic behavior have been estimated, up to a similarity transformation, we show how the state and output measurements can be reconstructed using a Kalman filter.

We assume that the system to be identified is a finite-dimensional, linear, time-invariant system, subject to measurement and process noise, which has been sampled at $t = \tau k$, where τ is the time step and k is an integer, with a general discrete-time state space representation given by

$$x_{k+1} = Ax_k + Bu_k + w_k, \tag{3.1}$$

$$y_k = Cx_k + Du_k + v_k, \tag{3.2}$$

where $x_k \in \mathbb{R}^n$, $u_k \in \mathbb{R}^{n_u}$,$w_k \in \mathbb{R}^n$, $y_k \in \mathbb{R}^{n_y}$, and $v_k \in \mathbb{R}^{n_y}$ are the state, input signal, process noise, output signal, and measurement noise, respectively [94]. The assumption of a linear time-invariant system is considered valid when the gearbox operates close to rated torque conditions. Under these operating conditions, contact patterns in the gear flanks are fully developed, and non-linear effects like backlash or material properties related to the torque reaction arm elastomers are not expected to play a role. The matrices $A \in \mathbb{R}^{n\times n}$, $B \in \mathbb{R}^{n\times n_u}$, $C \in \mathbb{R}^{n_y\times n}$ and $D \in \mathbb{R}^{n_y\times n_u}$ are the system, control, sensor, and output matrices, respectively.

The system dimension or order of the system is n, and the dimension of the output vector y_k is the number of measured response signals n_y.

Operational modal analysis relies on ambient broadband excitation and assumes this excitation is random white noise in the frequency range of interest. In this case, no deterministic input is considered (i.e., $u_k = 0$), which leads to the so-called stochastic realization problem. In wind turbine gearboxes, and rotating machinery in general, this premise is severely violated because the periodic action of shafts and gears dominates the system response. Gres et al. showed that it is possible to extend the stochastic realization to OMA under (unknown) periodic excitations [95] by modeling the effect of a deterministic periodic force as a sum of a finite number of h sinusoidal frequency components such that $u(t)$ has the following shape:

$$u(t) = \sum_{i=1}^{h} a_i \sin(\omega_i t + \phi_i), \tag{3.3}$$

where $a_i, \omega_i, and \phi_i \in \mathbb{R}$ are the unknown amplitude, frequency, and phase of the i^{th} periodic input component. These components can become part of a combined state vector to eliminate the periodic input component from Eqs. (3.1)-(3.2). The following periodic state vector can be defined:

$$x^{\text{per}}(t) = \begin{bmatrix} a_1 \sin(\omega_1 t + \phi_1) \\ a_1 \cos(\omega_1 t + \phi_1) \\ a_2 \sin(\omega_2 1t + \phi_2) \\ a_2 \cos(\omega_2 t + \phi_2) \\ \vdots \\ a_h \sin(\omega_h t + \phi_h) \\ a_h \cos(\omega_h t + \phi_h) \end{bmatrix} \in \mathbb{R}^{2h}, \tag{3.4}$$

which enables the state space model in Eqs. (3.1)-(3.2) to be rewritten as a combined state space model without the periodic input $u(t)$ as

$$\begin{bmatrix} x_{k+1} \\ x_{k+1}^{\text{per}} \end{bmatrix} = \begin{bmatrix} A & A^{\text{B}} \\ 0 & A^{\text{per}} \end{bmatrix} \begin{bmatrix} x_k \\ x_k^{\text{per}} \end{bmatrix} + \begin{bmatrix} w_k \\ 0 \end{bmatrix}, \tag{3.5}$$

$$y_k = \begin{bmatrix} C & C^{\text{per}} \end{bmatrix} \begin{bmatrix} x_k \\ x_k^{\text{per}} \end{bmatrix} + v_k. \tag{3.6}$$

The matrices A and C are the original system or structural matrices, and the matrices A^{per} and C^{per} correspond to the periodic unknown inputs. The matrix A^B is a mapping from the periodic states at time index k into the system or structural states at time index $k+1$. Due to the upper-right block structure of the state matrix, the eigenvalues of the combined system are the combined set of eigenvalues of A^{sys} and A^{per}. While the eigenvectors of the combined state matrix regarding the structural part become $\begin{bmatrix} \Phi_i^T & 0 \end{bmatrix}^T$, the resulting mode shapes are Ψ_i. For a full derivation, interested readers are referred to [95]. This approach has been successfully applied to an operational offshore wind turbine and has

been shown to provide accurate estimates of the first three tower bending modes [96]. The unknown periodic excitations in Eqs. (3.1)-(3.2) can become part of a combined state vector yielding an equivalent state space realization shown in Eqs. (3.5)-(3.6) without the periodic input $u(t)$. The extended system matrix $\bar{A}$ can be defined as

$$\bar{A} = \begin{bmatrix} A & A^{\mathrm{B}} \\ 0 & A^{\mathrm{per}} \end{bmatrix}. \tag{3.7}$$

Assuming the system admits an innovation state space representation [94], we can rewrite Eqs. (3.5)-(3.6) as

$$\bar{x}_{k+1} = \bar{A}\bar{x}_k + \bar{K}e_k, \tag{3.8}$$
$$y_k = \bar{C}\bar{x}_k + e_k, \tag{3.9}$$

where the innovation signal e_k is assumed to be an ergodic white noise sequence and the matrix $\bar{K}$ is the Kalman gain.

This extended system matrix $\bar{A}$ is composed of A the original or structural system matrix. It combines the periodic and structural modes, which, due to the upper-right block structure, can be distinguished because the eigenvalues of the periodic part correspond to undamped modes on the unit circle. The objective of system identification is to estimate the matrices $\bar{A}$ and $\bar{C}$, up to a similarity transformation, using only the output measurement y_k. For the present study, the multivariable output-error state space (MOESP) subspace method was chosen because it has been shown to provide asymptotically unbiased estimates of model parameters as long as the system input has adequate persistency of excitation [97] and the RQ factorization enables a computationally efficient implementation. Furthermore, using instrumental variables, it is possible to deal with process and measurement noise. A full description and proofs of the algorithm are given in [94], and the implementation shown in this chapter was accomplished using the LTI System Identification Toolbox for Matlab® [98]. The user must define three key parameters when realizing the MOESP algorithm:

1. N - the number of samples for each of the signals;
2. s - the number of block rows, used to construct the Hankel matrices;
3. n - the model order.

The matrices $\bar{A}_T$ and $\bar{C}_T$ are the estimates, up to a similarity transformation of $\bar{A}$ and $\bar{C}$. That is, $\bar{A}_T$ has the same eigenvalues as the matrix $\bar{A}$ and the system $(\bar{A}_T, \bar{C}_T)$ has the same input—output behavior as the original system $(\bar{A}, \bar{C})$. These linear transformations are given by: $T^{-1}\bar{A}T$, $\bar{C}T$ and $T^{-1}\bar{K}$ with $T \in \mathbb{R}^{n\times n}$. The transformed state is such that $\bar{x} = Tx$. With a suitable transformation matrix, it is possible to transform the system (A_T, C_T) into the so-called modal form with a diagonal state-transition form or combine complex-conjugate pole pairs to form a real, "block-diagonal" system in which $\bar{A}_M$ has two-by-two real matrices along its diagonal. The dynamics of the system are completely characterized by the eigenvalues (poles) and the observed parts of the eigenvectors (mode shapes) of the $\bar{A}_M$ matrix. The eigenvalue decomposition of $\bar{A}_M$ is given by:

$$\bar{A}_M = [\Phi][\Lambda][\Phi]^{-1}. \tag{3.10}$$

For oscillatory systems, the λ_i values are complex. The pole locations govern the system response. Poles inside the unit circle, $|\lambda_i| < 1$, give stable and convergent responses and are also called damped modes. Poles outside the unit circle, $|\lambda_i| > 1$ have unstable responses. When a pole is on the unit circle, $|\lambda_i| = 1$, the system exhibits a sustained oscillation (lossless), referred to as undamped. In this case, the state variable x_i oscillates sinusoidally at some frequency ω_i, where$\lambda_i = e^{j\omega_i T}$.

The observed part of the i^{th} system eigenvector $\{\phi_i\}$ is the mode shape $\{\Psi_i\}$ at the sensor locations given by:

$$\{\Psi_i\} = \left[\bar{C}_M\right]\{\Phi_i\}. \tag{3.11}$$

Both the state and the output measurements can be reconstructed using the so-called one-step-ahead predictor using the identified system and output matrices in modal form $(\bar{A}_M, \bar{C}_M)$ and the transformed Kalman filter $(\bar{K}_M)$:

$$\hat{x}_{k+1} = (\bar{A}_M - \bar{K}_M\bar{C}_M)\hat{x}_k + \bar{K}_M y_k, \tag{3.12}$$

$$\hat{y}_k = \bar{C}_M\hat{x}_k, \tag{3.13}$$

where $\hat{x}_{k+1}$ is the predicted state at time index $k+1$ and $\hat{y}_k$ denotes the predicted measurement vector for time index k.

As a means of cross-validation, different datasets were used for identification and validation. As a quality measure, we used the variance accounted for (VAF), which gives a measure of how well the linear model predicts the variability of the output signal. The *mathrmVAF* is defined for each individual sensor signal and is expressed as

$$\text{VAF}_s = \left(1 - \frac{\text{Var}(y_s - \hat{y}_s)}{\text{Var}(y_s)}\right) \times 100\ \%, \tag{3.14}$$

where $\hat{y}_s$ is the output predicted by the identified model for the s^{th} sensor, y_s is the actual measurement for the s^{th} sensor, and Var denotes the variance.

3.3 Experimental setup

This section describes the experimental setup used for the present study. First, the main characteristics of the gearbox used for identification are described. Then, details of the fiber-optic strain sensors used and their location on the outer surface of the ring gears are shown. Lastly, the test bench used and the specifications of the tests performed for identification and validation are presented.

3.3.1 Gearbox description

The wind turbine gearbox used for the present study is a four-stage gearbox manufactured by Gamesa Gearbox with a reference torque of 8 MNm. It is considered a suitable example of the gearbox architecture expected to dominate high-end power ratings; see Section 3.1. The gearbox has a configuration comprised of three planetary stages followed by a parallel

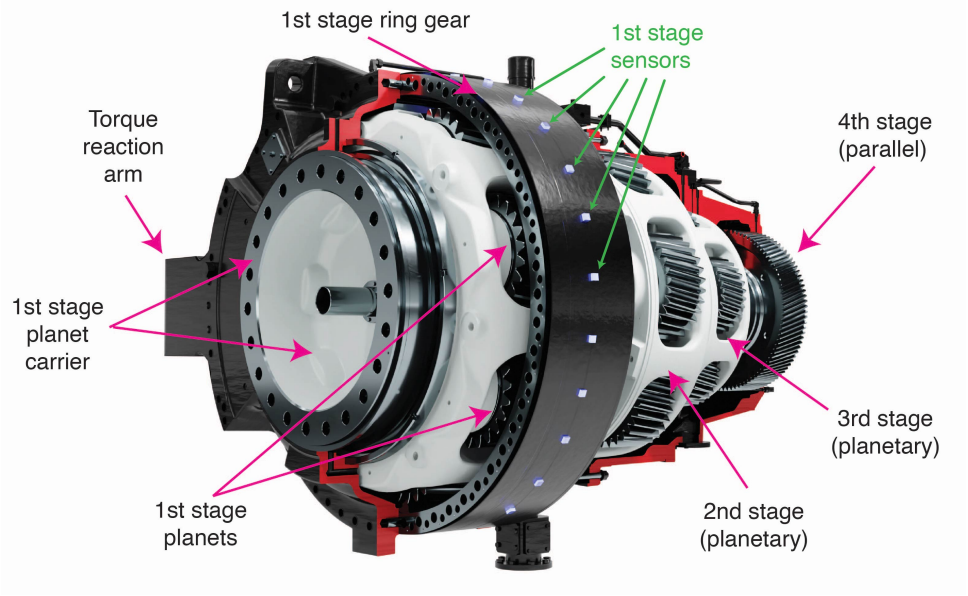

Figure 3.1: A 3D Representation of the tested gearbox with fiber-optic strain sensors on the outer surface of the first-stage ring gear. Adapted from Gamesa Gearbox (`https://www.gamesagearbox.com/wind-technology/`).

helical gear stage. The four stages together provide a total gear ratio of 179.576. Figure 3.1 shows the arrangement of all the stages in the gearbox with the rotor on the left side of the picture. For clarity, only the first-stage ring gear has been fully drawn. The first input stage is a planetary stage with seven planets and has a ring gear with an outer diameter of 2107 mm. The first-stage sun is connected with a spline to the second-stage planet carrier that contains six planets. The outer diameter of the second-stage ring gear is 1790 mm. The third stage has five planets and a ring gear with an outer diameter of 1428 mm. The total weight of the gearbox is approximately 38950 kg, which yields a torque density of 205 Nm/kg. The planets from the first and second stage are supported by journal bearings instead of roller element bearings due to the space constraints created by the very large number of planets. The known excitation frequencies can be computed using the rotational speed and the number of teeth of the gears. The rotational frequencies of the planet carriers, the planet-passing frequencies of each stage, and the gear mesh frequencies are summarized in Table 3.2. These frequencies correspond to the nominal speed of 8.35 rpm in the first-stage planet carrier, which is the low-speed or input shaft.

3.3.2 Fiber-optic strain sensors

Three arrays of fiber-optic strain sensors based on fiber Bragg gratings (FBGs) were wrapped around the planetary stage ring gears. The sensor placement was designed taking into account the insights gained in [86], which demonstrated that because the rims are relatively thin significant strains can be measured on the outer surface of the ring gears. In total,

Table 3.2: Rotational and gear mesh frequencies of the gearbox at nominal speed.

Abbreviation	Description	Frequency (Hz)	Order of low-speed shaft (LSS)
PC1	Rotational frequency of first planet carrier	0.1392	1.0000
7xPC1	Planet-passing frequency of first stage	0.9748	7.0000
PC2	Rotational frequency of second planet carrier	0.4603	3.3056
6xPC2	Planet-passing frequency of second stage	2.7619	19.8334
PC3	Rotational frequency of third planet carrier	1.7169	12.3288
5xPC3	Planet-passing frequency of third stage	8.5843	61.6441
HSIS	Rotational frequency of high-speed gear wheel	7.5542	54.2468
HSS	Rotational frequency of high-speed gear pinion	25.0070	179.5758
GMF1	first-stage gear mesh frequency	11.5583	83.0000
GMF2	Second-stage gear mesh frequency	46.4922	333.8614
GMF3	Third-stage gear mesh frequency	145.9335	1047.9504
GMF4	Fourth-stage gear mesh frequency	725.2035	5207.6966

12 optical fibers were installed on the test gearbox, four on each ring gear. A number of grooves were machined on the external diameter of the ring gears, in the middle section across the width of the gear between the rotor and generator side faces, to facilitate the installation process and protect the sensors during assembly and testing. Machining the grooves by turning provided a smooth finish that guaranteed an adequate bonding between the fiber and the ring gear. Figure 3.2 shows the detailed location of the 42 strain sensors distributed on the outer perimeter of the first-stage ring gear. The number of sensors was defined as a multiple of the planets, equally spaced around the perimeter, to ensure that the mesh events caused by the seven planets could be detected synchronously by the strain sensors. The labels of the strain sensors have been colour-coded to represent the fiber in which the FBG was accommodated. The spacing between FGBs within each fiber was designed so that all fibers cover the complete perimeter of the ring. This was done to prevent losing a portion of the ring gear in case of damage to a fiber. However, all the fibers survived the complete measurement campaign satisfactorily, including assembly and disassembly operations. Sensor placement on the second- and third-stage ring gears is shown in Figures 3.3 and 3.4, respectively. The fiber optical sensors were supplied and installed by the company Sensing360 B.V. [80]. Figure 3.5 shows the three ring gears used for the present work before installing the sensors, and Figure 3.6 gives a detailed view of the sensor placement on the third ring gear together with the fiber routing and connectors. For a detailed description of the measurement principle and properties of fiber-optic strain sensors based on FBGs, the interested reader is referred to previous work by [86].

In each of the planetary stages, in addition to the fiber-optic strain sensors, inductive displacement sensors were installed to provide a pulse once per revolution of the planet carrier. The purpose of these sensors was to know the planet carrier's relative position to the strain sensors to identify which planet is responsible for the strain peaks observed in the strain signals. The relative positions of the target and the inductive sensor or pick-up are shown in Figures 3.2 to 3.4. During the experiments, torque measurements from torque transducers installed in the high-speed shaft coupling of the test bench were logged synchronously with the fiber-optic strain data and the tachometer signals of all three stages.

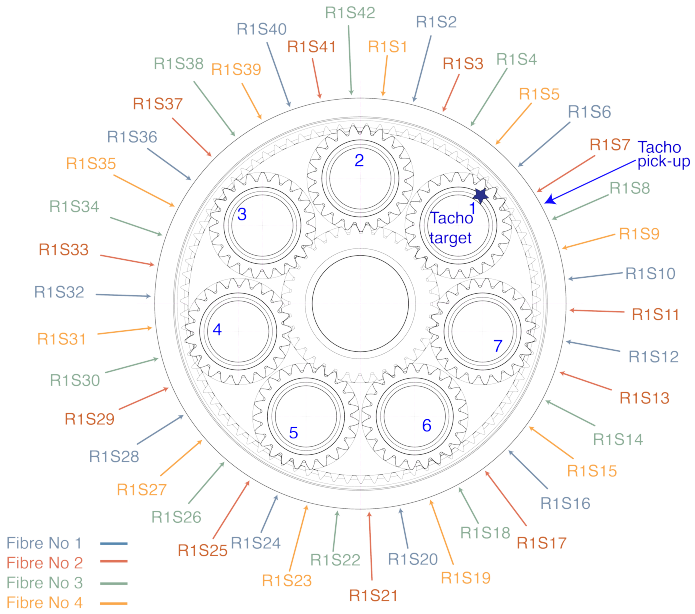

Figure 3.2: Sensor placement on the first-stage ring gear.

3.3.3 Test specification

The tests presented in this study were performed on an end-of-line test bench at the assembly factory of Gamesa Gearbox (Siemens Gamesa Renewable Energy) in Lerma, Spain. The standard IEC 61400-4 [59] sets the design requirements for wind turbine gearboxes and establishes a mandatory requirement to perform a loaded end-of-line test for all gearbox units before their installation in a wind turbine. This test is also referred to as the run-in or gearbox conditioning test. The purpose is twofold: on the one hand, it serves as a conditioning test for bearings and gears because the gearbox is loaded progressively up to nominal torque; on the other, it provides a means for quality control. Typically, gearbox manufacturers employ a back-to-back arrangement for end-of-line testing where two gearboxes are connected through the low-speed shaft (LSS). Figure 3.7 shows the layout of the back-to-back arrangement used for the experiments with the test gearbox, presented in Section 3.3.1, on the left side. An electric motor provides the driving motion to the high-speed shaft (HSS) of one gearbox, and the other motor acts as a generator, providing the braking torque at the HSS of the second gearbox. The rated power of the test bench electric motors is 11.5 MW, which enabled testing the gearbox above its nominal torque. Although the test bench is designed to recreate the working conditions of the gearbox as close as possible to the wind turbine, in back-to-back test benches, torque is the only controlled input load excitation, and they generally do not have the capacity to apply bending moments to the gearbox. The mechanical interfaces at the LSS and HSS of the gearbox are different from the wind turbine, and it is not possible to reproduce the rotor inertia in the test bench. Despite these differences, we consider the back-to-back test bench results

representative of the behavior of the gearbox in a wind turbine, in particular taking into account that these gearboxes are designed for operation in wind turbine drivetrains with a four-point mount suspension.

The instrumented gearbox completed a standard end-of-line test, composed of six stationary load stages under nominal speed. Once stable thermal conditions had been reached, signals from the fiber-optic strain sensors were logged at each of the run-in load stages to perform system identification. After the run-in, several design validation tests were performed, and these tests were used to collect more strain data to evaluate the state and output estimation procedures. In particular, a test to validate the structural models of the gearbox, comprised of 22 stationary torque conditions from 5 % to 110 % of its nominal value, was used to evaluate the effect of torque on the identified operational deflection shapes. Finally, different tests with dynamically changing torques were performed to quantify the contribution of the identified deflection shapes in a dynamic manner.

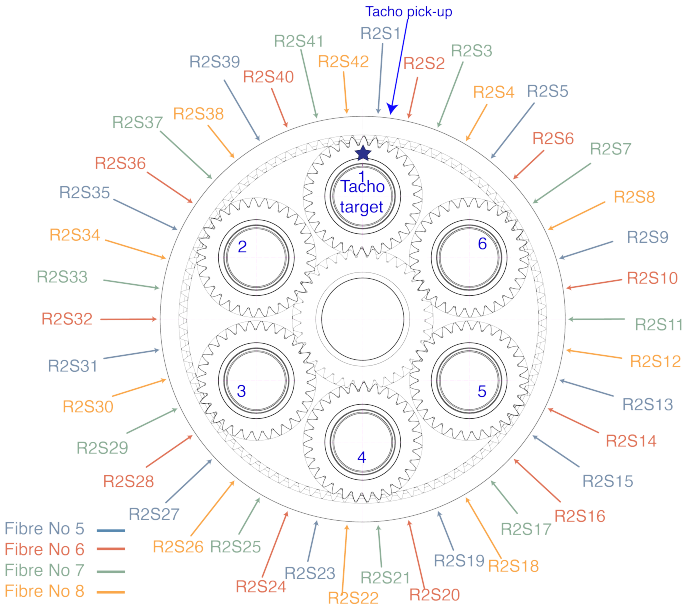

Figure 3.3: Sensor placement on the second-stage ring gear.

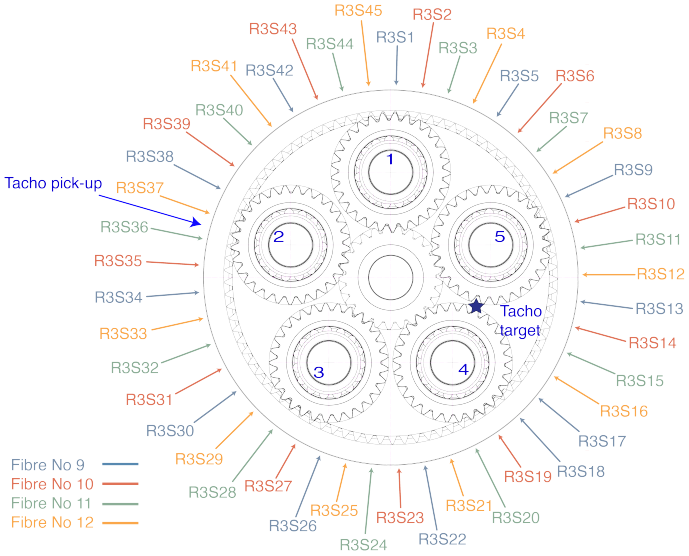

Figure 3.4: Sensor placement on the third-stage ring gear.

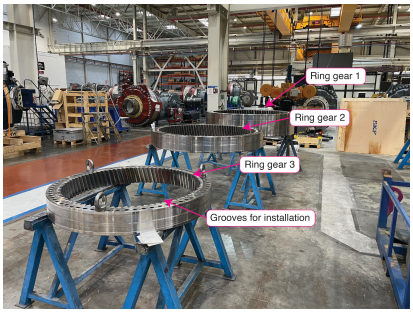

Figure 3.5: All three ring gears with machined grooves ready for sensor installation.

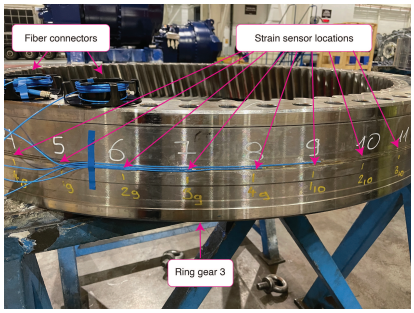

Figure 3.6: Details of fiber-optic sensors installed on the third-stage ring gear.

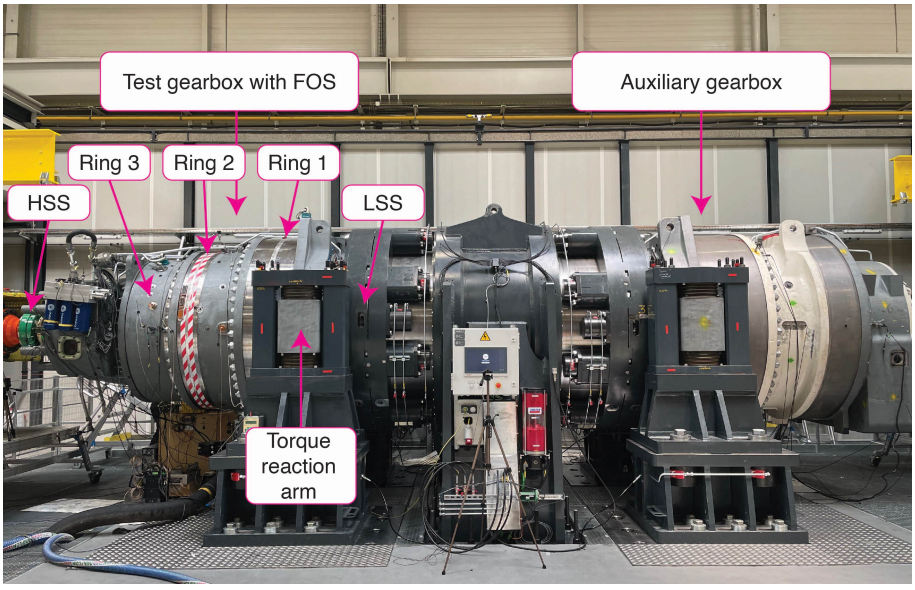

Figure 3.7: Test gearbox on the left side of the back-to-back test bench used for end-of-line testing of wind turbine gearboxes with a maximum power capacity of 11.5 MW.

3.4 Identification of operational deflection shapes

This section describes the key findings obtained when performing system identification on the strain signals logged during experiments performed on a serial production end-of-line test bench.

3.4.1 Identification using signals from all stages

The system identification framework presented in Section 3.2 was initially applied to all available signals from the three ring gears together. Figure 3.8 shows a time trace of two strain sensors from each stage during a test performed with rated stationary speed and torque conditions. As can be seen, each stage has a different rotational speed, and the time interval between strain peaks corresponds to the planet-passing frequencies defined in Table 3.2. Within each stage, the strain signals of two sensors are shown in Figure 3.8. The deformation peaks caused by the mesh forces as the planets pass close to the measurement points on the ring gears occur at different times because the sensors are at different angular positions. For clarity, only two sensors from each ring gear have been plotted in Figure 3.8 but there are 42 strain signals available in the first stage, 42 in the second stage and 45 in the third stage. The location of all sensors are shown in Figures 3.2, 3.3 and 3.4.

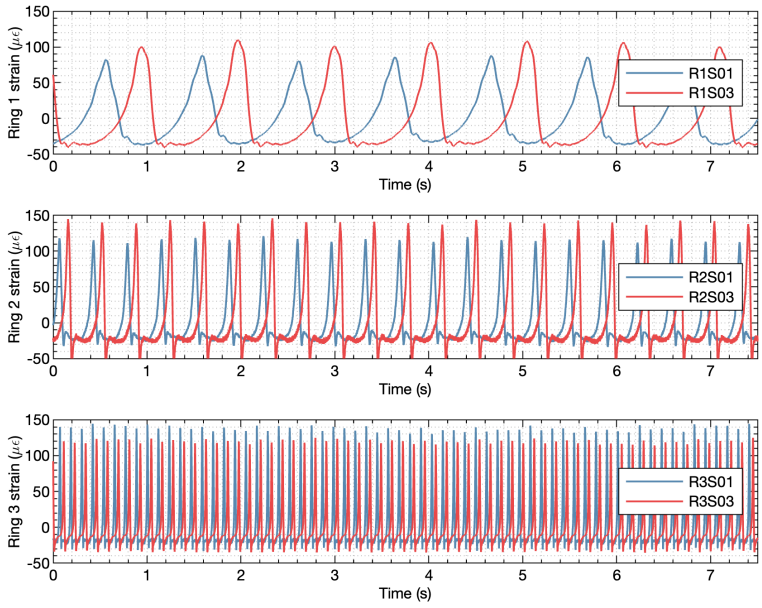

Figure 3.8: Raw strain signals logged from the first and third sensors of each planetary stage. The angular location of the R1S01, R1S03, R2S01, R2S03, R3S01, and R3S03 sensors is shown in Figures 3.2, 3.3 and 3.4.

Several data preprocessing steps were performed on the raw signals logged by the op-

tical interrogators. First, the sampling frequency was downsampled for a more efficient numerical implementation. Generally, the sampling rate should be up to about ten times the bandwidth of interest to avoid the effects of aliasing and, simultaneously, limit the amount of high-frequency noise that contaminates the measurements [94]. The optical interrogators used to acquire the signals during testing provided a sampling frequency of 2000 Hz in the first stage and 2500 Hz in the second and third stages. Considering the known excitation frequencies present during gearbox operation, see Table 3.2, different downsampled frequencies from 45 Hz to 250 Hz were tested. The difference between resampling, interpolation, and decimation on the identified parameters was found to be negligible. Therefore, resampling with an embedded anti-aliasing filter was chosen as the downsampling method. Measurements used for identification were logged once the gearbox had reached thermal stability. Thus, the influence of temperature variations on the FOS signals was minimized. Nevertheless, a detrending step was added to ensure that the signals fed to the identification algorithm only resulted from the strain caused by the planet gear passage events. All signals were normalized using their standard deviation to have unit variance. As a last preprocessing step, a hamming window was applied to the training data sequences because it was found to reduce the variance of the identified models.

As described in Section 3.2, from sequences of discrete-time data samples of the measured signals, three parameters need to be defined to execute the MOESP algorithm. These parameters are the number of samples, N; the number of block rows, s; and the system order, n. Using fiber-optic strain signals from the total of 129 sensors (42 from the first stage, 42 from the second, and 45 from the third), different options for N, s, and n were explored. The integer s should be chosen to be about 2-3 times the maximum expected model order [94]. The experiment duration, number of samples N, should usually be at least about 10 times the length of the slowest time constant of the system to ensure that the low-frequency behavior of the process is captured. Therefore, a trade-off between sample frequency and measurement duration must be made that is dictated by storage and/or processing limitations regarding the number of data points. After exploring different downsampled frequencies between 45 and 250 Hz, a frequency of 62.5 Hz was selected. This selection was based on identified frequencies and the signal reconstructions obtained using the one-step-ahead predictor, Eq. (3.13). Figure 3.9 shows the discrete-time representation of the pole locations of the identified models using $N = 17500$ samples per signal, $s = 64$ block rows and $n = 20$ a model order equivalent to 10 oscillatory modes. All identified poles are on the unit circle, which is expected from the periodic behavior. The corresponding frequencies associated with the identified poles are shown in Table 3.3. All identified frequencies match with known excitation frequencies. A description of the abbreviations used to name the frequencies can be found in Table 3.2. The term operational deflection shapes (ODSs) has been chosen for the observed part of the identified eigenvectors because they are caused by periodic excitations and not a structural property of the gearbox. These deflection shapes identified when using all strain signals together only influence one ring gear at a time. To illustrate this, the three mode shapes related to the planet-passing frequencies of each stage are shown in Figure 3.10. For example, in the case of the mode associated with the planet passing of the first stage, with an identified frequency of 0.9750 Hz, the deformations of this mode shape in the second and third

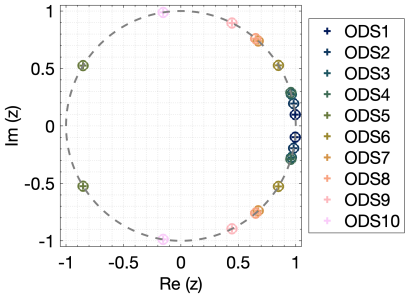

Figure 3.9: Pole locations (eigenvalues) of the identified model using measurement signals from all three stages in a discrete-time representation ($N = 17500$, $s = 64$, $n = 20$).

Table 3.3: Identified frequencies using signals from all three stages; a description of the abbreviations can be found in Table 3.2.

Mode	Frequency (Hz)	Order of LSS	Abbreviation
1	0.9748	7.0000	7xPC1
2	1.9496	13.9999	2x7xPC1
3	2.7618	19.8327	6xPC2
4	2.9244	21.0000	3x7xPC1
5	5.5234	39.6634	2x6xPC2
6	8.2861	59.5023	3x6xPC2
7	8.5844	61.6445	5xPC3
8	11.0466	79.3258	4x6xPC2
9	17.1688	123.2890	2x5xPC3
10	25.7532	184.9335	3x5xPC3

stages are negligible. This means there is very little cross-stage excitation, which is positive and one of the design objectives. Considering these results, it was decided to apply the identification algorithm on strain data from each stage individually.

3.4.2 Identification using signals from the first planetary stage

Using data from the same test, with rated torque and speed conditions shown in Figure 3.8, the system identification procedure was repeated with the strain signals from the first-stage ring gear only. The same preprocessing steps detailed in Section 3.4.1 were applied, and 10 different downsampled frequencies (45.45, 50.00, 55.55, 62.50, 71.43, 83.33, 100.00, 125.00, 166.67, and 250.00 Hz) were tested to explore the effect of resampling on the identified models using a baseline setting of $s = 32$ block rows and $n = 20$ model orders. The number of samples was chosen to cover the same training time, defined as 256 s, in all sampling frequencies. The different identified models were evaluated based on their identified frequencies (eigenvalues) and how well newly measured data from validation tests could be reconstructed using the identified operational deflection shapes. As in the case of all stages, the difference between identified frequencies using different sampling frequencies was found to be small. Again, all identified poles were on top of the unit circle, corresponding to undamped modes. To evaluate the accuracy of the reconstructed outputs, data for validation were acquired using the same experimental conditions as for training the models: applying stationary rated torque and speed and waiting for temperatures across the gearbox to stabilize. With the identified system matrices, the system's state and output signals can be reconstructed using Eq. (3.12). The Kalman filter was not considered for model validation because the intention is to evaluate how the identified system matrices

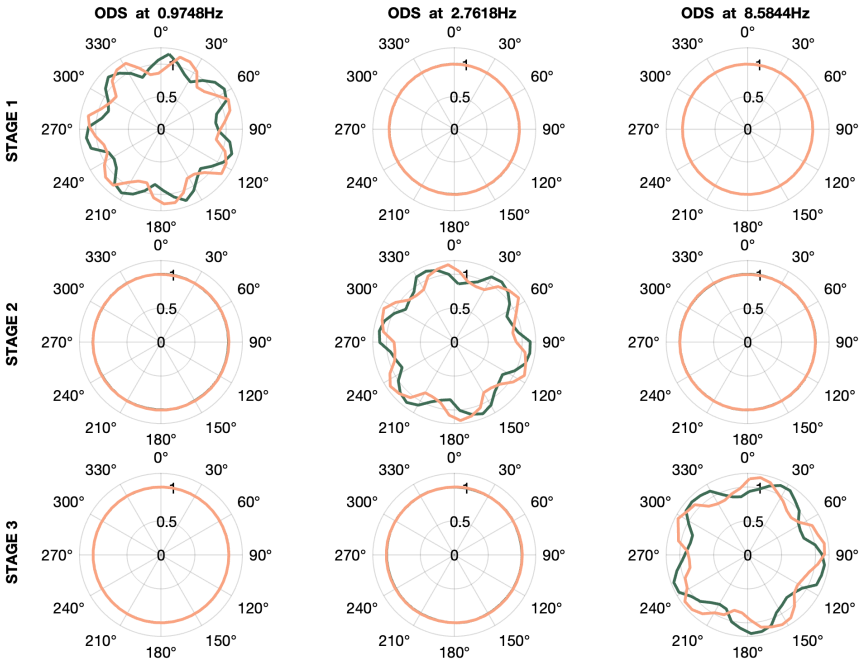

Figure 3.10: Identified operation deflection shapes using measurement signals from all three stages. Each shape is defined by two conjugate vectors with a size equal to the number of sensors; the real part is shown in green, and the imaginary part is shown in orange.

represent the measured signals. In this case, the system's behavior is modeled as an autonomous system oscillating from a non-zero initial condition which can be derived from Eq. (3.13). As the identified damping coefficients are close to zero, the modules of the state show little variation throughout the duration of the validation datasets. Figure 3.12 shows a comparison of the measured signal from sensor R1S01 (first sensor of first-stage ring gear) against the reconstructed output using identified models with three different sampling frequencies. Very high variance accounted for (VAF) values were obtained with the reconstructed outputs. The highest average VAF was 99.68 % obtained for a sampling frequency of 62.5 Hz, and the lowest value was 98.40 % for the case of 250 Hz. For this reason, 62.5 Hz was used as a sampling frequency to search for suitable s and n parameters. Table 3.4 shows the average VAFs obtained for different combinations of s block rows and n model orders. The VAF value presented is the average of the 42 sensors. Increasing the model order and the number of block rows improved the fit between the reconstructed and measured signals; an average VAF value of 99.00 % was already achieved with $s = 32$ and $n = 10$. This VAF could be increased up to 99.90 % when further increasing s and n to $s = 128$ and $n = 32$. As with other practical applications of system identification [89], we did not observe a big gap in VAFs from one model order to the next. Table 3.5 shows the

frequencies of the 10 deflection shapes identified using $s = 128$ and $n = 20$. Up to $n = 18$, all the deflection shapes correspond to multiples of the planet-passing frequency (7 times the carrier rotational frequency), and for larger model orders, the planet carrier rotational frequency is also identified. Figure 3.11 shows the deflection shapes associated with the planet-passing frequency and the first two integer multiples or harmonics. Due to the given spatial resolution (42 sensors around the ring gear), it is not possible to represent higher-frequency mode shapes accurately as they provoke a spatial aliasing effect. This, however, does not affect the output reconstruction of individual sensors as long as the sampling frequency is high enough for the identified modes.

Table 3.4: VAF of first-stage strain measurements and reconstructions with a sampling frequency of 62.5 Hz and 16000 samples.

VAF (%)	$n = 2$	$n = 6$	$n = 10$	$n = 14$	$n = 18$	$n = 20$	$n = 24$	$n = 32$
$s = 8$	3.04	26.67	-	-	-	-	-	-
$s = 16$	60.02	69.66	98.83	98.99	-	-	-	-
$s = 32$	72.42	97.49	99.00	99.39	99.34	99.69	99.71	-
$s = 48$	72.40	89.02	99.08	99.32	99.44	99.64	99.65	99.73
$s = 64$	72.55	97.50	99.33	99.44	99.62	99.69	99.73	99.75
$s = 96$	72.55	97.50	99.33	99.45	99.53	99.71	99.76	99.77
$s = 128$	72.55	97.50	99.34	99.43	99.59	99.78	99.83	99.90

Table 3.5: Identified frequencies from the first-stage measurement signals using $s = 128$ and $n = 20$ (10 modes).

	Frequency (Hz)	**Order of LSS**	**Description**	**State module**
1	0.1407	1.0108	PC1	81.52
2	0.9748	7.0000	7xPC1	2181.44
3	1.9496	14.0000	2x7xPC1	1117.53
4	2.9244	20.9999	3x7xPC1	624.14
5	3.8992	27.9999	4x7xPC1	313.85
6	4.8739	34.9993	5x7xPC1	149.58
7	5.8487	41.9997	6x7xPC1	89.13
8	6.8233	48.9984	7x7xPC1	73.23
9	7.7983	55.9998	8x7xPC1	75.66
10	8.7731	62.9998	9x7xPC1	74.51

The reconstructed output signals shown in Figure 3.12 were computed using the system matrices only, finding the initial state conditions and assuming the system behaves like an autonomous system. We can improve the state estimation using Eq. (3.13) with the Kalman filter. This allows for the analysis of strain measurements from tests with variable torque. The states associated with each mode shape convey the contribution of each mode to the measured strain signals. For the validation test performed using stationary

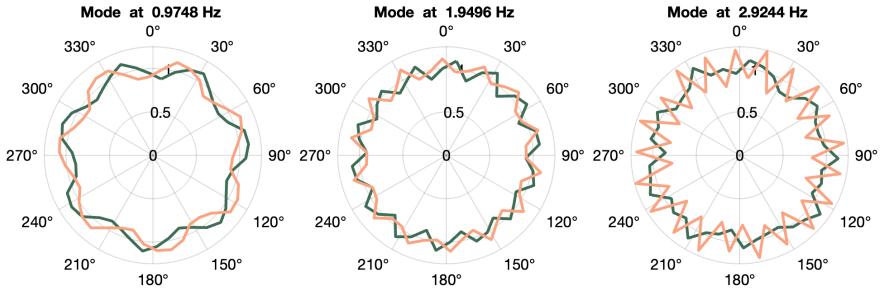

Figure 3.11: Deflection shapes from the first three harmonics of the planet-passing frequency using measurement signals from the first stage. Each shape is defined by two conjugate vectors; the real part is shown in green, and the imaginary part is shown in orange.

rated torque and speed, the average modulus values of the states associated with the operational deflection shapes are shown in Table 3.5. The system matrix was transformed into diagonal form, with the eigenvalues in the diagonal. As described in Section 3.2, these eigenvalues are complex numbers and for oscillatory systems they come in conjugate pairs. Therefore, two states, which are also conjugate imaginary numbers, are associated with a pair of eigenvalues. From these values, we can infer that the contribution of the first deflection shape, which is related to the rotation of the planet carrier, is relatively small. The second deflection shape, created by the passing of the planets at 7 times planet carrier frequency, is the most dominant mode shape, and its higher harmonics have a descending contribution.

3.4.3 Effect of torque on identified models and state variables

Once a model has been identified using suitable training data, that is, the operational deflection shapes and their frequencies have been found, the associated states can be computed using the one-step-ahead predictor, Eq. (3.12). When the state variables are computed for tests with stationary torque conditions, the modulus of the state remains almost constant and only exhibits small changes. These small changes are also evident in the test bench torque signals and in the peak values of the fiber-optic strain signals; see Figure 3.8. In Figure 3.13, a depiction of the strains reconstructed using only the first three operational deflection shapes associated with the passing of the planets is shown. To evaluate the effect of torque on the identified deflection shapes, a test comprised of 22 stationary torque conditions from 5 % to 110 % of its nominal value was performed. This test was originally intended to validate the structural models of the gearbox. Once stability in torque and speed was reached, data were recorded for 240 s for each torque condition. Torque

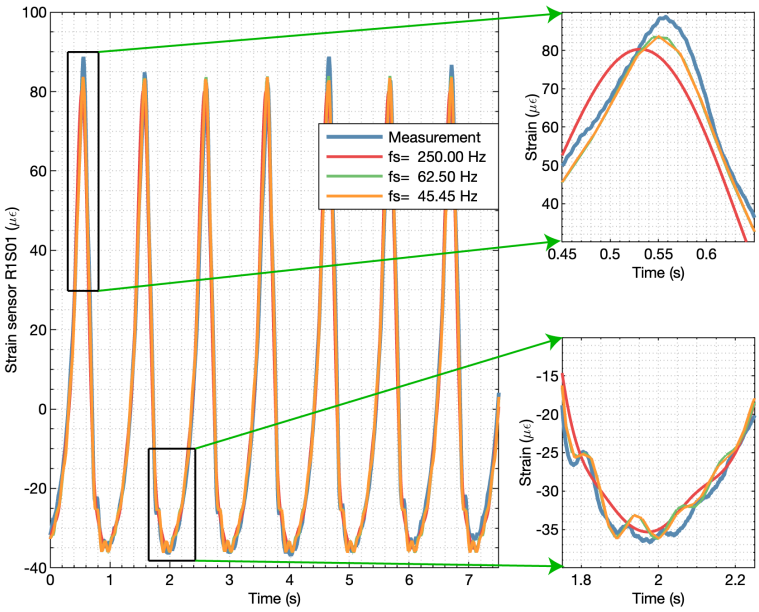

Figure 3.12: Output reconstruction of strain signal R1S01 using models identified with different sampling frequencies.

data from two test bench torque sensors installed in the high-speed shafts (HSSs) were logged synchronously with the fiber-optic strain data. From these two sensors, the torque at the low-speed shaft (LSS) was estimated as the average value of both high-speed shafts multiplied by the gear ratio. This assumes that the gear losses are equal in both gearboxes, which is not exactly true because the two gearboxes tested were not identical, and the torque level in the gearbox acting as a reducer is slightly higher, but it is considered a good approximation to evaluate the effect of torque.

The 22 data recordings at different torques were used to identify operational deflection shapes. Figure 3.14 shows the deflection shapes of the mode corresponding to the planet-passing frequency of the first stage (7 times the rotational frequency of the carrier) from 55 % to 100 % of the nominal torque. When the system matrix is transformed into a diagonal form, as described in Section 3.2, each mode $\{\phi_i\}$ comes in conjugate pairs of imaginary numbers. For clarity, only the real component of the mode shape is shown in a linear format, and the magnitudes have been normalized using the norm of the deflection shape at nominal torque. The shapes are very similar, with only very slight differences observed when the torque drops below 65 % of nominal torque. The gearbox is designed to operate in near-rated torque conditions where the gear microgeometry has been optimized.

This observation led to evaluating the relationship between the contribution of mode

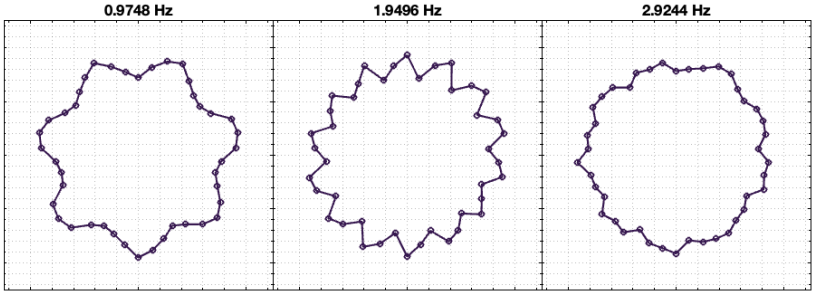

Figure 3.13: Simulated strains on the first-stage ring gear associated with the first three planet-passing modes. The axis labels and units have been omitted as the deformations were scaled for better representation. An animation of a planet carrier revolution is available in a supplementary video file [99].

shapes identified at nominal torque conditions for the 22 load stages. Using the identified ODSs at nominal torque, the corresponding states were computed for the data recordings at different torques. When using the diagonal form, the state variables are also conjugate imaginary numbers. The moduli or absolute values of the state variables for each test against torque are shown Figure 3.15. The modulus or absolute value of the states associated with the first deflection shape doesn't exhibit any relationship with torque. However, all the states associated with the planet-passing frequency and its harmonics show a very strong relationship with torque. A polynomial fit was computed between the module of the state and torque, which can be used to estimate torque from a known state value. To demonstrate this we performed a test with six torque levels. In Figure 3.16, the torque estimation from the test bench torque sensors is compared to the torque estimation using the state variable associated with the planet passing of the first stage. As can be seen, the torque estimate using the planet-passing mode closely follows the behavior of the torque estimate from the test bench torque sensors with a similar pattern. As mentioned before, the torque sensors are placed in the HSS of both gearboxes in the back-to-back arrangement, and a comparison with a direct measurement in the input LSS is suggested to further evaluate the accuracy of the new estimation method.

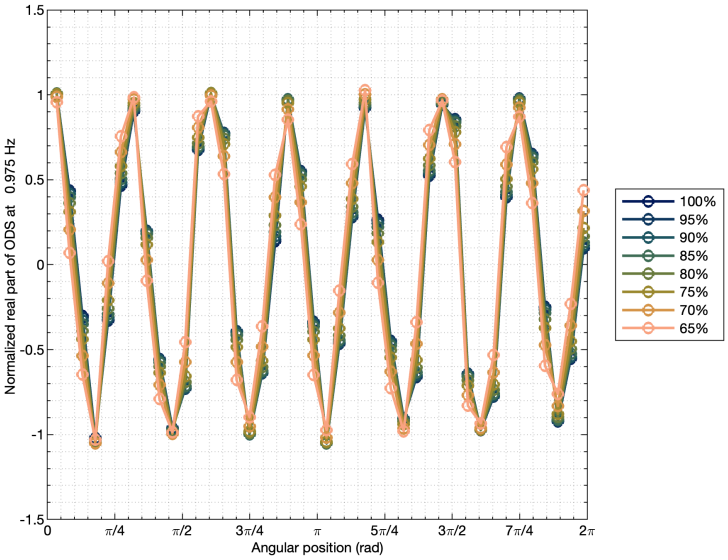

Figure 3.14: Operational deflection shapes (real part) using datasets at different torque levels for identification.

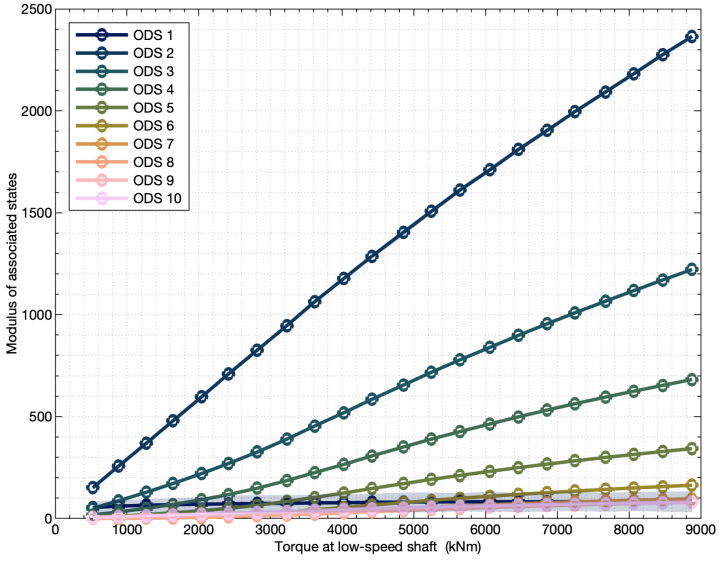

Figure 3.15: Average moduli of states associated with each ODS against the low-speed shaft torque (from test bench sensors).

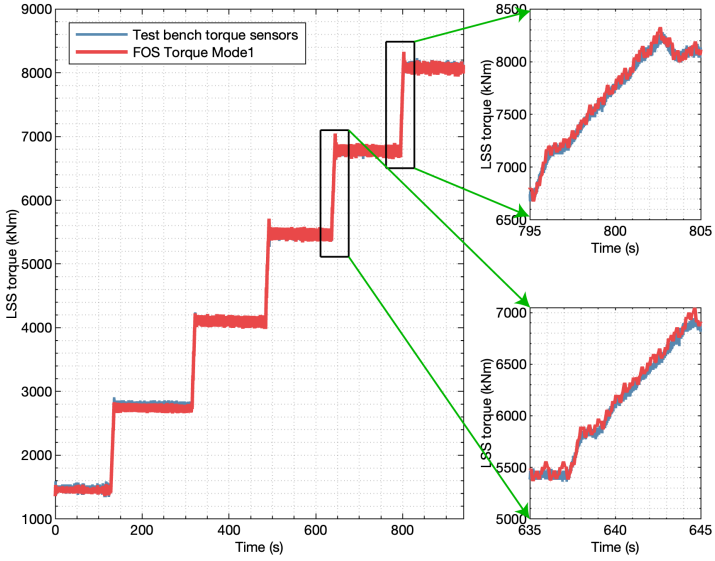

Figure 3.16: Torque estimation from identified ODS vs test bench torque sensors for a test with dynamic torque conditions.

3.5 Conclusions

This article presents a novel measurement setup of 129 fiber-optic strain sensors distributed around the three ring gears of a modern wind turbine gearbox. The subspace identification multivariable output-error state space (MOESP) method has been applied to experiments performed on a serial production end-of-line test bench and has been found to provide consistent estimates. Using signals from tests with stationary torque and speed conditions, all identified eigenvalues and eigenvectors correspond to periodic excitations related to shaft rotations, planet passing, and gear mesh frequencies. When performing system identification on data from all three stages, the identified deflection shapes have been found to cover only one stage at a time. Therefore, no cross-excitation between stages was observed, which is in line with one of the design intents to minimize cross-stage interactions. Therefore, it can be concluded that the identification algorithm can be applied to strain data from each stage individually.

For each planetary stage, the effect of the different identification parameters that can be chosen in the MOESP algorithm has been explored. Measurements from model validation tests, with the same torque and speed conditions as the ones used for identification or training, have been used to evaluate the identified frequencies and mode shapes. The variance accounted for (VAF) between the validation measurements and the reconstructed outputs, simulating the system's behavior as an autonomous system oscillating from a non-zero initial condition, has been used as a metric. For the signals of the first-stage ring gear, average VAF values above 99 % were achieved between the signals measured in the validation tests and the reconstructed signals for suitable combinations of s block rows and n model orders. Therefore, the identified deflection shapes can reproduce the behavior of the gearbox accurately, and the contribution of the periodic excitations accounts for almost all the energy in the measured strain signals. The effect of torque on the identified deflection shapes has been studied, and no noticeable differences in the planet-passing mode shapes were observed for torques above 65 % of the nominal value. For strain recordings from tests with dynamically changing torque conditions, the contribution of the periodic modes has been quantified through the states associated with the operational deflection shapes identified at nominal torque. The contribution of the deflection shapes produced by the passing of planets is controlled by the amount of input torque applied to the gearbox. Using this contribution an estimate of the input torque has been demonstrated for dynamic operating conditions.

Accurate knowledge of the input torque is critical for ensuring the reliability of wind turbine gearboxes. Measuring the input torque throughout the service history of every gearbox in a fleet would enable an improved assessment of the consumed fatigue life. This is important because the loading conditions are site-specific, and allowing for an individual evaluation of each gearbox can lead to a better understanding of current gearbox failure modes. The system identification framework presented in this article can be applied recursively to track the operational deflection shapes over time. This is proposed for fault detection in the planetary stage components. Three avenues are suggested for future work. First, it is recommended that the accuracy of the torque estimate produced by the strain measurements on the outer surface of the ring gear be quantified against a conventional direct measurement in the input shaft. When assessing the accuracy, the effects of non-torque loads, i.e., axial forces and bending moments, should be explored. Second,

we suggest researching different sensor configurations and loading conditions that can excite the structural modes. Finally, it is suggested that the fault detection capabilities of trending the operational deflection shapes be investigated, ideally by seeding known faults in components of the planetary stages and evaluating their impact on the identified mode shapes.

3.6 Annex: Identification using signals from the second and third planetary stages

The same identification exercise presented in Section 3.4.2 was performed for the strain signals acquired for the second and third stages. Using the same approach as for the first stage, a suitable sampling frequency was selected first, and then the effects of the identification parameters s,n and N, were explored. For the second stage, a sampling frequency of 208.33 Hz was found to give satisfactory identification results. Table 3.6 shows the frequencies associated with the deflection shapes using $s = 128$ and $n = 20$. In this case, all identified frequencies correspond to the planet-passing frequency, 6 times the carrier rotational frequency, and its harmonics. The first three identified mode shapes of the second stage are shown in Figure 3.17, and a depiction of the reconstructed strain signals using these deflection shapes is shown in Figure 3.18. In this case, due to the higher frequency and frames per second, of the animation had to be reduced and could not match the identified frequencies. For the third stage, a sampling frequency of 625 Hz was chosen, and the identified frequencies are shown in Table 3.7. In this case, using $s = 128$ and $n = 20$, the first nine identified frequencies correspond to the planet-passing harmonics (third stage has five planets). The last identified frequency corresponds to twice the gear mesh frequency of the second stage. The second-stage ring gear drives thethird-stage planet carrier. However, the contribution of this mode is very small. The first three identified mode shapes of the third stage are shown in Figure 3.19, and an animation of the strains reconstructed using these deflection shapes is shown in Figure 3.20. Again, the allowable frames per second could not match the identified frequencies, and the speed of the animation had to be reduced.

Table 3.6: Identified frequencies using measurement signals from the second stage with $s = 128$ and $n = 20$ (10 modes).

	Frequency (Hz)	Order of LSS	Description
1	2.7619	19.8330	6xPC2
2	5.5238	39.6661	2x6xPC2
3	8.2856	59.4992	3x6xPC2
4	11.0475	79.3322	4x6xPC2
5	13.8094	99.1653	5x6xPC2
6	16.5712	118.9983	6x6xPC2
7	19.3331	138.8314	7x6xPC2
8	22.0950	158.6643	8x6xPC2
9	24.8581	178.5060	9x6xPC2
10	27.6304	198.4140	10x6xPC2

Table 3.7: Identified frequencies using measurement signals from the third stage with $s = 128$ and $n = 20$ (10 modes).

	Frequency (Hz)	Order of LSS	Description
1	8.5844	61.6445	5xPC3
2	17.1688	123.2892	2x5xPC3
3	25.7531	184.9337	3x5xPC3
4	34.3375	246.5780	4x5xPC3
5	42.9218	308.2222	5x5xPC3
6	51.5062	369.8665	6x5xPC3
7	60.0901	431.5077	7x5xPC3
8	68.6750	493.1560	8x5xPC3
9	77.2774	554.9303	9x5xPC3
10	91.8262	659.4054	2xGMF2

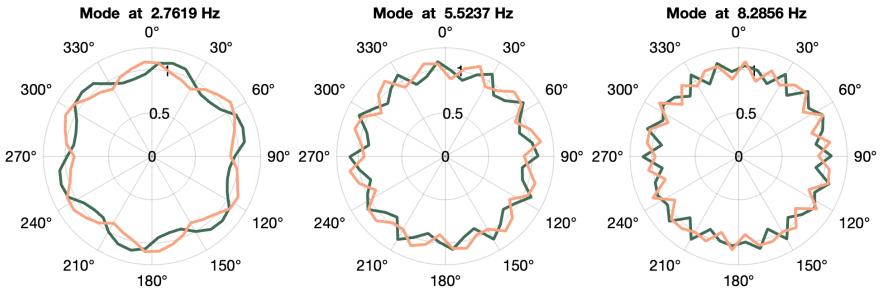

Figure 3.17: Deflection shapes from the first three harmonics of the planet-passing frequency using measurement signals from the second stage. Each shape is defined by two conjugate vectors; the real part is shown in green, and the imaginary part is shown in orange.

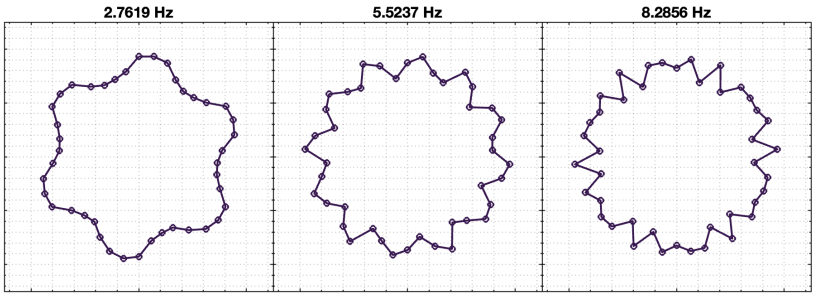

Figure 3.18: Simulated strains on the second-stage ring gear associated with the first three planet-passing modes. The axis labels and units have been omitted as the deformations were scaled for better representation. An animation of a planet carrier revolution is available in a supplementary video file [99].

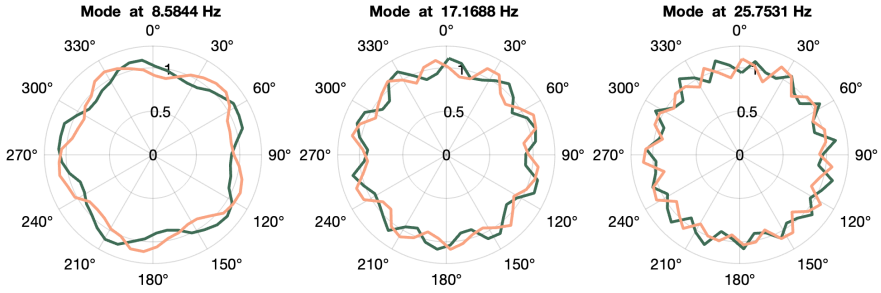

Figure 3.19: Deflection shapes from the first three harmonics of the planet-passing frequency using measurement signals from the third stage. Each shape is defined by two conjugate vectors; the real part is shown in green, and the imaginary part is shown in orange.

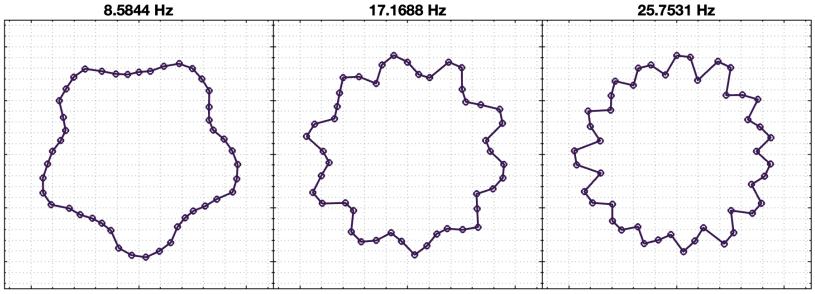

Figure 3.20: Simulated strains on the third-stage ring gear associated with the first three planet-passing modes. The axis labels and units have been omitted as the deformations were scaled for better representation. An animation of a planet carrier revolution is available in a supplementary video file [99].

4

Field validation of dynamic mechanical torque measurements using fiber-optic strain sensors for geared wind turbines

Accurate knowledge of the mechanical loads of wind turbine gearboxes has become essential in modern, highly loaded gearbox designs, as maintaining or even improving gearbox reliability with increasing torque density demands is proving to be challenging. Unfortunately, the traditional method of measuring dynamic mechanical torque using strain gauges placed on the outer surface of a rotating shaft and transmitting the resulting signal is unsuitable for serial deployment due to technical and economic constraints. An alternative method based on fiber-optic strain sensors placed on the stationary outer surface of the gearbox ring gear has been proposed. Like shaft torsion, the radial deformation of the ring gear is proportionate to the rotor torque. Placing the sensors on a stationary component is a cost-effective alternative for serial implementation because the need for complex and expensive data transfer via wireless transmission or a slip ring is eliminated. We present the results of an extensive field experiment conducted to evaluate the torque measurement accuracy of this novel sensing solution installed on the gearbox of a Gamesa G97 2-MW wind turbine at the National Renewable Energy Laboratory's Flatirons Campus. Torque measurements derived from fiber-optic strain sensors placed on the ring gear of the planetary stage are compared to conventional torque measurements from strain gauges placed on the main shaft. Two different torque estimation data processing methods were evaluated, each of which provide an average normalized root-mean-square error below 0.7 % for a load revolution distribution analysis and are insensitive to nontorque load and temperature effects. The method based on the third planet-passing operational deflection shape has several advantages over the peak-to-peak method, such as a higher sampling frequency and potential for real-time application. The fiber-optic strain sensors' successful operation during the complete test campaign has demonstrated a robust and accurate solution for fleet-wide enhanced gearbox remaining useful life estimation.

4

This chapter is based on the following publication: *U. Gutierrez Santiago. Field validation of dynamic mechanical torque measurements using fiber-optic strain sensors for geared wind turbines* [100]. Green is the fourth color of the rainbow when arranged by increasing wavelength. Green has a wavelength between 495 nm and 570 nm. The CMYK color model, also known as process color or four color, is a subtractive color model used in color printing. It is based on the CMY color model and uses four ink plates: cyan, magenta, yellow, and key (black). The CMYK model works by masking colors on a lighter background, usually white, and is called subtractive because the inks subtract some colors from white light. In contrast, the RGB color model is an additive color model where red, green, and blue lights are combined to create colors. The CMYK model is used for printing, while the RGB model is used for electronic displays. The RGB color model is used for sensing, representing, and displaying images in electronic systems like televisions and computers. The choice of primary colors in the RGB model is related to the human eye's physiology, maximizing the difference between the responses of cone cells to different wavelengths of light. The green color used for this chapter has a CMYK value of (0.53, 0, 0.51, 42) which is equivalent to (70, 147, 72) in RGB.

4.1 Introduction

Wind turbine power ratings, rotor diameters, and hub heights have grown significantly to reduce the cost of wind energy [9]. The wind turbine drivetrain converts mechanical power to electrical power and transmits the rotor loads to the bedplate and tower [12]; it makes an appreciable contribution to the capital expenditure of the turbine [13]. Many wind turbine drivetrains use gearboxes to lower the capital cost of the drivetrain, but its reliability is essential and remains a top priority because gearbox failures cause long downtime with costly repairs and contribute appreciably to the turbine operation and maintenance costs [10, 23, 24]. Thanks to internationally recognized gearbox wind turbine design standards like IEC 61400-4 and AGMA 6006 and collaborative efforts like the Drivetrain Reliability Collaborative between turbine manufacturers, gearbox designers, bearing suppliers, and research institutions like the National Renewable Energy Laboratory (NREL) and Argonne National Laboratory, average annual gearbox failure rates for the U.S. land-based fleet have dropped from 5 % to 10 % 20 years ago [25] to 2.5 % more recently [26]. Yet, there is room for improvement because gearboxes still generally do not reach their desired design life [27]. These standards have placed greater rigor on the design and gearbox verification process, including the effects of rotor non-torque loads [28], transient events [29, 30], and electrical currents [31]. However, the rapid pace at which torque density requirements have risen has led to increasingly complex and lightweight designs with new reliability challenges and additional requirements, such as complying with stricter noise demands and more prominent dynamic interactions.

Accurate knowledge of the dynamic mechanical torque in wind turbine gearboxes is essential to complying with these requirements and improving their reliability. Dynamic mechanical torque measurements of every gearbox in a fleet can enhance drivetrain usage monitoring because the consumed fatigue life can be assessed more precisely using the measured torque values throughout their entire commercial operation. Dynamic torque measurements can also potentially be used by the wind turbine controller for improved wind turbine control to achieve a reduction of torque oscillations (i.e., torsional damping). Additionally, dynamic mechanical torque measurements can be used to quantify drivetrain efficiency. Unfortunately, sensors that provide detailed load measurements of the turbine during commercial operation are not generally available [41]. It is possible to estimate the mechanical gearbox torque from the electric currents in the generator, but this requires assumptions about the variable gearbox, generator, and power converter efficiencies for fatigue life calculations and is not available for estimation of the severity of high-load, damaging events like emergency braking and low-voltage ride through when the generator disconnects from the grid [30, 42–44]. The conventional method to measure dynamic mechanical torque is based on bonding strain gauges to a rotating drive shaft. The strain gauges convert the torsional deformation caused by the torque into a change in electrical resistance. Transferring the resulting signal from the rotating shaft to a stationary data logging system and powering the data acquisition devices is difficult and costly. In wind turbines, the main shaft's torsional deformation is also small because of its high stiffness, which typically results in a low signal-to-noise ratio. The torsional deformation of the gearbox output shaft is higher, but accessing this shaft can require special provisions [30]. These drawbacks have limited the use of such measurements to laboratory environments [28], validation and certification of experimental wind turbines [45], and troubleshooting

exercises [46]. Other researchers have focused on indirect techniques or so-called virtual sensors where a model of the system is combined with data from sensors in other locations of the turbine to obtain an estimate of dynamic mechanical torque [47–53].

Installation of fiber-optic sensors (FOSs) in other wind turbine components, such as blades [64], has recently become more common. FOSs offer several advantages compared to traditional electrically resistive strain gauges, including higher signal-to-noise ratio, immunity to electromagnetic interference, and the ability to accommodate many strain sensors in a single fiber [63]. Previous work demonstrated an alternative method to measure the dynamic mechanical torque based on deformation measurements of the static first-stage ring gear using fiber-optic strain sensors during a bench test of a 6 MW wind turbine gearbox with 5 planets [86]. By measuring strain on the static or fixed frame, the difficulties related to data transfer from a rotating shaft and the power supply of the electronic components on the shaft are avoided. However, this work was conducted on a back-to-back gearbox test bench intended for validation and certification of new gearbox designs and for end-of-line testing of serial production units. Such test benches typically have limited capabilities for producing dynamic torque and generally cannot create controlled nontorque loads, such as axial loads and bending moments created by the rotor. Field testing provides the most realistic platform for performance evaluation of this fiber-optic-based torque measurement method, as certain problems related to the interaction of multiple drivetrain components can only be discovered after deployment in the field [101].

In the work described in this chapter, we took the next step in technology development and validation of dynamic mechanical torque measurements using fiber-optic strain sensors by:

- Conducting an extensive field validation campaign to demonstrate the use of FOSs for wind turbine gearbox dynamic mechanical torque measurements, contributing to an increase in the technology readiness level from 6 to 7 as defined in ISO 16290.
- Assessing the accuracy of dynamic mechanical torque measurements by comparing the results gathered from fiber-optic strain sensors to reference torque measurements from conventional strain gauges installed on the main shaft over a wide range of normal power production conditions.
- Investigating the effects of wind turbine operating conditions on the quality of dynamic mechanical torque measurements, with a special focus on the effects produced by nontorque loads and ring gear temperature.

The remainder of the chapter is structured as follows. In Section 4.2, we describe the measurement setup and test program. In Section 4.3, two alternative data processing procedures are described to derive gearbox torque from fiber-optic strain signals. In Section 4.4, the key findings from the validation campaign are described, and finally, Section 4.5 summarizes the main conclusions of this work.

4.2 Experimental setup

The present study was conducted on a Gamesa G97 2 MW wind turbine located at the NREL Flatirons Campus (Colorado, USA) as shown in Figure 4.1a. The G97 turbine has a

four-point mount drivetrain, in which two spherical roller bearings 1.3 m apart support the main shaft and transfer all rotor nontorque loads to the main frame. The main shaft then transmits nearly only torque to the gearbox planet carrier. The gearbox planetary stage includes three equally spaced planets meshing with the ring gear and a floating sun pinion, while two additional parallel stages use helical gearing. The gearbox provides a total gear ratio of 126.328, which at a rated rotor speed of 15.96 rpm results in a speed of 2,016 rpm of the doubly-fed induction generator. The gearbox mass is 14,620 kg, resulting in a torque density of 90 Nm/kg at a reference (rated) mechanical torque of 1,320 kNm. This torque density was quite common at the time of development of the G97, but modern gearboxes are now being produced with torque densities over 200 Nm/kg [12, 86]. During the test campaign, data were collected from three different sources [102]:

1. FOSs installed on the outer surface of the gearbox ring gear to measure ring gear deformation

2. Meteorological and drivetrain sensors to measure rotor inflow conditions and main-shaft loads

3. Wind turbine operational parameters collected from the turbine controller.

An overview of the drivetrain arrangement with the location of the gearbox ring gear FOSs and the main-shaft strain gauges are also shown in Figure 4.1b.

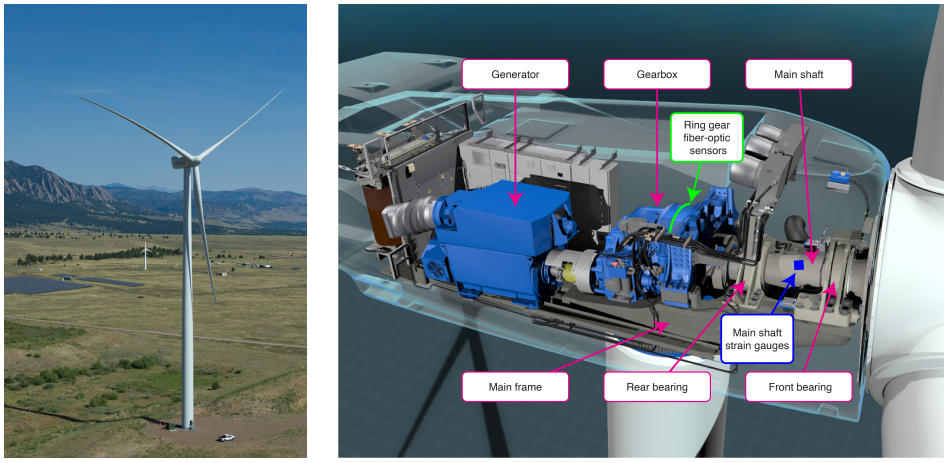

(a) **(b)**

Figure 4.1: **(a)** G97 2 MW wind turbine on NREL's Flatirons Campus; photo from Dennis Schroeder, NREL 21886. **(b)** Nacelle schematic (source Nextwave Multimedia (`https://www.nextwavemultimedia.com/blog/3d-animation/this-time-a-stereoscopic-3d-av-for-gamesa-by-nextwave/`).

4.2.1 Ring gear fiber-optic sensors

Two fibers with a total of 23 FOSs were installed around the outer surface of the ring gear of the gearbox at the midpoint of the ring gear face width. Figure 4.2a shows the planetary stage of a G97 gearbox as seen from the rotor side. The sensors were located at the midpoint of the ring gear width, b, and evenly distributed around the ring gear circumference as shown in Figure 4.2b. In operation, the mesh force between the planets and ring gear, F_p, causes deformation of the ring gear proportionate to the rotor torque as the planets orbit around the ring gear. Because the ring gear rim thickness, S_r, is relatively thin, significant deformations can be measured by FOSs well within their sensing capabilities [86]. The FOSs used for the present study are based on fiber Bragg gratings (FBGs) and are commonly classified as discrete sensors. FBGs are modifications to the fiber's core in discrete, short segments that reflect particular wavelengths of light and transmit all others. FBGs are used extensively for sensing applications because the reflected wavelength is sensitive to temperature and strain changes at the grating. They offer several advantages compared to electrical strain gauges [63]. FBGs offer a higher signal-to-noise ratio than strain gauges and are immune to electromagnetic interference. A single optical fiber can also accommodate multiple sensors, simplifying the installation process. For torque measurement, a total of 23 FBGs was chosen because it is a noninteger multiple of the three planets, in contrast with the 24 FBGs that were intentionally chosen as an integer multiple of the three planets for previous planet load-sharing measurements [102]. The FBGs for torque measurement were accommodated in two optical fibers, with 11 and 12 FBGs. In Figure 4.2b, the sensors have been color-coded depending on the optical fiber to which they belong. The fibers were bonded with cyanoacrylate glue to the outer surface of the ring gear in an existing machined groove. A snapshot of the uptower installation process is shown in Figure 4.3a. Because the sensors were retrofitted to an operational wind turbine, the protective paint on the ring gear had to be removed by sanding to allow for better bonding between the fibers and the ring. In operation, an interrogator sends light into the fibers and analyzes the wavelengths reflected by the gratings. The interrogator extracts a signal proportional to the spectral shift in each FBG caused by mechanical and thermal strain. The interrogator used for the measurement campaign provided a sampling frequency of 2,000 Hz for each signal. Sensing360 B.V. supplied the FOSs and the interrogator.

4.2.2 Meteorological and drivetrain sensors

A second set of sensors were installed on a meteorological tower in front of the wind turbine and the drivetrain to gather related operational data for comparison to and analysis of the fiber-optic measurements. The inflow wind conditions were gathered from the NREL M4/site 4.4 meteorological tower located near the wind turbine. Wind speed, wind direction, and temperature measurements at hub height were recorded. For the drivetrain, three full Wheatstone bridges consisting of weldable strain gauges were placed on the outer surface of the tapered main shaft at a diameter of 553 mm and approximately halfway between the two main bearings, 2.29 m from the rotor center of gravity and 0.62 m from the front main bearing as shown in Figure 4.3b. LEA-06-W125F-350/3R strain gauges were used to measure the main-shaft torque and LEA-06-W250B-350 strain gauges were used to measure the two orthogonal main-shaft bending moments. A battery-powered

V-Link transmitter system was used to transmit the bridge outputs to a base station where they were recorded in units of volts. A CEV58M-1600 absolute rotary shaft encoder was installed to measure absolute azimuth angle to relate both the fiber-optic strains measured on the static ring gear described in the previous section and the main-shaft strains to the angular position of the main shaft and rotor. A zero-degree azimuth angle was set referenced to the blade labeled as "A" when pointing down. Additionally, an SA1 resistance temperature detector was installed on the outer surface of the bottom of the ring gear to measure its temperature and assess the effect of thermally induced strains in the FBGs on the accuracy of the torque measurements. These data were recorded by an NREL-operated, GPS-time-synchronized, National Instruments-based EtherCAT data acquisition system at a sampling rate of 60 Hz for 10-minute periods.

4.2.3 Turbine operation parameters

The last data source was the turbine controller. Using a proprietary data acquisition system supplied by Siemens Gamesa, several operational parameters were recorded with a sampling frequency of 25 Hz. These operational parameters included the wind speed measured by the turbine, nacelle direction, total power produced, generator and rotor speed, gearbox oil sump and high-speed shaft bearing temperature, nacelle and exterior temperature, pitch angles, and pitch angle rates.

4.2.4 Test program

The measurement and data acquisition equipment were active from April 25$^{\text{th}}$ to July 20$^{\text{th}}$, 2023. During this period, the turbine was operated using the standard controller parameters to reproduce normal working conditions. The acquired data described in Sections 4.2.1 to 4.2.3 were then postprocessed and binned together into 10-minute files for ease of handling and analysis. All three data acquisition systems were synchronized using the Coordinated Universal Time (UTC) timestamp, verified by comparing the rotor speed recorded by the controller versus the rotor speed as calculated from the main-shaft azimuth encoder and FOSs. In total, 837 10-minute files were recorded with all data acquisition systems operational and with a minimum of 150 kW, 238 of which were above 50 % rated torque. The wide range of operating conditions experienced during the test campaign covered the complete power curve of the turbine [102].

4.2.5 Filtering of fiber-optic sensor signals and conversion to strain

Figure 4.4 shows the raw spectral shift recorded by the interrogator for sensors T01, T03, and T06 during an example 10-second portion on April 25$^{\text{th}}$ beginning at 20:45:55 UTC. The moving average was subtracted from the raw spectral shift to remove the specific spectral offset and thermally induced strain from each FOS. The remaining filtered signal is assumed to be produced by only the planet passage effect and can then be converted to strain using a linear conversion factor of 840.34 $\mu\epsilon$/nm as shown in Figure 4.5.

4.2.6 Calibration of torque measurement with main-shaft strain gauges

The 10-minute average of the main-shaft Wheatstone torque bridge was calibrated through a linear regression to the estimated rotor mechanical torque derived from the turbine operation parameters for all datasets with a minimum value of 150 kW of total power production. Because the strain gauges were installed *in situ* uptower, the measured strain was correlated to the main-shaft mechanical torque estimated from the power managed by the turbine controller and rotor speed measurements along with an assumed factor of 1.1 to account for typical power converter, generator, and gearbox efficiency losses. For the purposes of this work, such a reference torque is sufficient to compare the relative accuracies of the different methods used to determine torque from the FOSs. Figure 4.6 shows the resulting correlation. As expected, a linear relationship was found with an interpolation coefficient of 917 kNm/V. The main-shaft bending measurements were also calibrated by relating the response from the corresponding Wheatstone bridges in turbine idling conditions to the expected bending moment of 395 kNm at the Wheatstone bridge location, which was derived from a force balance of the drivetrain subject to the approximate rotor mass of 34,000 kg and the counterbalancing effect of the gearbox mass. In this calculation, the drivetrain tilt angle of 6 degrees was also accounted for and the spherical main bearings were assumed to support only radial and/or axial loads, but not any moments [103]. These methods are common in field testing of installed wind turbines [45].

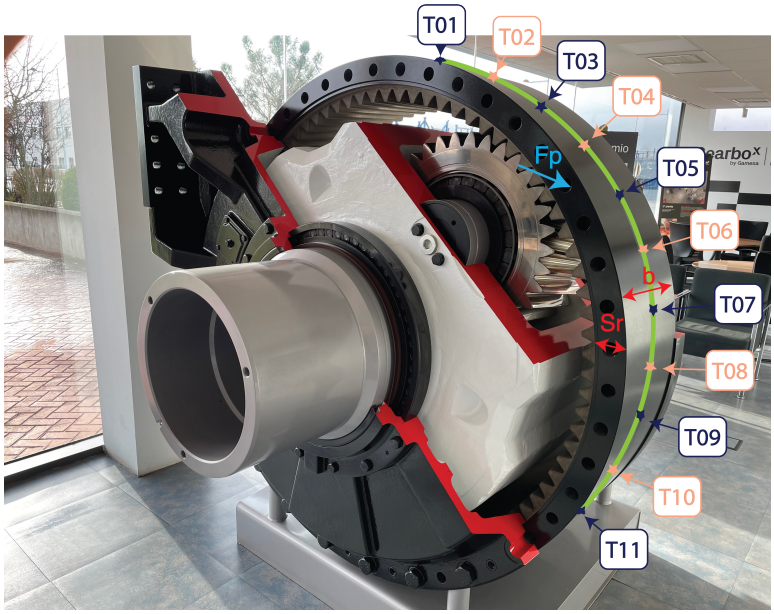

(a)

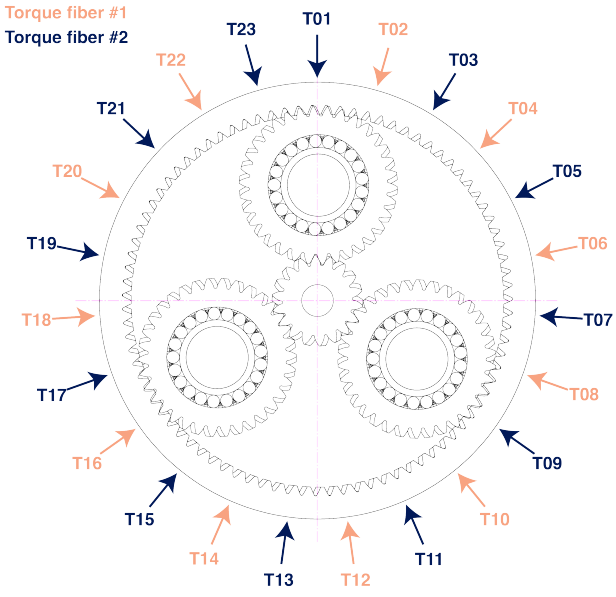

(b)

Figure 4.2: G97 2 MW gearbox with (a) representation of fiber-optic strain sensors on the outer surface of the first stage ring gear installed for torque measurements (adaptation of figure from Gamesa Gearbox (`https://www.gamesagearbox.com/wind-technology/`) and (b) angular placement of the 23 FBGs labeled T01 to T23, with the 12 sensors in blue belonging to fiber number one, and the 11 sensors in red to fiber number two.

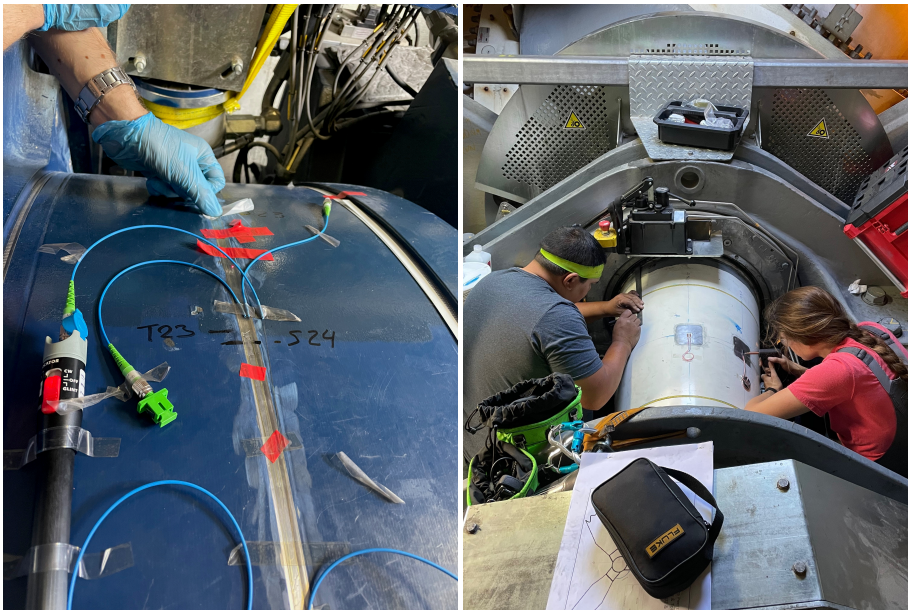

Figure 4.3: Sensor installation process of (a) ring gear FBGs and (b) main-shaft strain gauges. Photos from Unai Gutierrez-Santiago, Siemens Gamesa Renewable Energy, NREL 85910 and 91649.

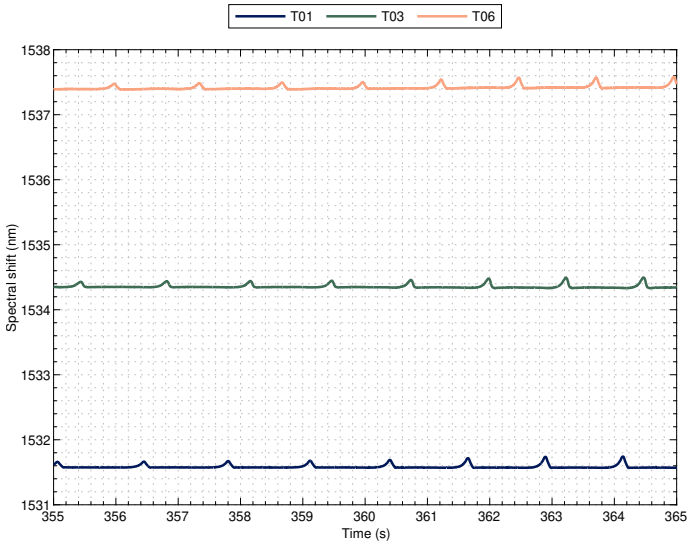

Figure 4.4: Example raw spectral shift from fiber-optic for sensors T01, T03, and T06.

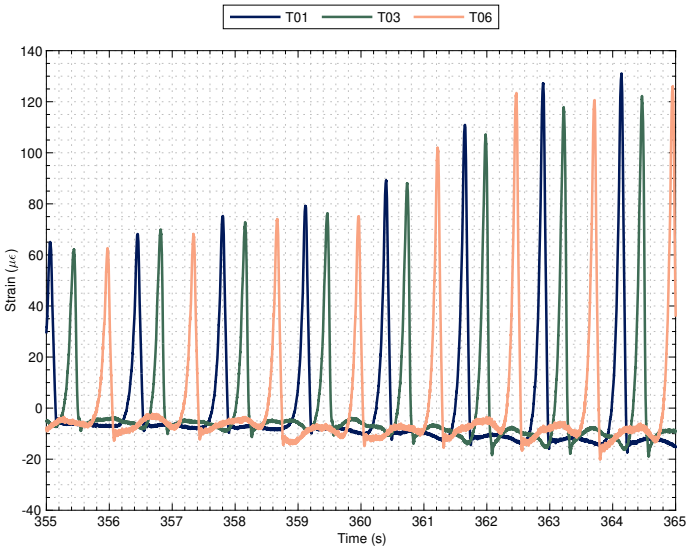

Figure 4.5: Example of filtered strain from raw spectral shifts of sensors T01, T03, and T06.

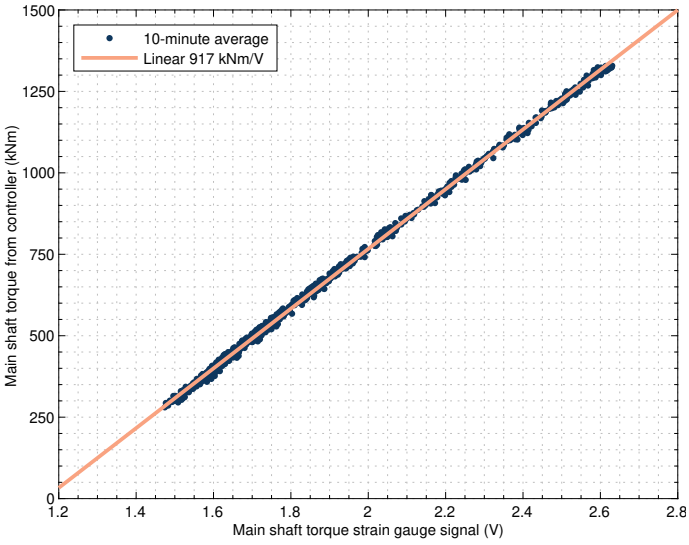

Figure 4.6: Linear interpolation between main-shaft strain gauge response and mechanical torque derived from turbine controller using 10-minute average values from April 25th to July 20th.

4.3 Measuring dynamic mechanical torque with ring gear fiber-optic sensors

This section describes how the strain signals from the fiber-optic sensors placed on the outer surface of the ring gear are processed to derive the dynamic mechanical torque applied to the gearbox. Two alternatives to derive torque from strain are examined using an example 10-minute period of turbine operation on April 25th beginning at 20:40 UTC. The wind speed at hub height, the rotor speed, and the total produced power during this 10-minute period are shown in Figure 4.7. For the first 2 minutes, the wind speed was just under the rated wind speed of 11 m/s, so the turbine was operating the rated rotor speed of 15.96 rpm, but slightly less than the rated power of 2 MW. During the next 4 minutes the wind speed dropped to as low as 5 m/s, so the turbine operated with variable rotor speed and power as low as 300 kW. For the last 4 minutes, the wind speed increased quickly to as high as 15 m/s, so the turbine operated largely at rated rotor speed and torque.

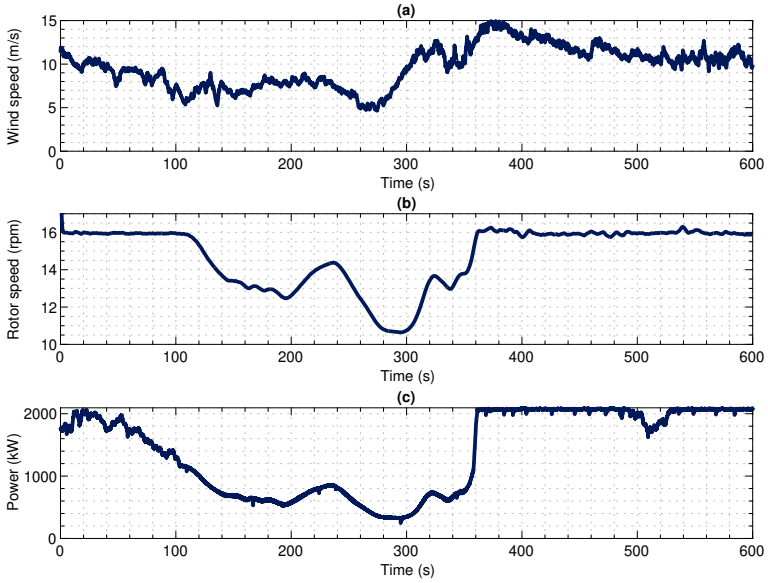

Figure 4.7: Wind speed at hub height, rotor speed, and total produced power recorded for the example 10-minute period of turbine operation on April 25th beginning at 20:40 UTC.

4.3.1 Peak-to-peak method

This section describes how the fiber-optic strain data were processed to obtain a torque estimate based on the change of the peak-to-peak (P2P) strain values over time [86]. Once signals have been filtered as described in Section 4.2.5, the remaining signal is assumed to be entirely caused by strain at the FBG as shown in Figure 4.5. The signals of all 23 sensors exhibit large tensile strain peaks followed by a compressive peak as each of the three planet gears passes the sensor, which occurs three times per-rotor revolution (3P). Figure 4.8 shows the identified tensile and compressive peaks of sensors T01, T03, and

T06 over a 5-second portion of the example, during which each sensor witnessed 8 planet passes. The red squares depict the moment when the main-shaft azimuth angle equaled zero, signaling a complete revolution of the rotor. Figure 4.9 shows the resulting P2P values for the same period. The P2P strains measured at each sensor location are slightly different in magnitude and occur at slightly different times. Several factors are expected to play a role in the observed differences in the torque-to-deformation relationship. Although the ring gear itself is axisymmetric as shown in Figure 4.2b, the front and rear housings connected to the ring gear and especially the torque reaction arms are not as shown in Figure 4.1b and thus result in a nonuniform stiffness for the complete system. Because there are 23 sensors and 87 ring gear teeth, the sensors each have different circumferential positions relative to the ring gear teeth. If the distribution of load over the teeth is not exactly the same, it can result in slightly different strain at each sensor location. Finally, the bonding between the fiber and the ring gear is a manual process that could lead to differences in sensitivity to strain of each sensor, especially for this *in situ* installation.

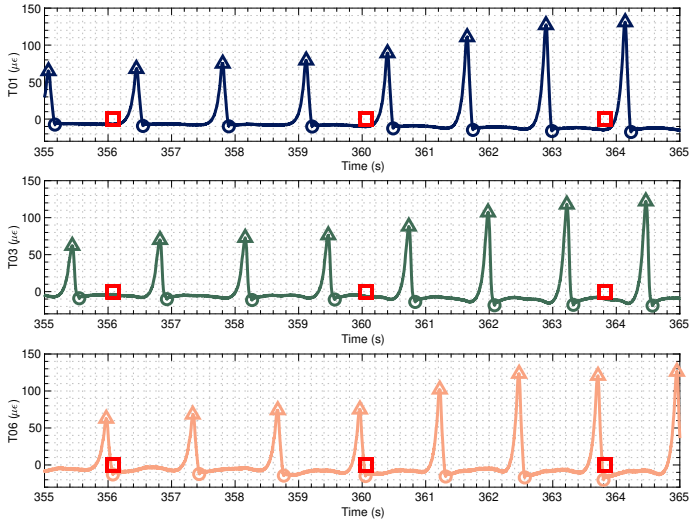

Figure 4.8: Example P2P strain processing for sensors T01, T03, and T06: peak detection.

Although torque can be estimated from the P2P strain of just a single FOS, doing so would only result in a torque measurement at the time of each planet passage at a frequency of 3P. Combining the P2P strain for all the sensors around the ring gear circumference into a single measure would result in a torque measurement at a much higher frequency of 23 times 3P; however, the identified minor differences in strain for each sensor must be accounted for. In this work, the average P2P value of each sensor was used to normalize and combine the P2P strains into a single measure. Like the main-shaft strain gauges, the FOSs could not be calibrated to torque because of the *in situ* installation. Instead, the average values of normalized P2P (nP2P) strain and mechanical torque measured by the main-shaft strain gauges for every revolution of the rotor were compared as shown in Figure 4.10. A linear relationship is observed with an interpolation coefficient of

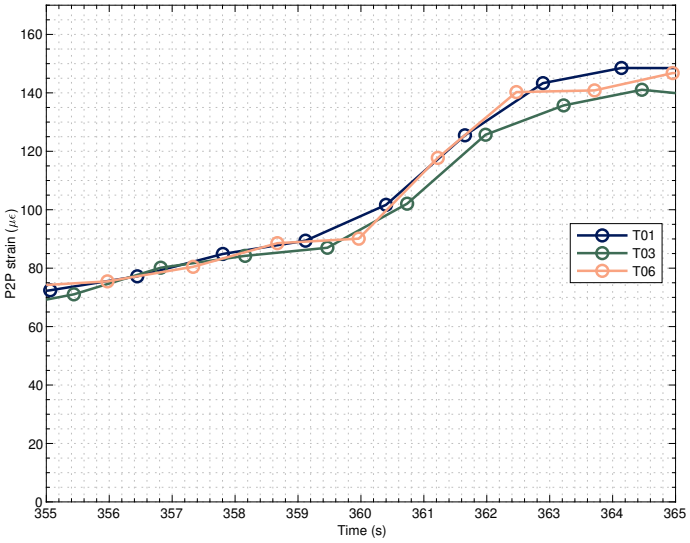

Figure 4.9: Example P2P strain processing for sensors T01, T03, and T06: P2P strain magnitude.

9.43 kNm/$\mu\epsilon$. Using this, the nP2P strains can be converted to dynamic mechanical torque for every detected planet passage.

4.3.2 Operational deflection shape method

This section describes another approach to derive torque from the FOSs based on operational deflection shapes (ODSs). ODSs are similar to natural mode shapes, but because they are caused by periodic external excitations rather than being a structural property of the gearbox, the term ODS is used. In a previous work, [36] described the subspace multivariable output-error state-space (MOESP) algorithm used to identify models from the FOSs and the state reconstruction procedure to quantify the contribution of the ODSs. The contribution of the planet-passing ODSs showed a strong correlation with the dynamic mechanical torque in the gearbox and, therefore, provides a means to estimate torque. The first step of this method is to identify the ODSs from a suitable training dataset at continuously rated operating conditions. The first such conditions occurred on May 5th at 23:00 UTC, in which the turbine was operating at rated speed and power for the entire 10-minute period.

The sampling frequency plays an important role in the efficiency of the numerical implementation of the MOESP algorithm. The original sampling frequency of 2,000 Hz for the FOSs was downsampled to 60 Hz, which matched the sampling frequency of the main-shaft strain gauges. This frequency is still suitable, as it easily captures the 3P planet-passing and gear mesh excitation frequencies for the planetary stage, which at the rated rotor speed of 15.96 rpm (0.266 Hz) are 0.798 Hz and 23.140 Hz, respectively, for the ring gear with 87 teeth and the sun pinion with 18 teeth. Once the sampling frequency has been chosen, three parameters need to be defined to execute the MOESP algorithm [94, 98, 104]. These

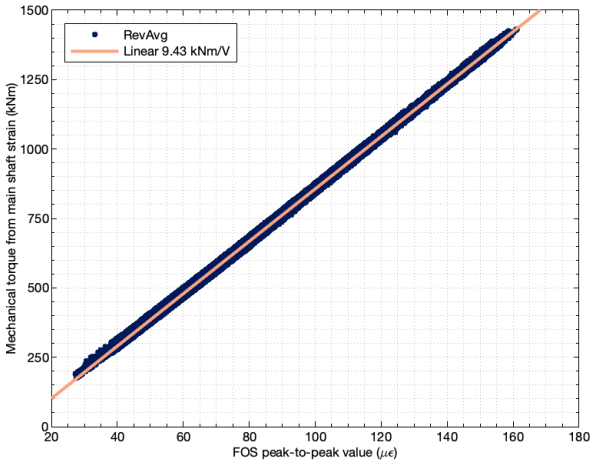

Figure 4.10: Linear interpolation between nP2P values and main-shaft mechanical torque using main-shaft revolution average values from April 25$^{\text{th}}$ to July 20$^{\text{th}}$.

parameters are the number of samples N, the number of block rows s, and the system order n. For the present study, $N = 12,800$ samples per sensor accounting for approximately one-third of the 10-minute data sample, $s = 64$ block rows, and $n = 20$, which is a model order equivalent to 10 oscillatory modes. The observed part of the eigenvectors identified by the MOESP algorithm are the system's mode shapes. The frequency and damping ratios of each ODS, computed from the identified eigenvalues, are listed in Table 4.1. The damping ratios are all very small, as expected for a stiff, metal structure such as the ring gear, resulting in periodic, undamped dynamic behavior. All identified frequencies match with the 3P planet-passing frequency and its harmonics. Figure 4.11 shows an animation of the ODSs that correspond to the first three orders of the planet-passing frequency (3P).

With a suitable transformation matrix, it is possible to diagonalize the identified system matrix $\bar{A}$ into the so-called modal form denoted as $\bar{A}_M$. The same transformation matrix can be used to obtain the output matrix $\bar{C}_M$. The associated states $\hat{x}$ and the output measurements $\hat{y}$ can be reconstructed using the "one-step-ahead" predictor. For this predictor, we use a Kalman gain $\bar{K}_M$ estimated from the measured data as the optimal estimator. The accuracy of the identified system was evaluated using the variance accounted for (VAF) metric between the measured signals y and the predicted $\hat{y}$, representing the strain from the FOSs. The VAF was computed using a different section of the 10-minute training recording used for training, which is the validation dataset. The system's initial state is estimated for the validation part of the dataset using the identified models. Then, the system state and output signals can be reconstructed, assuming the system behaves as an autonomous system oscillating from a nonzero initial condition. An average VAF value for the 23 FOSs of 98.45 % was achieved with the above-mentioned identification parameters. Such a high VAF value indicates that the identified ODSs can reproduce the behavior of the gearbox accurately, and the contribution of the periodic excitations accounts for

Table 4.1: ODS frequencies in rated conditions identified by the MOESP algorithm using $s = 64$ and $n = 20$.

Mode	Frequency (Hz)	3P Order	Damping ratio	Acronym
1	0.80	1.00	2.15e-5	3P
2	1.60	2.00	1.24e-5	2x3P
3	2.39	3.00	1.16e-5	3x3P
4	3.19	4.00	1.10e-5	4x3P
5	3.99	5.00	9.29e-5	5x3P
6	4.78	6.00	1.26e-5	6x3P
7	5.58	6.99	1.34e-5	7x3P
8	6.38	7.99	1.30e-5	8x3P
9	7.18	8.99	1.86e-5	9x3P
10	7.97	9.99	3.91e-5	10x3P

almost all the energy in the measured FOS strain signals.

However, the results were not close to the measured signals when recordings with variable speed were analyzed. For normal operating conditions, where the speed of the turbine is constantly changing, the behavior is no longer periodic in the time domain, so the identified system representation does not hold. To overcome this, the measured strain signals were resampled at fixed angular intervals. In the angular domain, the system exhibits a periodic behavior and can be represented by the ODSs. The strain signals were angularly resampled by using their periodic 3P behavior, previously shown in Figure 4.9. The angular resolution was chosen to match the time resolution at rated speed. Figure 4.12 compares the main-shaft torque, the nP2P strain, and the modules of the dimensionless states associated with each ODS for the example 10-minute recording from April 25$^{\text{th}}$ at 20:40 UTC. The trends for the nP2P strain and the modules for the dimensionless states are the same as the main-shaft torque, giving confidence that both the FOS strain analysis methods and any of the ODSs can be used to measure dynamic mechanical torque. When the system is represented in diagonal form, via a suitable similarity transformation, two conjugate states are associated with each ODS with equal modules.

In order to find the relationship between the module of the states ($\hat{x}$) and the mechanical torque, again, the average values of the state modules and mechanical torque measured by the main-shaft strain gauges for every full revolution of the rotor were determined and are compared as shown in Figure 4.13. A linear relationship is observed for every ODS, each with its own interpolation coefficient as listed in the legend. Using these coefficients, the modules of the states can be converted to dynamic mechanical torque for every sample.

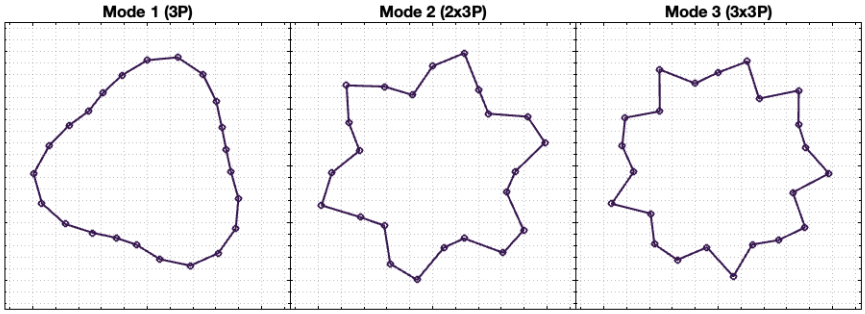

Figure 4.11: Simulated strains on the ring gear associated with the first three planet-passing mode shapes. The axis labels and units have been omitted as the deformations were scaled for better representation. An animation of a planet carrier revolution is available in a supplementary video file [105].

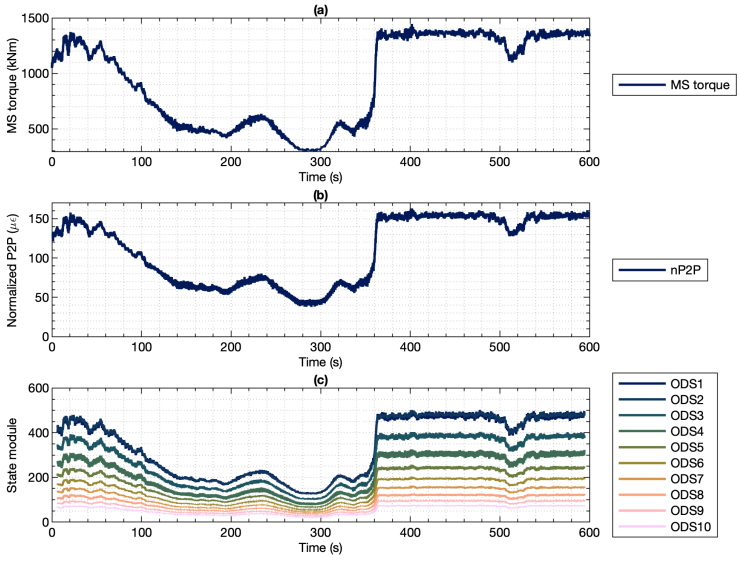

Figure 4.12: Evolution of the module of each state associated with the identified ODSs for the 10-min recording from April 25th at 20:40 UTC.

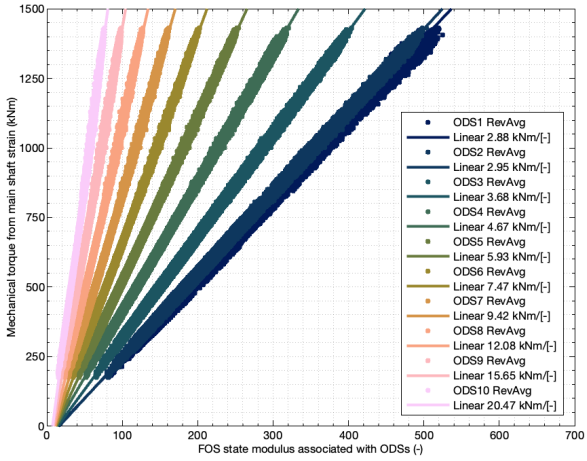

Figure 4.13: Linear interpolation between modules of reconstructed states for each ODS and main-shaft mechanical torque using main-shaft revolution average values from April 25th to July 20th.

4.4 Results

This section presents the key findings obtained from the field validation campaign. First, we examine the dynamic mechanical torque measurements derived from the FOSs placed on the ring gear and their differences compared to those from the main-shaft strain gauges. Then, we quantify the accuracy of the fiber-optic measurements and analyze the effect of the operating conditions experienced by the turbine throughout the field validation campaign.

4.4.1 Accuracy assessment

Using the linear interpolation coefficients shown in Figures 4.10 and 4.13, it is possible to convert the nP2P values and ODS state modules into dynamic mechanical torque. In this work, these relationships were defined using average values over a full rotor revolution for the complete measurement campaign. However, for a serial implementation, it is envisaged that the FOSs could be installed during the gearbox assembly and fully calibrated to mechanical torque during the end-of-line gearbox test. For the example 10-minute data recording analyzed in Section 4.3, a comparison between the dynamic mechanical torque measured by the main-shaft strain gauges and the torque measurements derived from the FOS strain signals is shown in Figure 4.14. Both the nP2P and third-order (ODS3) torque measurements closely match the dynamic mechanical torque measurements from the main-shaft strain gauges, even in the quick rise in torque from 600 kNm to the rated 1,320 kNm that occurs in only 10 seconds. The error between the nP2P and ODS torque methods when compared to the main-shaft torque is typically less than 50 kNm, even during this highly dynamic period. Figure 4.15 shows the dynamic mechanical torque measurements for another 10-minute recording from May 31st at 22:40 UTC. This period features more operation in the variable torque and rotor speed region, with even more changes in torque from as low as 300 kNm to rated for brief periods. In some cases, the torque rises and falls 300 to 400 kNm in as little as 5 seconds at a time. In this variable-speed region, it does appear, though, that the torque errors increase slightly more but are still typically less than 70 kNm.

The root-mean-square error (RMSE) was used to assess the accuracy of the dynamic mechanical torque measurements [106]. For every 10-minute recording, such as the examples shown in Figures 4.14 and 4.15, the error was computed as the difference between the dynamic mechanical torque measurements from the main-shaft strain gauges and those derived from FOS magnitudes for each time sample. The main-shaft strain gauge signals were logged with a sampling frequency of 60 Hz. To perform a sample-by-sample computation of the error, the torque measurements obtained using the peak-to-peak method had to be interpolated because a torque value can only be obtained when any of the FBGs detects a planet passage, which generally leads to a nonuniform spacing of the torque samples. In the case of the ODS method, the FOS signals were angularly resampled as explained in Section 4.3.2, and therefore, the main shaft torque was also resampled using the same fixed angular intervals to make the instantaneous error evaluation possible. It is common practice to normalize the RMSE values to assess the magnitude of errors from the perspective of the measured quantity. However, there is no consistent means of normalization in the literature [107]. In this work, the RMSE values were normalized using the rated torque. Table 4.2 summarizes the normalized RMSE values of the 10-minute record-

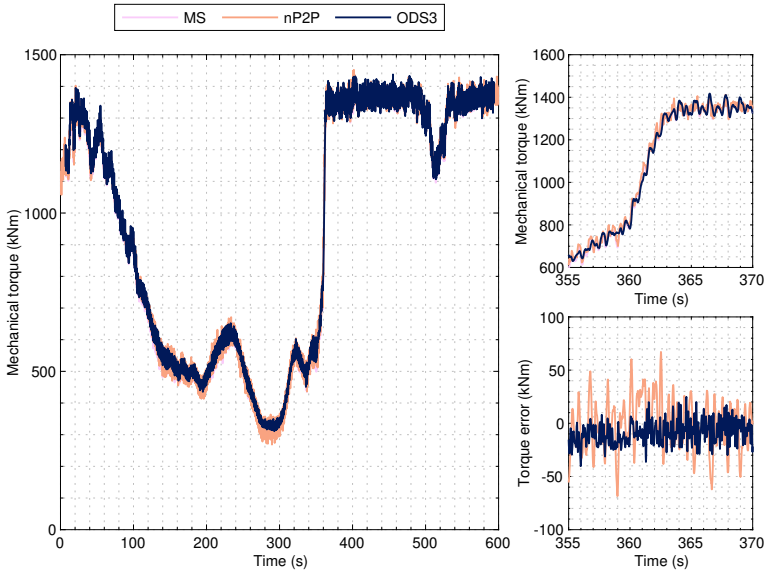

Figure 4.14: Comparison of torque measurements derived from fiber-optic and main-shaft strain signals for the example on April 25th at 20:40 UTC.

ings from April 25th at 20:40 UTC and May 31st at 22:40 UTC shown in Figures 4.14 and 4.15. The torque RMSE evaluation was also performed for all 837 10-minute recordings from the full validation campaign. These recordings were selected using the minimum produced power requirement of 150 kW. A single normalized RMSE value was obtained from each 10 minute, and the average of all 837 values is also shown in Table 4.2. Depending on the method to derive torque, the RMSE torque errors range from 15 to 30 kNm, which when normalized are approximately 1 to 2.5 %. These normalized RMSE values are considered very low, within the expected accuracy of the main shaft strain gauges. Examining just the nP2P and ODS3 methods, the errors are even lower, with normalized errors less than 1.5 %. For brevity, in Table 4.2, only the ODSs corresponding to the first three orders of the planet-passing frequency (ODS1, ODS2, and ODS3) are shown because the fourth and higher orders resulted in higher errors than the first three.

Table 4.2: Normalized RMSE of torque measurements on a time-based approach.

	RMSE (kNm)			Normalized RMSE (%)		
Method	**Apr 25th 20:40 UTC**	**May 31st 22:40 UTC**	**Mean 837 files**	**Apr 25th 20:40 UTC**	**May 31st 22:40 UTC**	**Mean 837 files**
nP2P	15.356	16.708	15.768	1.163	1.266	1.195
ODS1	28.434	28.514	20.923	2.154	2.160	1.585
ODS2	20.054	19.057	15.611	1.519	1.444	1.183
ODS3	22.806	18.476	18.015	1.728	1.400	1.365

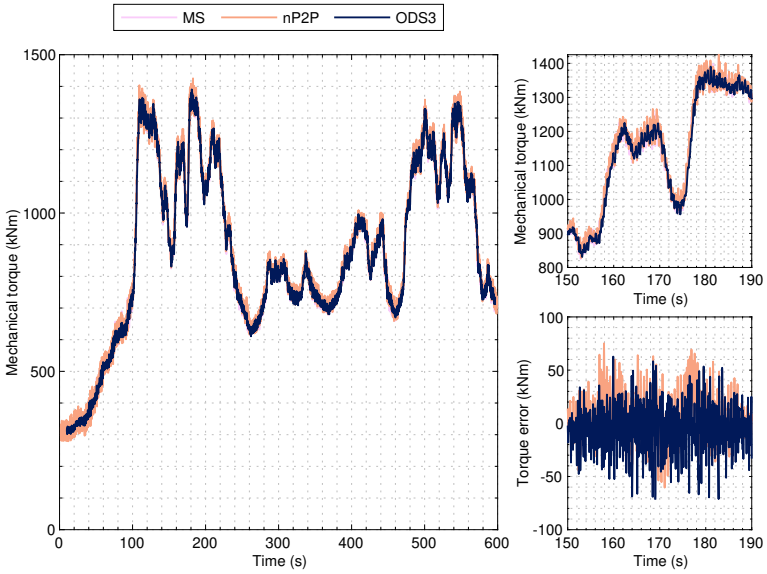

Figure 4.15: Comparison of torque measurements derived from fiber-optic and main-shaft strain signals on May 31st at 22:40 UTC.

For fatigue life estimations, because the gears and bearings are subjected to stress cycles even under a constant torque load, the IEC 61400-4 gearbox design standard recommends binning the loads using a load duration distribution approach. The load bins can be the time spent at a given load (i.e., load duration distribution (LDD)) or the number of revolutions (i.e., load revolution distribution (LRD)). The number of gear stress cycles depends on the rotational speed, and therefore, the shaft speed is taken into account in the LDD or LRD. As shown in Section 4.3.1 the rotor or main shaft speed can also be derived from the FOSs. For the 837 analyzed 10-minute recordings, the accuracy of the mechanical torque derived from the FOSs was assessed for both LDD and LRD approaches. For the LDD, each 10-minute recording was considered as a time bin, and its average torque value was computed. Similarly, for the LRD, the mechanical torque was averaged for the 113,499 full main-shaft revolutions contained in the 837 files. Table 4.3 summarizes the overall RMSE in kNm and the normalized RMSE in % for the full measurement campaign using the errors of each 10-minute file and each revolution. As can be seen, the normalized RMSE values drop below 0.7 % for both the nP2P and ODS3 methods.

Therefore, these highly accurate results allow the use of dynamic mechanical torque from the FOSs for applications like remaining useful life estimation and potentially even wind turbine control. Although the nP2P method has a similar error as the first 3 ODS methods, the ODS methods have the advantage of a greater sampling frequency. The nP2P method can only provide a torque estimate when a planet passage is detected, in this case at 23x3P per revolution. The ODS method, however, can give a higher sampling frequency because the state associated with the ODSs can be evaluated at every time step and, therefore, can be as high as the sampling frequency. Because it uses simple linear algebraic

Table 4.3: Normalized RMSE of torque measurements based on LRD and LDD approaches.

	Average RMSE (kNm)		Average Normalized RMSE (%)	
Method	**LRD**	**LDD**	**LRD**	**LDD**
nP2P	8.567	8.292	0.649	0.628
ODS1	15.152	13.585	1.148	1.029
ODS2	9.539	8.964	0.723	0.679
ODS3	9.013	8.542	0.683	0.647

operations, it can also potentially be implemented in real time. Another advantage of ODS method is that we can recursively implement the system identification algorithm to identify ODS at different times and track the deflection shapes, which could potentially be used for gearbox fault detection. Additionally, the nP2P method encounters difficulty identifying the planet passage peaks at lower torque levels.

4.4.2 Analysis of effect of wind turbine operational parameters

In this section, the effect of wind turbine operating conditions on the accuracy of the mechanical torque measurements from the FOSs presented in Section 4.4.1 is assessed using the LRD approach. By averaging the torque errors over full revolutions of the rotor and pairing them with the synchronously logged additional wind turbine operating parameters, like wind speed, main-shaft bending moments, and ring gear temperature, it is possible to assess the effect of those operating conditions on the accuracy of the FOSs. Figure 4.16 shows the error between the mechanical torque measurements from the nP2P and ODS methods and the main-shaft strain gauges across the average wind speed of each LRD bin. The errors are lowest above the rated wind speed of 11 m/s in which the turbine is typically operating at constant rotor speed and mechanical torque, even in wind speeds as high as 21 m/s. The errors are slightly higher in the variable rotor speed region between 6 and 10 m/s, in which the speed, torque, and blade pitch angles are all frequently changing.

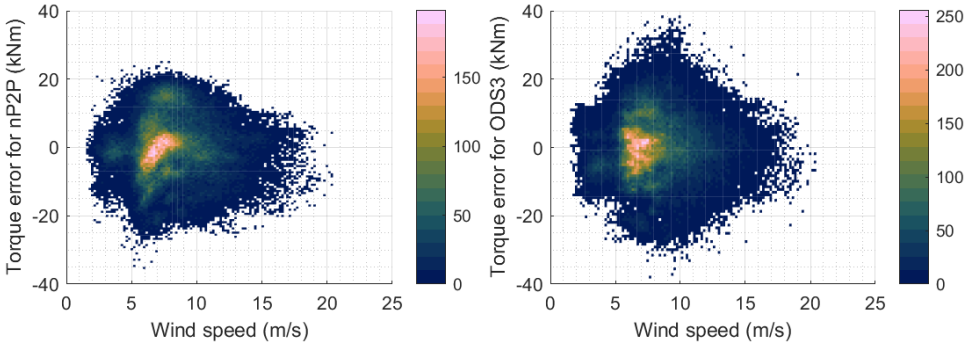

Figure 4.16: Effect of wind speed at hub height on the average RMSE for (a) nP2P and (b) ODS3 torque measurement methods for each rotor revolution from April 25th to July 20th.

Figure 4.17 shows the error between the mechanical torque measurements from the nP2P and ODS methods and the main-shaft strain gauges across the average main-shaft bending moment of each LRD bin. The majority of the main-shaft bending moments experienced were around 400 kNm, which is close to that caused by the rotor overhung weight moment at the main-shaft bending gauge location described in Section 4.2.2. In many operating conditions, slightly positive and negative wind shear can relieve or add to the main shaft bending moment, respectively, but these moments do not appear to have much effect on the torque error estimate.

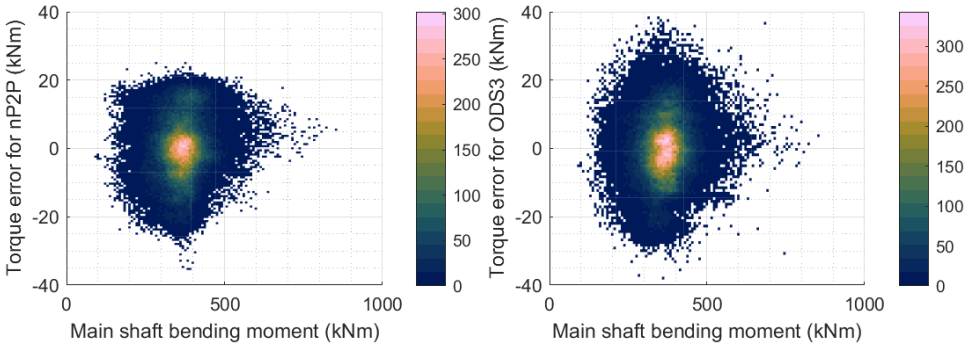

Figure 4.17: Effect of main shaft bending moment on the average RMSE for (a) nP2P and (b) ODS3 torque measurement methods for each rotor revolution from April 25th to July 20th.

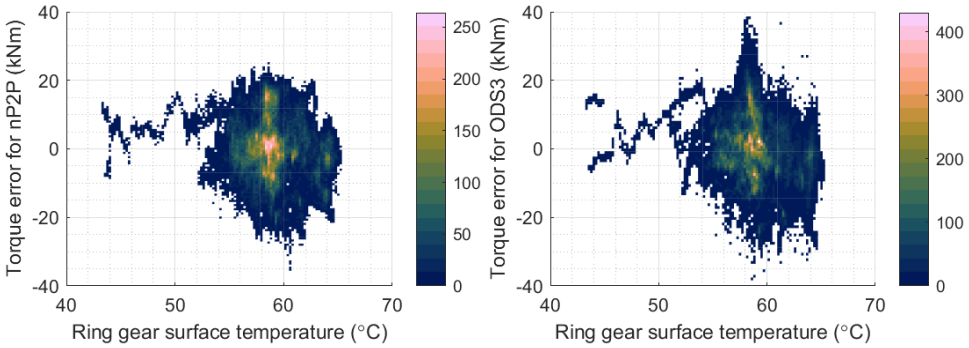

Figure 4.18: Effect of ring gear surface temperature on the average RMSE for (a) nP2P and (b) ODS3 torque measurement methods for each rotor revolution from April 25th to July 20th.

One of the concerns when evaluating the accuracy of the FOS measurements was to understand the effect of ring gear temperature on the FBGs. For that purpose, the FOS strains were correlated to the measurements from the ring gear surface temperature sensor described in Section 4.2.2. As Figure 4.18 shows, no appreciable correlation was observed between the torque errors and the ring gear temperature for either analysis method over

a wide range of ring gear temperatures from 43 to 66 °C. Typical operating temperatures ranged from 50 to 65 °C. From this we can conclude that both the nP2P and the ODS methods are robust to temperature variations.

The effects of other operating variables like wind turbulence intensity, yaw misalignment, and blade pitch angles on the torque error were also found to be negligible, similar to previous analysis of the effect of these parameters on the mesh load factor [102]. This is aligned with the expected behavior of the four-point-mount drivetrain configuration under test described in Section 4.2.

4.5 Conclusions

Accurate knowledge of the mechanical torque duty cycle of wind turbine gearboxes has become essential in modern designs, as maintaining or even improving gearbox reliability with increasing torque density demands is proving to be challenging. In many wind turbines, the mechanical torque is estimated from the generator electrical operational parameters; however, there are inherent uncertainties in the gearbox and electrical system efficiencies that vary with load, temperature, and time. Further, the electrical torque is zero in transient conditions, but highly dynamic mechanical torque is still present. Direct measurement of mechanical torque in the rotating system can be accomplished but can be costly.

In this work, a cost-effective method of measuring the dynamic mechanical torque based on fiber-optic strain sensors placed on the outer surface of the gearbox ring gear of a Gamesa G97 2 MW wind turbine was validated over a 3-month field test campaign. The fiber optic sensors measure the radial deformation of the ring gear, which is proportionate to the mechanical torque. The dynamic mechanical torque derived from the fiber optic strain sensors were compared to torque derived from traditional strain gauges installed on the main shaft with an average normalized root-mean-square error of less than 0.7 % using the load revolution distribution analysis. The effect of operating conditions on the torque estimate was also investigated, without an appreciable or consistent influence from wind speed, main-shaft bending moment, or ring gear temperature. The method based on the third planet-passing operational deflection shape has several advantages over the peak-to-peak method, such as a higher sampling frequency and potential for real-time application, and therefore is the preferred method. The fiber-optic strain sensors' successful operation during the complete test campaign demonstrated a robust and accurate solution for fleet-wide enhanced gearbox remaining useful life estimation that has been increased to a technology readiness level of 7 as defined in ISO 16290.

5

Experimental evaluation of the mesh load factor (K_γ) of a 6MW wind turbine gearbox

The significant increase in rotor diameters seen in modern wind turbines has pushed gearbox manufacturers to introduce technological innovations to increase the torque density of current designs. Driven by the need to lower the cost of energy from wind and size limitations imposed by logistic constraints in onshore wind, a trend has emerged to increase the number of planetary stages and the number of planet gears per stage. One of the main challenges of next-generation gearbox designs is sharing the load evenly between a high number of planets. This chapter presents an experimental evaluation of the mesh load factor of a modern 6MW wind turbine gearbox with five planets in the first planetary stage. Results from the traditional method, based on tooth root strain gauges, and from strain measurements in the outer surface of the ring gear are described and assessed. Both experimental approaches have yielded lower mesh load factor values than the default values required in the standard "Design requirements for wind turbine gearboxes" IEC 61400-4. Since the mesh load factor is used for gear rating and sizing, a lower value allows for a more optimized gearbox design, which leads to a significant improvement in torque density and cost.

5

This chapter is based on the following publication: *U. Gutierrez Santiago. Experimental evaluation of the mesh load factor (K_γ) of a 6MW wind turbine gearbox* [108]. Yellow is the fifth color of the rainbow when arranged by increasing wavelength. Yellow has a wavelength between 570 nm and 580 nm. All the FBGs used throughout this dissertation reflect light within the 1525 nm - 1575 nm bandwidth. That is well above the upper limits of the humanly visible part of the spectrum. They do, however, "light up" when connecting a visual fault detector, which emits light around 650nm. The visible spectrum is the narrow portion within the electromagnetic spectrum that can be seen by the human eye, also referred to as the optical spectrum. Other forms of electromagnetic radiation that we cannot see include radio, gamma, and microwaves. The cells in our eyes, called cones, are sensitive to the wavelengths found in the visible spectrum. They allow us to see all the colors of the rainbow. Various sources define visible light as narrowly as 420 nm - 680 nm to as broadly as 380 nm – 800 nm. Under ideal laboratory conditions, people can see infrared up to at least 1050 nm; children and young adults may perceive ultraviolet wavelengths down to about 310 nm. In order of increasing wavelength and decreasing frequency, the electromagnetic spectrum includes gamma rays, X-rays, ultraviolet, visible light, infrared, microwaves, and radio waves.

5.1 Introduction

Reducing the cost of energy (CoE) has become one of the main research drivers in Wind Energy [68]. As a result, wind turbines have experienced an astonishing increase in rotor diameter. In the overall breakdown of costs of onshore wind, the gearbox is one of the main contributors due to the associated capital expenditure and the considerable impact on operation and maintenance costs [69]. In this context, gearbox manufacturers have striven to reduce the cost of gearboxes by increasing the torque density of modern designs. Multiple technological innovations have been introduced, e.g., like new materials, improved manufacturing tolerances, and additional surface finishing techniques. However, increasing the number of planetary stages and the number of planet gears in each stage are the two most promising avenues to increase the torque density and keep the gearbox diameter within the limitations imposed by logistic constraints [12]. One of the main challenges of next-generation gearbox designs is sharing the load evenly between the high number of planets. The load-sharing behavior of planetary gears has been extensively studied in the literature. Kahraman et al. researched its dependency on manufacturing errors and the associated dynamic effects [55], and presented an experimental study in [56]. Singh, A. proposed an analytical formulation for the relationship between planet load sharing behavior and positional errors [57]. These studies were conducted on smaller module gears for automotive or helicopter applications. Guo, Y. and Keller, J. generalized this analytical formulation for wind turbine gearboxes with a three-planet, floating epicyclic configuration [28, 54]. Little evidence can be found in the literature for a higher number of planets. New analytical tools are needed to predict the load-sharing behavior in modern wind turbine gearboxes with more planets. These tools need to be demonstrated and validated through experimental evaluation.

For split path gear meshes, the gear rating standard ISO 6336-1 [58] defines the mesh load factor K_γ as the quotient between the highest load carried by a single path divided by the average load. In planetary gear stages, this corresponds to the highest load carried by a single planet divided by the average load of all planets. Design requirements for wind turbine gearboxes are set by the standard IEC 61400 – 4 [59]. This standard specifies default values of the load mesh factor K_γ as a function of the number of planets. These default values are given in Table 5.1.

Table 5.1: Mesh load factor K_γ values for planetary stages given by the standard IEC 61400-4 according to their number of planets.

Number of planets	3	4	5	6	7
Mesh load factor K_γ	1.10	1.25	1.35	1.44	1.47

For a high number of planets, the mesh load factors presented in Table 5.1 are conservative and would lead to gearbox designs with poor torque density values. The standard allows lower mesh load factor values if they are demonstrated by gear teeth root strain gauge measurements during prototype testing. Performing such tooth root strain measurements is complex and expensive. A recently developed method to measure torque using fiber optic strain sensors on the outer surface of the ring gear [65] has proven to

provide additional information about the way torque is shared by the different planets.

The main contribution of this study is to perform an experimental evaluation of the mesh load factor (K_γ) of a five-planet first planetary stage from a modern 6MW wind turbine gearbox. The traditional method to evaluate the mesh load factor based on strain gauge measurements in the gear teeth roots, has been compared against values obtained from the strain measurements on the outer surface of the ring gear to assess the new method. The results from both approaches have been compared to the requirements set by the standard IEC 61400 – 4 [59].

The remainder of this chapter is organized as follows, Section 5.2 describes the experimental procedure used to evaluate the mesh load factor K_γ. Section 5.2.1 covers the traditional method based on tooth root strain measurements, and Section 5.2.2 describes the method based on strain measurements on the outer surface of the ring gear using fiber-optic sensor. Section 5.3 discusses the results obtained with both signal processing procedures, and Section 5.4 draws the main conclusions of this work and suggests recommendations for future work.

5

5.2 Experimental evaluation of the mesh load factor K_γ

This study was conducted using a Siemens Gamesa Renewable Energy (SGRE) gearbox manufactured by Gamesa Energy Transmission (GET). The gearbox is a 3 stage gearbox, where the first and second are epicyclic planetary stages, and the third is a parallel stage. The first planetary has five planets and the second stage has three. The rated power of the gearbox is 6MW and weights approximately 44000 Kg. A full-scale prototype gearbox, instrumented with strain gauges in two roots of the sun gear and fiber optical strain sensors on the outer surface of the ring gear, was tested in a back-to-back test bench up to 100 % of its nominal torque. The first stage of this gearbox was chosen for this study because it is representative of current gearbox designs. With five planets, it provides a suitable case to evaluate the requirements of standard IEC 61400 - 4. All tests presented in this study were performed on the back-to-back test bench shown in Figure 1, property of the company DMT GmbH & Co. KG [79] at Krefeld (Germany) with electric motors of rated power of 7.5 MW.

5.2.1 Load mesh factor from sun gear root instrumentation

The traditional method to evaluate the mesh load factor is based on measurements from strain gauges installed in the gear tooth root. According to the standard IEC 61400 – 4 [59] these strain gauges are a compulsory part of the verification process of a new gearbox design and also serve to evaluate the gear mesh contact patterns and the load intensity distribution along the face width of the gears ($K_{H\beta}$). The measurement system was comprehensively described in [60]. However, it is worth emphasizing two critical items of the instrumentation:

- Location of strain gauges in the gear root: When a gear tooth is subjected to the mesh force as depicted in Figure 5.2, where α is the pressure angle. According to the standard ISO 6336 [58] the highest stresses can be found in the sections defined by the 30 degree tangents. In theory, these spots of maximum stress would lead to the highest possible signal-to-noise ratio. However, these spots also exhibit large stress

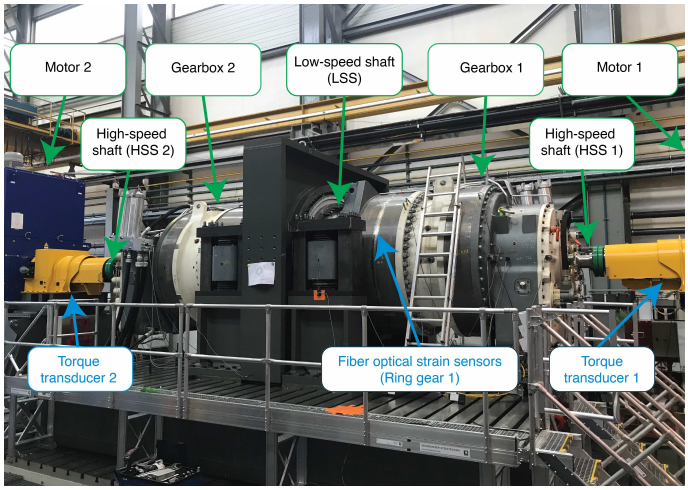

Figure 5.1: SGRE gearboxes on a back-to-back test bench (property of DMT GmbH & Co. KG).

gradients, making them very sensitive to positioning errors. In practice, the middle section between teeth offers a more suitable location to place the strain gauges. The strains are large enough to give good readings, and the smaller stress gradient reduces the sensitivity to positioning errors [60]. Additionally, the middle section offers more clearance with the mating tooth, which eases the physical installation process of the gauges and associated wiring.

- Number of strain gauges along the gear face width: The number of gauges to be installed along the face width in each root is a compromise between the required spatial resolution and the time and cost of the installation. In wind turbine gearboxes, considering the typical gear dimensions and the ratio of face width to the normal module, a number of 8 strain gauges has been found to produce satisfactory results [60]. Figure 5.3 shows how these eight gauges were distributed along a tooth root of the sun. This root was arbitrarily labeled as root number 1. The tooth root number 13, in the rotor's clockwise direction, was also instrumented in the same way for redundancy purposes.

The sun gear is a rotating part, and therefore, a special data acquisition system is needed. For the present study, bespoke uniaxial strain gauges together with gear alignment electronic modules developed by JR Transmission Dynamics [46] were used. These modules provide strain gauge conditioning using a Wheatstone bridge with a quarter bridge configuration; they are equipped with 8-channel synchronous acquisition and low-noise 12 bit analog to digital converters. Once the data is logged, a Bluetooth system transmits the data wirelessly. In this study, two roots (arbitrarily numbered 1 and 13) were instrumented with eight strain gauges on each root connected to independent 8-channel modules. Part of the electronic module can be seen in Figure 5.3. This picture was taken before soldering the wires from the strain gauges to the electronic module.

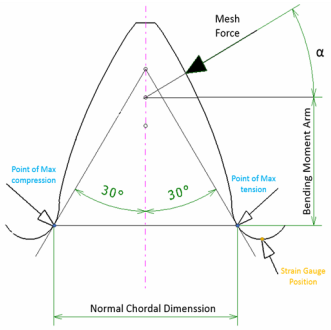

Figure 5.2: Strain gauge positioning in the gear tooth root.

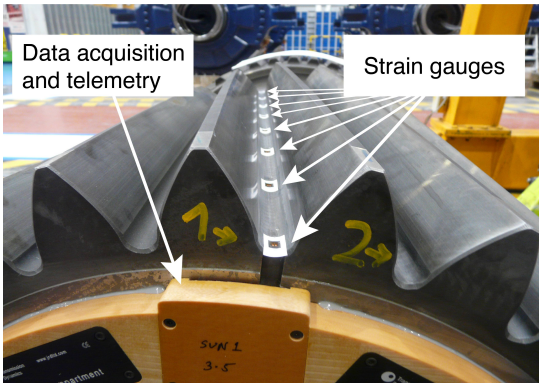

Figure 5.3: Strain gauge placement on a root of the first-stage sun gear.

5

In the case of the sun gear, the instrumented gear tooth will mesh with all the planets allowing the mesh load factor (K_γ) to be evaluated by comparing the mesh intensity of the gear meshes with the different planets. For each revolution of the sun relative to the carrier, a number of meshing cycles equal to the number of planets are observed in the time waveform of the strain gauges located in a tooth root of the sun gear. Figure 5.4 shows the raw data recorded from the eight strain gauges of the root number 1 of the sun. A once-per-revolution tachometer signal was also logged synchronously to identify the angular position of the sun relative to the carrier. The sun gear acts as a driven gear in the mesh with the planets. Therefore, during the start of the mesh cycle, when the tooth before the instrumented root is loaded, the strain gauge first observes a positive strain or traction. As the meshing cycle continues, the strain gauges will undergo compression or negative strain once the following tooth after the instrumented root becomes loaded.

The peak-to-peak strain value of the traction-compression cycle observed during the mesh cycle was chosen to measure the relative root stress of each strain gauge. Figure 5.5 shows the normalized peak-to-peak values of each strain gauge for the five mesh events of a single revolution of the sun gear relative to the carrier. The relative strain values are plotted against the axial position along the width of the sun gear shown in Figure 5.3. The rotor side corresponds to the left part of the graph and the generator side to the right. From the strain distributions shown in Figure 5.5, the area below each strain distribution was chosen as the mesh intensity value assigned to each gear mesh. This mesh intensity, denoted as i_{mesh}, can be computed using the following equation and was :

$$i_{mesh} = \sum_{n=1}^{N} b_n \Delta\delta_{n,mesh}, \tag{5.1}$$

where b_n is the length of face width covered by the strain gauge n and $\Delta\delta_{n,mesh}$ is the peak-to-peak strain measured by the strain gauge n during the mesh event. N is the total number of strain gauges placed along the face width. If we have P number of planets, then,

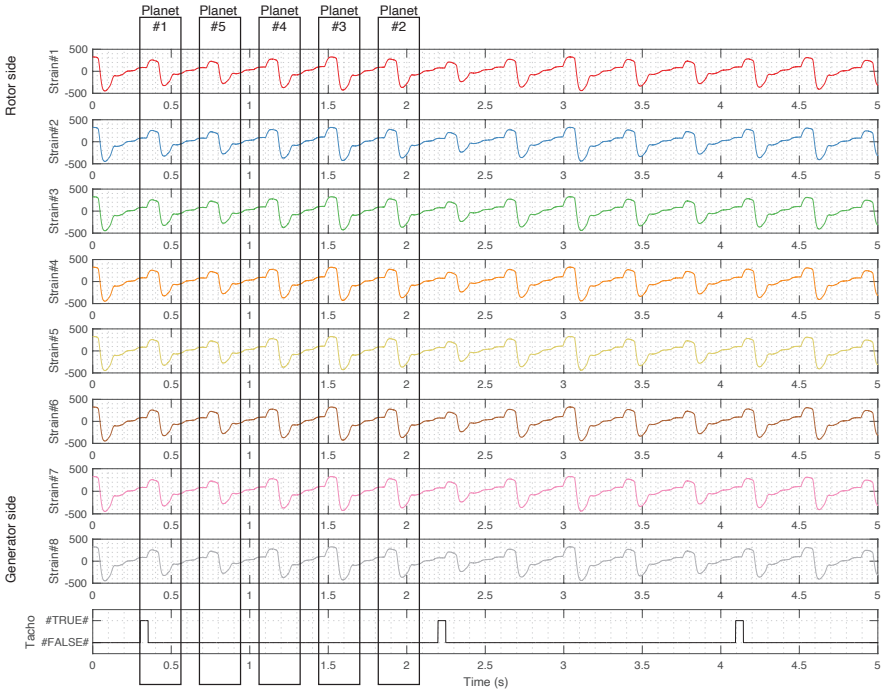

Figure 5.4: Strain signals of all 8 root gauges and once-per-revolution tachometer.

for a given revolution *rev* of the sun relative to the carrier the following mesh intensities can be computed: $i_{1,rev}, i_{2,rev}, i_{3,rev}, ..., i_{P,rev}$.

A mesh load factor for a single revolution can be evaluated by comparing all the mesh intensity values of a single revolution and dividing the maximum mesh intensity from a single planet by the average of all planets, see Eq. (5.2). Since dynamic effects can influence the different mesh intensity values during a complete revolution, this value has been denoted as $K_v K_{\gamma rev}$:

$$K_v K_{\gamma rev} = \frac{max(i_{1,rev}, i_{2,rev}, i_{3,rev}, ..., i_{P,rev})}{\frac{\sum_{p=1}^{P} i_{p,rev}}{P}}. \tag{5.2}$$

The term $K_v K_\gamma$ is a loose interpretation of the standard ISO 6336 [58]. A method to measure the dynamic effects covered by K_v is unavailable in the industry. The authors understand that the dynamic effects influence the mesh intensity measurements within a revolution because the mesh events were measured at different time instants. However, it cannot be guaranteed that all the dynamic effects will show in the few mesh events recorded by the instrumented tooth.

In the present study, the tooth root strains were recorded for tests performed with

33 %, 50 %, 67 %, 83 %, and 100 % of the nominal torque. During each test, the reference torque command was kept stationary. Around 20 revolutions of the sun relative to the carrier were recorded for each test. Throughout these revolutions, the strain distribution was observed to change dynamically. The $K_v K_\gamma$ values were computed for all the recorded revolutions. The average $K_v K_\gamma$ and the worst case or maximum $K_v K_\gamma$ were selected. A third value relative to the mesh load factor was explored. The peak-to-peak strain data of each strain gauge was averaged, taking into account the planet that produced the gear mesh. This average distribution filters out the contributions of K_v assuming that the dynamic effects covered by the factor K_v are uncorrelated with the mesh load factor K_γ and that the recorded data covers enough revolutions. This average mesh load factor has been denoted as $K_{\gamma,avg}$:

$$K_{\gamma,avg} = \frac{max(i_{1,avg}, i_{2,avg}, i_{3,avg}, ..., i_{p,avg})}{\frac{\sum_{p=1}^{P} i_{p,avg}}{P}}, \tag{5.3}$$

where the i_{pavg} is the average mesh intensity produced by the planet p which be computed using the following equation:

$$i_{p,avg} = \frac{\sum_{r=1}^{R} i_{p,r}}{R}. \tag{5.4}$$

Figure 5.6 shows the average K_γ, average $K_v K_\gamma$ and maximum $K_v K_\gamma$ results of both instrumented roots (roots number 1 and 13) obtained during the tests performed with stationary torque values of 33 %, 50 %, 67 %, 83 %, and 100 % of the nominal torque.

5.2.2 Load mesh factor from ring gear outer surface instrumentation

A new method to measure the input torque of wind turbine gearboxes was introduced in [65]. This method is based on strain measurements on the outer surface of the ring gear. The instrumentation requirements and the data logging process are simplified because the ring gear is static. Optical strain sensors based on fiber Bragg gratings (FBGs) were used because they offer a higher signal-to-noise ratio and are immune to electromagnetic interference. Since multiple strain sensors can be accommodated in a single fiber, they also allow a more straightforward installation. A satisfactory correlation was found between the input torque of the carrier and the deformations on the outer surface. Furthermore, the procedure based on peak-to-peak strain values provided information about the load sharing between planets.

Four optical fibers were installed on the outer surface of the first stage ring gear, at the middle section along the width of the ring gear in the axial direction, as shown in Figure 5.1. The fibers were installed tangentially to the middle section, covering a complete revolution along the outer perimeter of the ring gear. Figure 5.7 shows the radial and angular location of all the strain sensors with the corresponding labels in a rotor side section view. The four different colors of the sensor labels indicate how the FBGs belong to separate fibers (S01 to S15 in fiber number 1, S16 to S28 in fiber number 2, S29 to S41 in fiber number 3, and S42 to S54 in fiber number 4). The fiber optical sensors were supplied and installed by the company Sensing360 B.V. [80]. A more comprehensive description of the optical fiber instrumentation used can be found in [65].

Fiber Bragg gratings are sensitive to strain and temperature. The signals were detrended to remove the effect of temperature on the measured shifts in wavelengths of the FBGs. Once the long-term shift caused by temperature had been removed, the remaining signal was considered to be caused entirely by the strain imposed from the planet gear mesh events. A correlation between the average torque and the average peak-to-peak values of the strain sensors placed on the ring gear's outer surface was found in [65]. An inductive sensor was used to provide a pulse for every full rotation of the input shaft so that the relative position of the planet carrier is known and peak-to-peak values can be assigned to individual planets as shown in Figure 5.8. For every revolution of the carrier, a value of $K_v K_\gamma$ can be computed using the peak-to-peak values as i_{mesh} from Eq. (5.1). Similarly, the following expression is proposed to derive the average $K_{\gamma,p}$ of a particular planet:

$$K_{\gamma,p} = \frac{\overline{\Delta\delta}_p}{\overline{\Delta\delta_{all}}}, \tag{5.5}$$

where $\overline{\Delta\delta}_p$ is the average peak-to-peak strain value measured from all mesh events caused by a particular planet p, and $\overline{\Delta\delta_{all}}$ is the average peak-to-peak value of all planets. In the instrumentation set-up used for this study, the number of strain sensors on the ring gear is not an integer multiple of the number of planets, therefore, it is not possible to compare strain peaks in different positions simultaneously. Figure 5.9 shows the resulting average K_γ for each strain sensor position for a test conducted at 100 % of torque.

Short tests under 19 different stationary speed and torque conditions were performed to characterize the relationship between torque and the mesh load factor. The torque level was increased in five percent increments from 10 % to 100 % of the nominal torque. For each test, strain data was recorded for around 35 revolutions of the carrier. The gearbox rotational speed was kept constant and equal to the nominal value. Figure 5.10 shows the average K_γ values of the five planets against torque. The values shown by the circular markers in Figure 5.10 represent the mean value of all 54 sensors, and the shaded patches represent the bounds limited by the minimum and maximum K_γ.

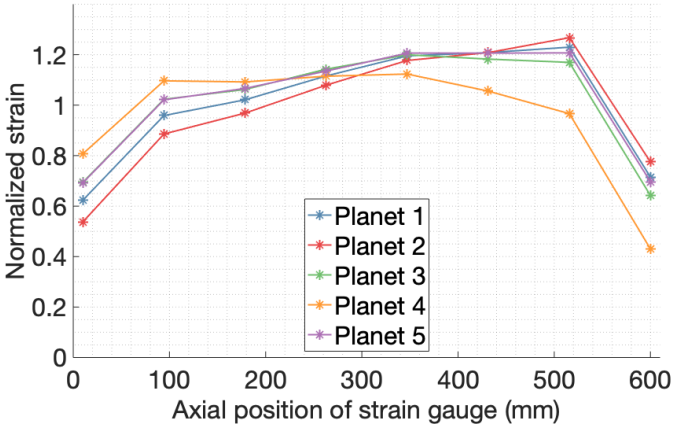

Figure 5.5: Root strain distribution for the mesh events of a single revolution of the sun relative to the carrier.

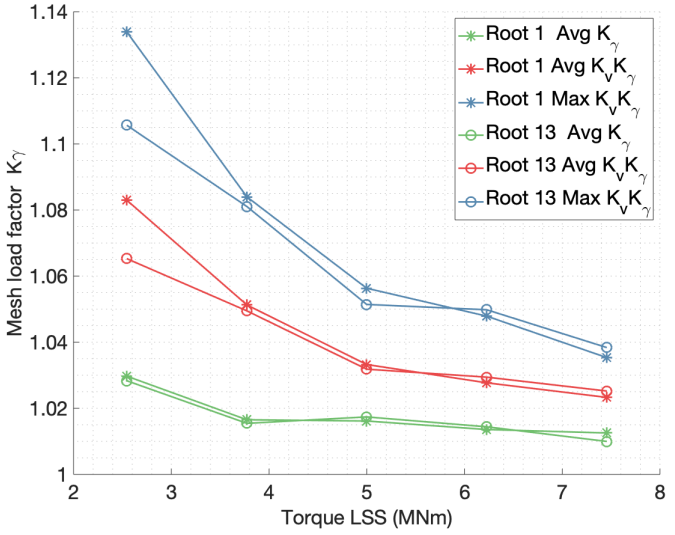

Figure 5.6: Mesh load factors obtained from strain measurements in two roots of the sun gear.

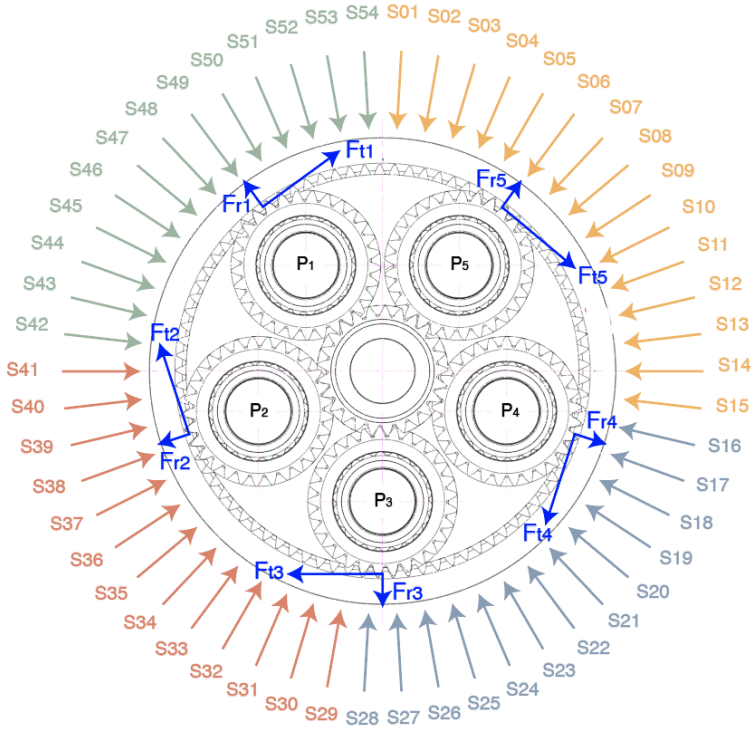

Figure 5.7: Location of the fiber optical strain sensors (S01 to S54).

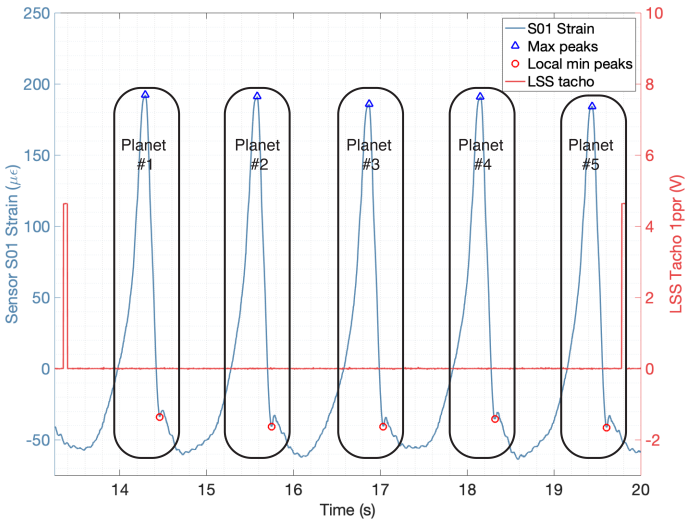

Figure 5.8: Sensor S01 Strain signal (left axis) during a single revolution of the input shaft (right axis) with detected peaks assigned to the corresponding planet.

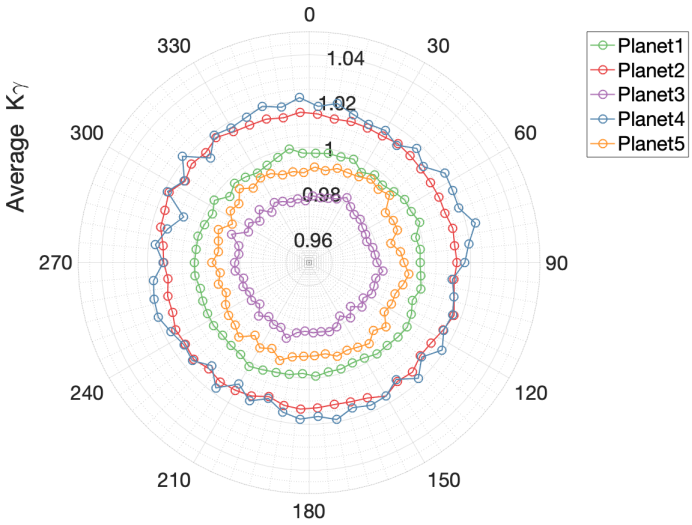

Figure 5.9: Average K_γ per planet for each sensor evaluated at 100 % nominal torque.

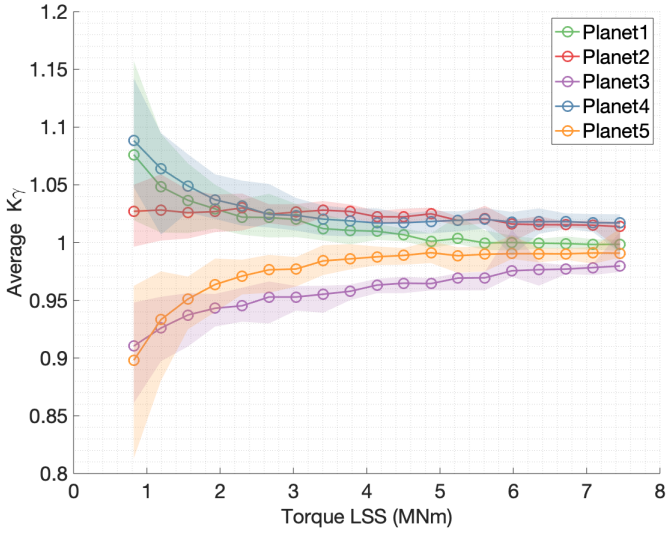

Figure 5.10: $K_{\gamma,avg}$ values from all fiber strain sensors, the mean value is represented by the circular marker and the min-max bounds by the shaded patch.

5.3 Discussion of results

This section will discuss the main findings gathered through the experimental evaluation of the mesh load factor K_γ of the first planetary stage from a modern 6MW wind turbine gearbox. Two alternative approaches have been studied. First, the traditional method based on gear tooth root strain measurements has been described in Section 5.2.1. Then a different approach based on strain measurements on the outer ring gear using fiber-optic sensors has been presented in Section 5.2.2. The results from both experimental approaches have been combined in Figure 5.11. The comparison has been made for the three mesh load factors defined in Section 5.2, i.e., average $K_v K_\gamma$, maximum $K_v K_\gamma$ and average K_γ. In the case of the fiber-optic strain sensors the triangular marker represents the mean value of all sensors and the shaded patch the minimum to maximum bounds. As it can be seen, both approaches yield similar results and a good fit has been found between the different K_γ values obtained.

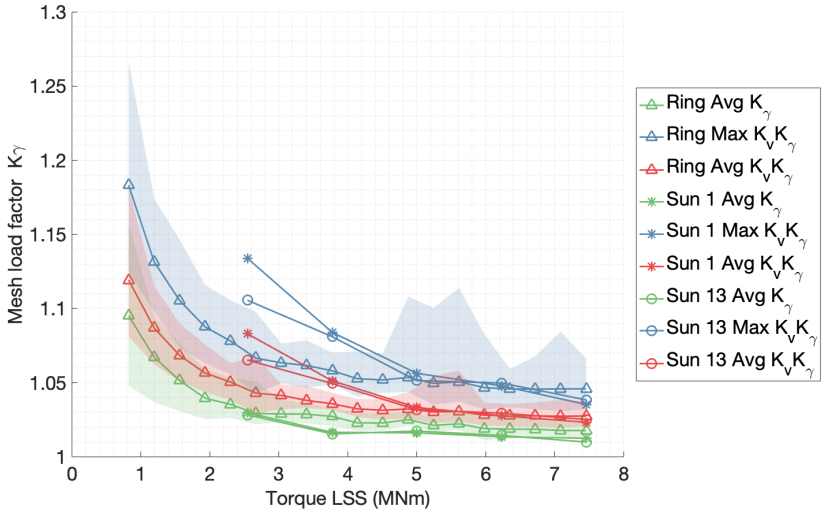

Figure 5.11: Average K_γ, maximum $K_v K_\gamma$ and average $K_v K_\gamma$ values evaluated from tooth root strain measurements at the sun gear, denoted as Sun1 and Sun13, compared with values evaluated from strain sensors on the ring, denoted as Ring.

It is worth noticing that results from the gear tooth root instrumentation were produced for test conditions with 33 %, 50 %, 67 %, 83 %, and 100 % of the nominal torque. On the other hand, using the strain sensors on the outer surface of the ring gear, the mesh load factor could be evaluated for 19 short tests from 10 % to 100 % of the nominal torque in 5 % increments. This is because measuring in the static frame overcomes the main drawbacks of data transfer from rotating components and makes data gathering less time-consuming. Therefore more test conditions could be performed in a shorter time.

Both measurement approaches show an improvement of the mesh load factor with torque. This is expected because of the flexibility of the gearbox components. As torque

increases, the deformation of these components increases, reducing the influence of manufacturing errors and better load sharing is achieved. The fit between the two approaches is best from 66 % to 100 % of the nominal torque. The sun gear results seem to be more sensitive to torque for lower torque values and show a larger increase when torque is reduced. However, the torque region below 33 % was not recorded with the sun gear instrumentation, and a direct comparison was not possible for such low torque levels. Low torque levels are not critical for gear rating and life expectations, and therefore having high mesh load factors at lower torque values is not a concern for gearbox manufacturers.

The experimental mesh load factor K_γ results for the nominal working condition of the gearbox are significantly lower than the default values required by the standard IEC 61400-4 [59] shown in Table 5.1. Care must be taken when interpreting these results because the results presented in this study come from a single instrumented gearbox. Therefore, the manufacturing class and accuracy of the serial production gearbox components shall be controlled so that the behavior of the prototype is representative of the complete fleet. Moreover, with the instrumentation set-up presented in this study, an instantaneous mesh load factor could not be evaluated. The average mesh load factor seems appropriate for gear rating and life calculations, but the instantaneous behavior of load-sharing between planets remains to be researched.

5.4 Conclusions

The present study has shown that the fiber optical strain measurements in the outer surface of the ring gear yield equivalent mesh load factor K_γ results compared to the traditional method based on strain gauges located in the roots of the sun gear teeth. This is a promising result because transferring the resulting signal from the rotating sun and powering the data acquisition devices is difficult and costly. Measuring in the static ring gear overcomes these drawbacks allowing a more straightforward installation and easing the data recording requirements for testing.

The experimental mesh load factor K_γ results obtained for a modern 6MW wind turbine gearbox with five planets in the first stage are significantly lower than the default values required by the standard IEC 61400-4 [59]. Since K_γ is directly used for gear rating and life calculations, a low value of K_γ allows for a more optimized gearbox design, and therefore significant improvements in torque density are expected. The manufacturing class of the gears and the accuracy of the serial production gearbox components have to be controlled to extrapolate the results obtained from a single prototype to the entire fleet.

For future work, researching the instantaneous load-sharing behavior between planets is suggested. The placement of the strain sensors used in the instrumentation set-up of this study does not allow evaluating simultaneous mesh events. However, the authors believe this could be overcome with improved sensor placement.

6

Instantaneous mesh load factor (K_γ) measurements in a wind turbine gearbox using fiber-optic strain sensors

The mesh load factor, K_γ, describes how loads are shared between planet gears and has become one of the key design challenges in modern wind turbine gearboxes. Planet load sharing directly impacts tooth root stresses, a critical driver of torque density and gearbox reliability. Experimental evaluation of K_γ is typically performed from sun gear tooth root strain gauge measurements, which are complex. Furthermore, such measurements can only provide an average value of load sharing. The present study describes an alternative method to evaluate the mesh load factor in wind turbine gearboxes based on fiber-optic strain sensors installed on the outer surface of the fixed ring gear. We present the results of an extensive measurement campaign to evaluate this novel sensing solution installed on the input planetary stage of a 2-MW wind turbine gearbox at the National Renewable Energy Laboratory's Flatirons Campus (Colorado, USA). The number of strain sensors on the ring gear was selected as an integer multiple of the number of planets, which has enabled an instantaneous evaluation of the mesh load factor. The effect of operating conditions on the planet load-sharing behavior of the gearbox has been investigated. The mesh load factor measured for operating conditions close to rated was below 1.05, well below IEC 61400-4 standard requirements.

6

This chapter is based on the following publication: *U. Gutierrez Santiago. Instantaneous mesh load factor (K_γ) measurements in a wind turbine gearbox using fiber-optic strain sensors* [102]. Orange is the sixth color of the rainbow when arranged by increasing wavelength. Orange has a wavelength between 590 nm and 620 nm. Data visualization plays an essential role in scientific research and dissemination. Rainbow colormaps, which follow the sequence of colors in the visible light spectrum, have been widely used in scientific publications. However, the rainbow colormap, also known as "jet," is misleading because the human eye perceives a stronger contrast in the yellow-orange-red part of the spectrum compared to the blue-green part. When arranged by the wavelength of individual colors, the rainbow color sequence appears highly unequal. Additionally, it is unreadable for people with most forms of color blindness and when printed in black and white. It is estimated that 4.5 % of the population cannot see the entire visible spectrum. A perceptual colormap ensures that equal data intervals correspond to the same perceived color difference across all parts of the spectrum. Plots in the articles presented in Chapters 2, 5 and 6 were generated using the Matalb function *linespecer.m* created by by Jonathan C. Lansey based on the research of Cynthia Brewer (`http://colorbrewer2.org/`) [109]. For the articles presented in Chapters 3 and 4, the open-access scientific color maps package `https://doi.org/10.5281/zenodo.1243862`) by Fabio Crameri [110]was used.

6.1 Introduction

The push to lower the levelized cost of energy from wind has resulted in a race to increase the rotor diameter, power rating, and hub height of wind turbines [9]. The increased rated power and rotor diameters have significantly increased the rotor torque. This has translated into higher torque density demands for all drivetrain components and notably for the gearbox. Thanks to multiple technological innovations, torque densities of 200 $\mathrm{N\,m\,kg^{-1}}$ are now available [37–39]. For such high torque ratings, a trend has emerged in gearbox architecture to increase the number of planetary stages and the number of planets per stage [65]. The main challenge of such gearbox designs is sharing the load evenly between the planets, especially when subjected to rotor nontorque loads and in the presence of any manufacturing errors [54]. The gear rating standard ISO 6336-1 [58] defines the mesh load factor, K_γ, as the quotient between the highest load carried by a single planet divided by the average load of all planets. Within the design requirements for wind turbine gearboxes, the standard IEC 61400–4 [59] sets K_γ as a function of the number of planets. For a large number of planets, the specified mesh load factors are conservative and would lead to gearbox designs with poor torque density. The standard allows using lower mesh load factors if they are experimentally demonstrated by gear tooth root strain gauge measurements. However, such measurements are very complex and costly and only provide an average measurement of the mesh load factor because the mesh intensity can only be assessed when an instrumented sun tooth meshes with the different planets. Because those gear meshes occur at different times, the mesh load factor has to be averaged over multiple revolutions of the sun gear relative to the carrier, assuming that the loading conditions remain constant during the averaging period. In [108], the authors presented an alternative approach based on strain measurements on the outer surface of the static ring gear. Because the ring gear is static, the system's complexity is greatly reduced and has the potential to be implemented on serial production gearboxes throughout their operational life instead of being limited to prototype verification purposes. Both methods yielded equivalent average mesh load factor results under stationary conditions. However, that study was performed on a back-to-back test bench under torque-only loading and stationary conditions. The number and placement of the strain sensors used did not allow the evaluation of simultaneous mesh events because they were not an integer multiple of the number of planets.

Planet load sharing directly impacts tooth root stresses, which are a critical driver of torque density and gearbox reliability. The ability to instantaneously measure the mesh load factor is important to verify design assumptions. Gear fatigue life calculations in gear rating standards assume a constant mesh load factor; measuring the mesh load factor instantaneously will verify the design assumptions for different operating conditions. The contribution of this chapter is twofold: (1) We demonstrate that fiber-optic strain sensors with improved sensor placement can provide instantaneous measurements of the mesh load factor, and (2) we present the results of an extensive measurement campaign on a 2-MW wind turbine with nonstationary operating conditions and complex rotor loading.

The remainder of this chapter is organized as follows: Section 6.2 describes the sensors and data acquisition equipment used for the experiment; Section 6.3 describes the methodology used to extract the instantaneous mesh load from fiber-optic strain measurements on the outer surface of the ring gear; Section 6.4 discusses the results obtained during the

field measurement campaign; and finally, Section 6.5 draws the main conclusions of this work and suggests recommendations for future work.

6.2 Experimental setup

The present study was conducted on a Gamesa G97 2-MW wind turbine, shown in Figure 6.1, located at the National Renewable Energy Laboratory's (NREL's) Flatirons Campus (Colorado, USA). This turbine has a four-point mount drivetrain, and the gearbox planetary stage comprises three planets. During the test campaign, data were collected from four different sources: (1) the fiber-optic strain sensors installed on the outer surface of the ring gear; (2) main shaft instrumentation comprising strain gauges and an angular encoder installed to measure torque, bending, and rotor azimuth angle; (3) NREL's meteorological tower to measure ambient temperature, wind speed, and wind direction at hub height; and (4) turbine controller for wind turbine operational parameters.

6.2.1 Fiber-optic sensors

An array of 24 fiber-optic strain sensors were installed around the outer surface of the ring gear of the gearbox, which has a single planetary stage. The sensing principle was based on fiber Bragg gratings (FBGs). FBGs are modifications to the fiber's core in discrete, short segments that reflect particular wavelengths of light and transmit all others. FBGs are suitable for sensing applications because the reflected wavelength is sensitive to temperature and strain changes at the grating. FBGs offer a higher signal-to-noise ratio than traditional strain gauges based on their electrical resistance change. They are immune to electromagnetic interference, and a single optical fiber can accommodate multiple sensors, simplifying the installation process. In the present study, two optical fibers, each with 12 FBGs, were bonded with cyanoacrylate glue on the outer surface of the ring gear at the midpoint of the tooth width, as shown in Figure 6.2.

The 24 fiber-optic sensors were chosen as a multiple of the three planets. The sensors were equally spaced around the perimeter to ensure that the mesh events caused by the three planets could be detected simultaneously. Figure 6.3 shows a rotor side view of the middle section of the ring gear with the angular location of the strain sensors. In operation, the mesh forces between the planets and ring gear teeth cause deformations of the ring gear proportionate to the rotor torque. The main element of the data acquisition system is a fiber interrogator that sends light into the fiber and analyzes the wavelengths reflected by the gratings. The interrogator extracts a signal from each grating to measure strain and temperature. The interrogator used for the measurement campaign provided a sampling frequency of 2000 Hz for each signal. Sensing360 B.V. supplied the fiber optic sensors.

6.2.2 Main shaft sensors

The second set of sensors was installed in the main shaft. An angular displacement encoder measured absolute azimuth angle to relate the strains measured in the static ring gear to an angular position of the main shaft and rotor. A zero-degree azimuth angle was set with a blade labeled as "A" down. In the main shaft, three full Wheatstone bridges measured torque and the two orthogonal bending moments. All sensors installed in the main shaft were logged at a sampling rate of 60 Hz.

Figure 6.1: G97 2-MW wind turbine on NREL's Flatirons Campus. Photo from Dennis Schroeder, NREL 21886.

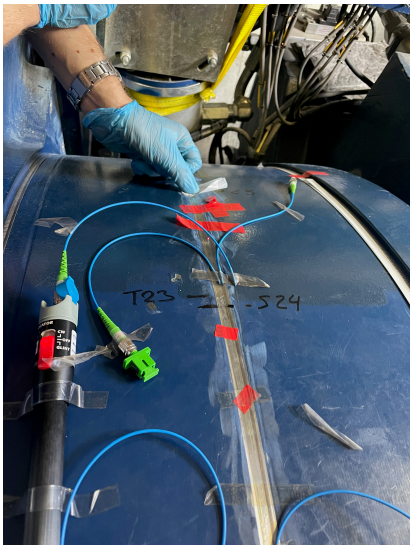

Figure 6.2: FBG installation. Photo from Unai Gutierrez-Santiago, Siemens Gamesa Renewable Energy, NREL 85910.

6.2.3 Meteorological data

The inflow wind conditions were gathered from the NREL Flatirons Campus M4/site 4.4 meteorological tower. Wind speed, wind direction, and temperature measurements at hub height were logged at a sampling rate of 60 Hz.

6.2.4 Turbine operation parameters

The last data source was the turbine controller. Using a proprietary data acquisition system supplied by Siemens Gamesa, several operational parameters were logged with a sampling frequency of 25 Hz. These operational parameters included the wind speed measured by the turbine, nacelle direction, total power produced, generator and rotor speed, gearbox oil sump and high-speed shaft bearing temperature, nacelle and exterior temperature, pitch angles, and pitch angle rates.

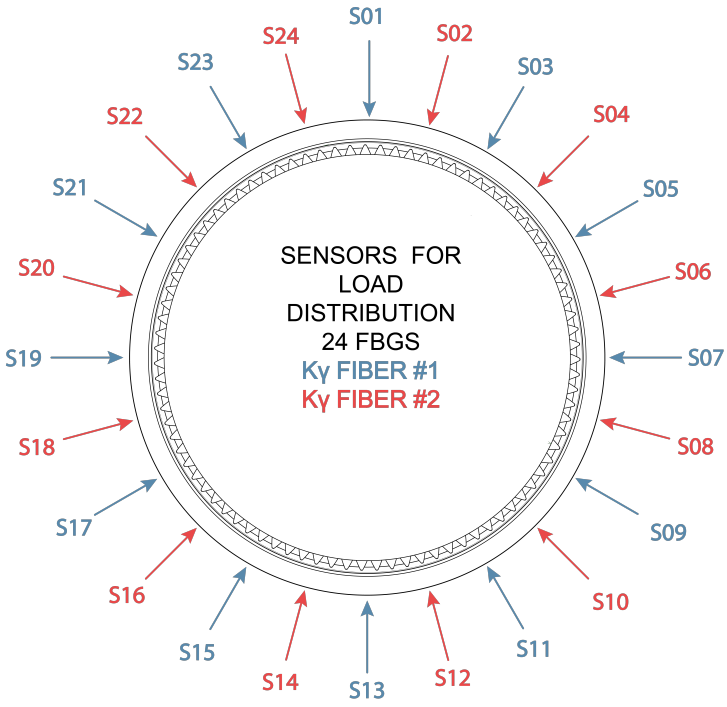

Figure 6.3: Angular placement of the 24 FBGs on the outer surface of the first-stage ring gear.

6.3 Evaluation of the load mesh factor from ring gear outer surface strain

The standard IEC 61400–4 [59] sets the design requirements for wind turbine gearboxes and specifies the mesh load factor K_γ as a function of the number of planets. The standard allows using lower mesh load factors if they are experimentally demonstrated by gear tooth root strain gauge measurements. Examples of practical implementations of such measurement systems can be found in [60] and [61]. Strain gauges must be placed in a root of the rotating sun gear to extract planet load-sharing behavior, which requires either a slip ring or telemetry system with appreciable planning and installation costs. Each time the instrumented sun tooth engages with a planet, the mesh forces can be evaluated, assuming they are proportional to a weighted sum of all the strains measured along the root. The instrumented tooth will mesh with all the planets because the sun rotates faster than the carrier. However, the mesh events do not coincide in time. Therefore, the effect of the dynamic factor, K_v, and torque fluctuations must be addressed, and only an average value of the mesh load factor over multiple revolutions of the sun gear relative to the carrier can be obtained. A more elaborate way of evaluating the mesh load factor has

been used to overcome this limitation [54]; however, this method is very complex and requires modifications to the gearbox and planet bearings. Using fiber-optic strain sensors, strain measurements on the ring gear's outer surface were proven to provide equivalent load-sharing results [108]. These results were obtained in a back-to-back test bench under stationary torque loads. Because the ring gear is stationary, there is no need for wireless data transfer, and the power supply is also simplified compared to when the instrumentation is on the rotating sun. However, with the sensor configuration used in [108], it was only possible to assess the average mesh load factor due to the chosen sensor spacing. For this study, a new sensor configuration, shown in Figure 6.3 and described in Section 6.2, was designed to evaluate the instantaneous planet load sharing.

For the G97 drivetrain, the rotor torque is transmitted directly by the main shaft to the planet carrier of the gearbox, which is then distributed by the carrier to the three planets. When the planets mesh with the ring gear, the mesh force causes the ring gear to deform, and this deformation is measured by the fiber-optic strain sensors placed on the ring gear's outer surface as a tensile-compressive cycle. FBGs are sensitive to changes in strain and temperature. However, temperature changes occur at a much lower pace than strain changes caused by gear mesh events. A moving average filter was used to detrend the raw FBG signals, and we assumed that once the long-term shift caused by temperature had been removed, the remaining signal was entirely caused by the strain imposed by the planet gear mesh events. The relationship between torque and the peak-to-peak values of the tensile-compressive strain cycle were described in [65]. Using the absolute rotor azimuth signal, the relative position of the planet carrier is known, and peak-to-peak values can be assigned to individual planets. Figure 6.4 shows the strain measured at sensor S01 and the azimuth angle. Arbitrarily, for each full rotation of the rotor, the first planet to cause a deformation in sensor S01 was identified as planet one (P1). During normal operation, the carrier rotates clockwise, downwind, and subsequent planets were labeled two (P2) and three (P3). For each sensor, the maxima and minima peaks of every revolution are detected and assigned to each planet, denoting the peak-to-peak strain as $\Delta\epsilon_{n,p}$, where n is the revolution number, and p is the planet number. For clarity, only the first revolution is shown in Figure 6.4. An average K_γ value can be computed for each sensor using the following equation, $\Delta\epsilon$

$$K_{\gamma,p} = \frac{\overline{\Delta\epsilon}_p}{\overline{\Delta\epsilon}_{all}}, \tag{6.1}$$

where $\overline{\Delta\epsilon}_p$ is the average peak-to-peak strain value measured from all mesh events assigned to a single planet, and $\overline{\Delta\epsilon}_{all}$ is the average peak-to-peak value of all planets. That is,

$$\overline{\Delta\epsilon}_p = \frac{1}{n}\sum_{i=1}^{n}\Delta\epsilon_{i,p} = \frac{\Delta\epsilon_{1,p} + \Delta\epsilon_{2,p} + \cdots + \Delta\epsilon_{n,p}}{n}. \tag{6.2}$$

In the instrumentation setup used for this study, the number of strain sensors on the ring gear was selected as an integer multiple of the number of planets. Therefore, when a planet is meshing near a strain sensor, the other two planets are also close to other strain

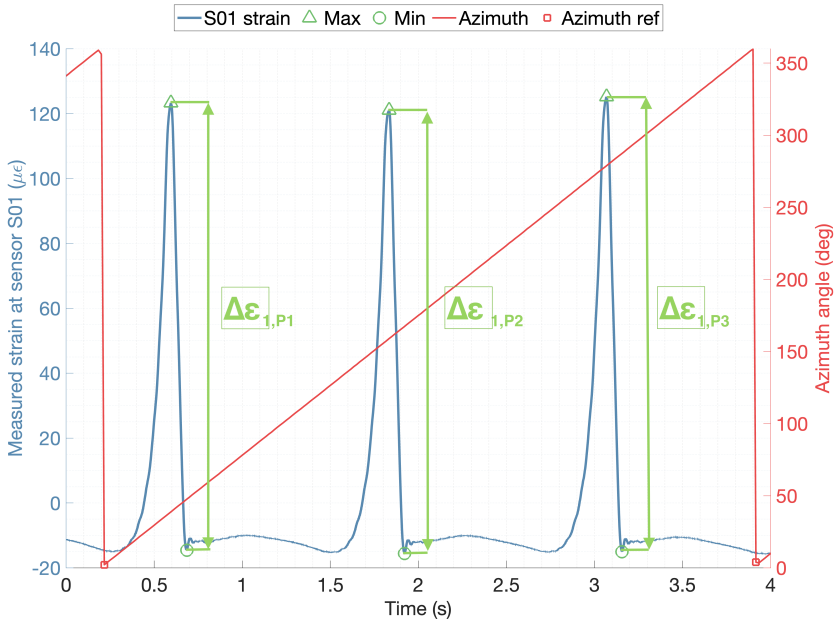

Figure 6.4: Peak-to-peak strain from sensor S01 assigned to P1, P2, and P3 for one full rotation.

sensors, and it is possible to compare their strain peaks simultaneously. Since we have 24 sensors and three planets, there are eight possible sensor combinations with synchronous mesh events. Figure 6.5 shows one of the combinations with strain sensors S01, S09 and S17. The strains measured at each sensor location are different in magnitude. This was also observed when estimating the torque from the peak-to-peak values in [65]. A normalization of the individual peaks is proposed to compare the strain of the simultaneous sensors. The peak-to-peak values are, therefore, normalized with the ratio between the average of all sensors and the mean peak-to-peak from each sensor. Figure 6.5 shows the first simultaneous mesh event recorded at sensors S01, S09, and S17 after the azimuth angle passed zero degrees. In this case, P1 meshes close to sensor S01, P2 is close to S17, and P3 is close to S09. Once the weighted peak-to-peak values have been assigned to the planet that caused the deformation, it is possible to compute an instantaneous K_γ for the time when the mesh was recorded. Figure 6 shows the torque and instantaneous K_γ value, constructed by repeating the same procedure for all eight sensor combinations with 24 values per rotor revolution, over an example 1 minute of turbine operation at 23:40 UTC on May 30. The torque ranges from 50 % to near rated. The instantaneous load-sharing ranges from 0.97 to 1.03, but the average load-sharing for each planet is much closer to 1.0.

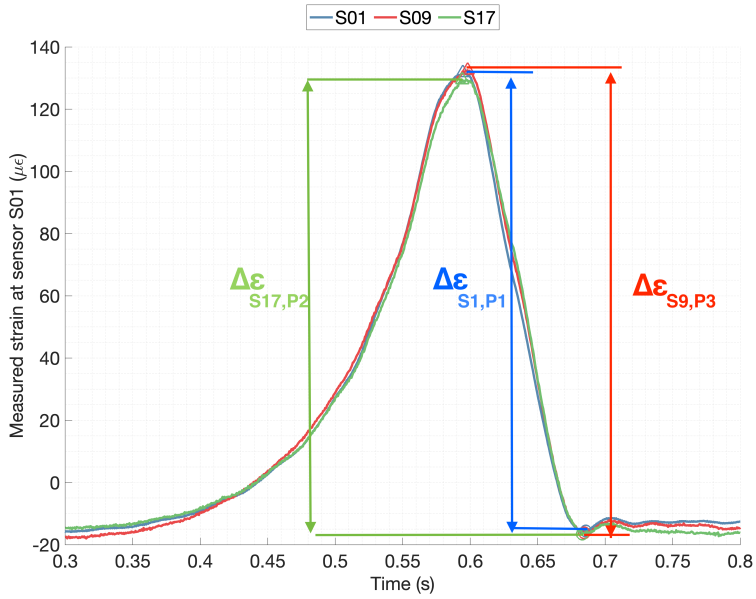

Figure 6.5: Strain of sensors S01, S09, and S17, zoom first peak, assignment of planets.

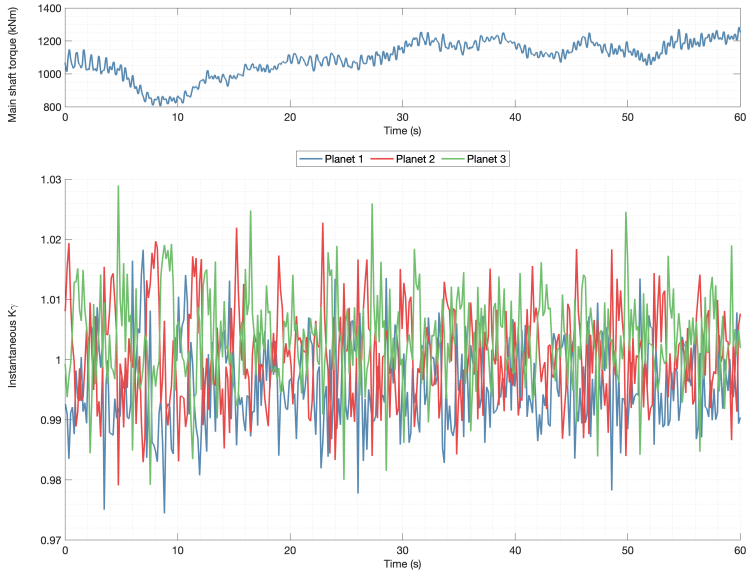

Figure 6.6: Evolution of torque and the mesh load factor with time (May 30 at 23:40 UTC).

6.4 Field validation campaign

An extensive measurement campaign was conducted on the G97 2-MW wind turbine shown in Figure 6.1. The measurement and data acquisition equipment described in Section 6.2 were active from April 25 to July 31, 2023. During this period, the turbine was run under normal working conditions using the standard controller parameters. Data were continuously logged during operation using the specified sampling frequencies of each data source. The acquired data were binned into 10-minute files for ease of handling and analysis. Figure 6.7 shows a scatterplot constructed using the average wind speed against the total produced power for all the 10-minute recordings gathered during the test campaign. A wide range of operating conditions were covered and were considered representative of the complete power curve of the turbine. Only data containing produced power measurements above 150 kW were analyzed to evaluate the instantaneous mesh load factor. In total, 1644 10-minute files were recorded with a minimum of 150 kW, and 238 of these files had torque values above 50 % of rated. As shown in Figure 6.6, the mesh load factor exhibits small fluctuations around a mean value. The effect of different normal power production operating conditions on the planet load-sharing behavior was analyzed by averaging the instantaneous K_γ values within the 10-minute recordings. From all the turbine operation parameters, torque was found to have the largest effect on the mesh load factor. Other turbine variables investigated included wind speed, wind turbulence intensity, wind direction, yaw misalignment, blade pitch angles, and temperatures such as ambient, nacelle, ring gear, and gearbox oil sump. The relationship between torque and mesh load factor is shown in Figure 6.8, where each dot represents the average value for a full revolution. As can be observed, all recorded values are very low, lower than 1.05 around the rated operation, and increase slightly for lower torques. This is expected because the effect of small manufacturing errors tends to be absorbed by the carrier's flexibility for higher torques. Furthermore, having a higher mesh load factor for such low torques is not critical for gear stresses. The effect of other operating variables like wind turbulence intensity and yaw misalignment was also investigated and found to be very low. These findings align with the gearbox's expected performance due to the drivetrain configuration and number of planets. The G97 wind turbine uses a four-point mount drivetrain, in which the overwhelming majority of nontorque loads are supported by the two main bearings, and the gearbox planetary stage comprises three planets and a floating sun, which minimizes the effect of any manufacturing errors. In Figure 6.8 the mean mesh load factor behavior is shown and found to align with each planet's intrinsic manufacturing properties. As shown in Figure 6.6, the mesh load factor exhibits a dynamic behavior. To quantify the deviation from the mean, Figure 6.9 shows the maximum mesh load factors recorded during full revolutions of the rotor. The difference between the maximum and average values is low for the planet with the highest mesh load factor, which validates the design assumptions used for gear rating and fatigue life calculations.

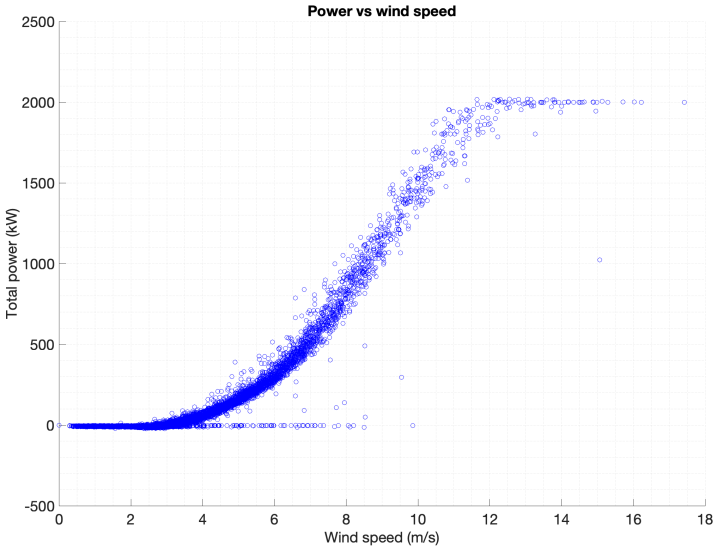

Figure 6.7: 10-minute average wind speed vs. total power produced by the turbine.

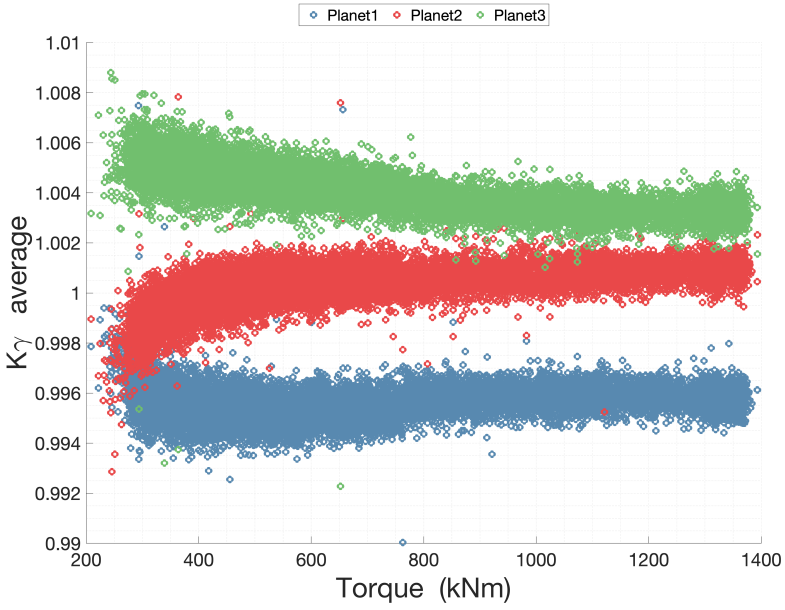

Figure 6.8: Average mesh load factor recorded during a full rotor revolution against rotor torque.

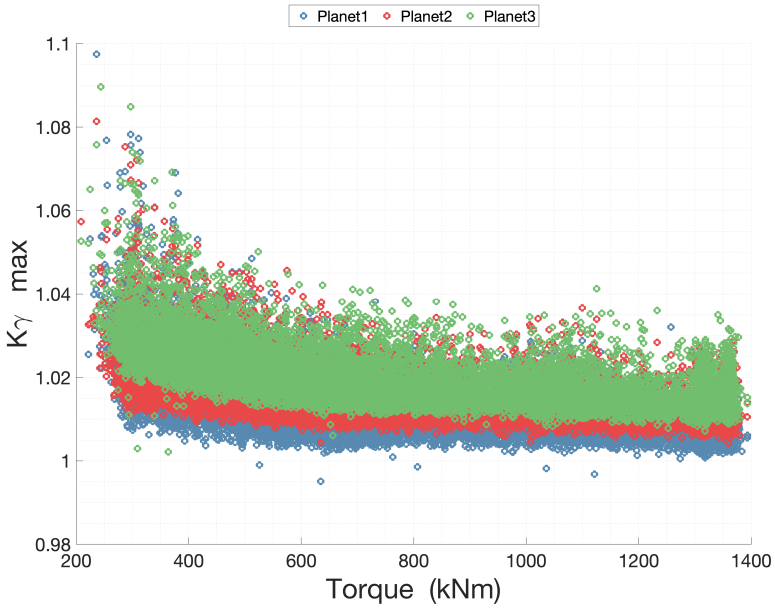

Figure 6.9: Maximum mesh load factor recorded during a full rotor revolution against rotor torque.

6.5 Conclusions

We have presented the results of an extensive field measurement campaign conducted on a 2-MW wind turbine gearbox. The results show that with an improved spacing definition, fiber-optic strain sensors placed on the outer surface of the static ring gear can provide a means to instantaneously evaluate the planetary mesh load factor. Accurate knowledge of planet load sharing is paramount to increasing torque density in new gearbox designs while ensuring high reliability. The instantaneous mesh load factor has been evaluated for a wide range of operating conditions over more than three months of normal operation, covering the complete power curve of the turbine. For operating conditions close to rated, the maximum mesh load factor was found to be below 1.05. This value is below the requirement of 1.10 from the IEC 61400–4 for three planets when no experimental data are available, which enables increasing the torque density of the gearbox. An increase in the mesh load factor was observed for lower torques, which is also to be expected but is not critical because tooth root and contact stresses are lower when torque decreases. The effects of other operating variables like wind turbulence intensity and yaw misalignment on the mesh load factor were found to be negligible, which is aligned with the expected behavior of the four-point mount drivetrain configuration under test. For future work, it is suggested that an analytical model of planet load sharing could be developed and correlated with the measurements presented in this chapter. Additionally, the potential usage of the presented instantaneous load mesh factor measurements for gearbox condition monitoring should be investigated.

7

Conclusion and recommendations

The primary objective of this dissertation was formulated in Chapter 1 as to "Develop a method to measure dynamic mechanical torque in geared wind turbines". A key requirement was set to enable fleet-wide implementation to monitor torque throughout the complete service life of the wind turbines. This dissertation has proposed a method based on strain measurements on the outer surface of the static first-stage ring gear that overcomes the main drawback of traditional methods. A series of experiments have been presented, ranging from proof-of-concept tests conducted using gearbox test benches to an extensive field validation campaign. These experiments have advanced the technology readiness level and demonstrated the accuracy and robustness of the proposed method, which is now deemed ready for commercial implementation. Future work should explore the potential to improve drivetrain loading using dynamic mechanical torque measurements with novel data-driven control strategies. Additionally, recursively tracking operational deflection shapes over time is proposed for fault detection, and its effectiveness in identifying faults in planetary components should be explored.

7

Each of Chapters 2 to 6 are concluded with a section summarizing the findings and recommendations for the research questions addressed in that chapter. This chapter reiterates these findings and formulates the overarching conclusions of the dissertation, together with recommendations for future research. Red is the seventh color of the rainbow when arranged by increasing wavelength. Red has a wavelength between 620 nm and 750 nm. Johann Wolfgang von Goethe (1749 – 1832) challenged Newton's views on color, arguing that color is a subjective experience perceived differently by each viewer. His work *Theory of Colours* was the first systematic study on the physiological effects of color. Color can dramatically affect moods, feelings, and emotions. Warm colors with high wavelengths, such as red, orange, and yellow, evoke emotions ranging from warmth and comfort to anger and hostility. In contrast, cool colors with lower wavelengths, like green, blue, and purple, are often associated with calmness but can also evoke feelings of sadness or indifference. Lighting conditions, including the intensity and color of light, significantly influence human biological cycles by affecting hormonal secretions like melatonin. Low light levels at night stimulate melatonin production, promoting sleep. Conversely, excessive lighting or sudden light flashes can cause discomfort, stress, and disorientation, potentially leading to neuropsychiatric disorders. Humans are inherently photosensitive beings, deeply affected by the colors and light around us.

7.1 Conclusions and recommendations

This dissertation has successfully developed a novel method to measure dynamic mechanical torque in geared wind turbines from proof-of-concept tests using gearbox test benches to an extensive field validation campaign. These experiments have advanced the technology readiness level, demonstrating the accuracy and robustness of the proposed method, which is now deemed ready for commercial implementation.

A key requirement was to enable fleet-wide implementation and, therefore, ensure reliable operation throughout the entire service life of the wind turbines. The proposed method to measure dynamic mechanical torque is based on strain measurements of the static first-stage ring gear. Thus, this method applies to geared drivetrains with gearbox configurations with an epicyclic planetary input stage regardless of the number and topology of downstream stages. This gearbox configuration represents the majority of current and future commercial wind turbines.

The proposed method overcomes the limitation of traditional methods, which measure the strain of rotating components by measuring the stationary ring gear. Placing the sensors on a stationary component is a cost-effective alternative for serial implementation because the need for complex and expensive data transfer via wireless transmission or a slip ring is eliminated. Optical fiber strain sensors based on fiber Bragg gratings (FBGs) are proposed because of their advantages compared to electric resistance strain gauges, i.e., higher signal-to-noise ratio, immunity to electromagnetic interference, and allow a more straightforward installation because multiple strain sensors can be accommodated in a single fiber.

In Section 1.6, several research questions were formulated, and throughout this dissertation, subsequent scientific contributions have been presented to address these questions.

Research question 1: "Is the magnitude of the deformations on the outer surface of the ring gear within the sensing capabilities of commercial fiber-optic strain sensors?"

Chapter 2 presented the results from experiments conducted on a 6 MW wind turbine gearbox in which a total of 54 fiber-optic strain sensors were installed on the outer surface of the first stage ring gear. During the tests performed on a back-to-back gearbox test bench, the gear mesh forces between the planets and the ring gear were found to cause measurable deformations on the outer surface of the stationary ring gear well within the sensing capabilities of the FBGs. The findings in Chapter 3 and 4 have further validated this conclusion across three different gearboxes.

Research question 2: "How can the dynamic mechanical torque be quantified from the strain readings in discrete fiber-optic strain sensors distributed on the outer surface of the ring gear?"

The strain signals recorded in the experiments presented in Chapter 2 exhibited a dynamic behavior changing their values depending on the angular position of the planet carrier, the instantaneous variations of the input torque, and the load distribution between planets. Two signal processing strategies were presented to correlate the strain signals measured on the static ring gear with torque. The first strategy is based on the peak-to-peak strain values associated with the planet gear passage events. The second strategy

combines the strain signals from different sensors using a Coleman coordinate transformation and tracks the magnitude of the harmonic component corresponding to the number of planets. With the first strategy, torque can only be estimated when a planet passage is detected. In contrast, with the second strategy, it is possible to estimate torque whenever strain data of all sensors is available, leading to an improved frequency resolution up to the sampling frequency used to acquire strain data.

Research question 3: "Using the fiber-optic strain signals, can the periodic modes that describe the dynamic behavior of the gearbox be identified using data-driven methods?"

Chapter 3 presented an extended measurement setup comprising 129 fiber-optic strain sensors distributed around the ring gears of the three planetary stages of a state-of-the-art gearbox with a PPPH configuration. Operational deflection shapes were identified by applying the Multivariable Output-Error State-sPace (MOESP) subspace identification method to strain signals measured on a serial production end-of-line test bench. Under stationary torque and speed conditions, all identified eigenvalues and eigenvectors correspond to periodic excitations related to shaft rotations, planet passing, and gear mesh frequencies, and these excitations accounted for almost all the energy in the measured strain signals. The contribution of the deflection shapes produced by the passing of planets and their harmonics was found to be controlled by the amount of input torque applied to the gearbox. Using these contributions, an estimate of the input torque was demonstrated for dynamic operating conditions.

Research question 4: "How accurate are torque measurements taken by fiber-optic strain sensors in the ring gear?"

The findings of an extensive field experiment conducted on a 2 MW wind turbine at the National Renewable Energy Laboratory's Flatirons Campus to evaluate the accuracy of the torque measurement were presented in Chapter 4. The dynamic mechanical torque measurements from the fiber-optic strain sensors on the ring gear were compared to those derived from traditional strain gauges installed on the main shaft. For a load revolution distribution analysis, the average normalized root-mean-square error was below 0.7 %, which is very promising as it falls within the expected uncertainty of the traditional method to measure torque. Two different signal processing alternatives were compared, using peak-to-peak values associated with the planet passing events (Chapter 2) and a data-driven method that identifies operational deflection shapes (Chapter 3). Both methods resulted in very similar errors. However, the ODS method is preferred because it can provide a higher sampling frequency as the state associated with the ODSs can be evaluated at a rate as high as the sampling frequency. Additionally, the weighted P2P method encounters difficulty identifying the planet passage peaks at lower torque levels, which would be problematic for a potential real-time application.

Research question 5: "How do the turbine operating conditions affect the quality of the torque measurements? Especially what is the effect of speed fluctuations and non-torque loads, i.e. bending moments and thrust axial loads?"

The effect of operating conditions on the torque estimate was also investigated Chapter 4 for a wide range representative of the complete power curve of the turbine. The

highly variable speed operation of the turbine posed a key challenge when implementing the signal processing strategy based on identified operational deflection shapes because the periodicity requirement was violated without a constant rotor speed. This was restored by resampling the strain signals at fixed angular intervals of the rotor. In the angular domain, the system exhibits a periodic behavior and can be represented by the operational deflection shapes. The deflection shape associated with the third harmonic of the planet-passing frequency was found to be the least sensitive to nontorque load-related effects. In summary, no significant or consistent influence from wind speed, main-shaft bending moment, or temperature was observed.

Research question 6: "How accurate are mesh load factor results based on fiber-optic strain measurements on the outer surface of the ring gear compared to values obtained from strain gauge measurements in the gear teeth roots?"

The method to measure torque using fiber optic strain sensors on the outer surface of the ring gear relies on the deformations caused by the planet passages. By comparing the deformations caused by the different planets, it is feasible to evaluate the planet-load sharing behavior, which is quantified by the mesh load factor. Chapter 5 presented an experimental evaluation of the mesh load factor of a 6MW wind turbine gearbox with five planets in the first planetary stage. The fiber optical strain measurements in the outer surface of the ring gear yield equivalent mesh load factor K_γ results compared to the traditional method based on strain gauges located in the roots of the sun gear teeth. The results from both methods were significantly lower than the default values required in the standard "Design requirements for wind turbine gearboxes" IEC 61400-4. Since the mesh load factor is directly used for gear rating and sizing, a lower value allows a more optimized gearbox design, which significantly improves torque density and cost.

Research question 7: "If the number of strain sensors (FBGs) on the ring gear is selected as an integer multiple of the number of planets, can the mesh load factor be evaluated instantaneously?"

During the field validation campaign presented in Chapter 4 additional fiber-optic strain sensors were deployed on the 2-MW wind turbine gearbox with an enhanced spacing definition. By defining the number of sensors as an integer multiple of the number of planets, the findings presented in Chapter 6 demonstrate that it is feasible to evaluate the mesh load factor instantaneously from fiber-optic strain sensors placed on the outer surface of the static ring. The instantaneous mesh load factor was assessed across a wide range of operating conditions. The mesh load factor was found to be very low, consistent with the 4-point mount drivetrain configuration and three-planet input stage with a floating sun pinion. As expected, an increase in mesh load factor was observed for lower torques. The effect of other operating variables like wind turbulence intensity and yaw misalignment was found to be negligible.

7.2 Recommendations

The successful operation of the fiber-optic strain sensors during the test bench experiments and the field campaign presented in this dissertation has demonstrated a robust and accurate solution to measure dynamic mechanical torque ready for commercial fleet-wide implementation. This creates new avenues for future research, for which the following recommendations are given.

- The proposed commercial implementation of the method presented in this dissertation involves machining grooves on the outer surface of the ring gears, as detailed in Chapter 3. These grooves can be easily incorporated during the manufacturing process of the ring gears. This is the preferred solution because the grooves facilitate easier fiber installation and provide additional protection for the fiber-optic sensors. Additionally, the fiber-optic sensors and the optical interrogator should be installed during the gearbox assembly. This approach allows the system to be tested during the mandatory end-of-line test, where it can be calibrated against the test bench torque sensors. Consequently, each gearbox shipped for installation in a wind turbine would be equipped with a calibrated torque sensor, ready for operation as soon as the interrogator is powered.

- Having an accurate measurement of the input torque throughout the service history of every gearbox in a fleet would enable an improved assessment of the consumed fatigue life. This is important because the loading conditions are site-specific, and enabling an individual assessment of each gearbox can lead to better predictions of their remaining useful life and expected energy production. Having fleet-wide accurate mechanical torque measurements would significantly improve understanding of current gearbox failure modes. Some of these failure modes are not modeled in the industry and lack established design codes. Extensive research is needed to understand the effect of the torque fluctuations induced by dynamic wind turbine operations, particularly during high-load, damaging events such as emergency stops and low-voltage ride-throughs, to facilitate future design improvements, which would, in turn, lead to higher reliability and lower CoE.

- A better understanding of the effect of the torque fluctuations on the failure modes of wind turbine gearboxes coupled with the ability to measure torque reliably throughout the entire service life of the wind turbine enables a further research question: can drivetrain loading be improved using dynamic mechanical torque measurements from the fiber-optic sensors and novel data-driven control strategies? Such an outcome would significantly reduce the contribution of the wind turbine gearboxes to LCoE. This would require further development of the signal processing strategies that have been proposed in this dissertation to quantify dynamic mechanical torque to enable their real-time implementation.

- Assessing the consumed fatigue life of wind turbine gearboxes has attracted significant research interest recently to promote a change towards more efficient condition-based maintenance strategies. Current condition monitoring techniques are effective in detecting faults in the high-speed stages. However, detecting faults in the planetary stages is more challenging because of the complex transfer paths involved

in measuring signals associated with the faults and the low rotational speeds of these components. This dissertation proposes researching the high potential of using fiber-optic sensors for fault detection in planetary stages. Chapter 3 demonstrated how operational deflection shapes can be identified by applying data-driven methods to strain signals measured on the outer surface of the ring gear. We propose recursively identifying operational deflection shapes to track and trend their evolution over time to research if they can be used as an indicator for fault detection. Ideally, this topic should be investigated by seeding known faults in the planetary components, e.g., the journal bearings and planet gears, and evaluating their impact on the identified mode shapes. Additionally, two other avenues are suggested for future research to explore the condition monitoring potential of strain signals from fiber-optic sensors. Firstly, these sensors have been shown to capture high-frequency content, which may yield valuable indicators for fault detection. Secondly, the feasibility of evaluating the mesh load factor instantaneously was demonstrated in Chapter 6. Further research is recommended to investigate if faults in the planetary components, like wear in the planet gears or journal bearings, would manifest as changes in the mesh load factor.

- With the comprehensive instrumentation setup detailed in Chapter 3 and using signals from tests conducted under stationary torque and speed conditions, all identified eigenvalues and eigenvectors correspond to periodic excitations related to shaft rotations, planet passing, and gear mesh frequencies. The term “operational deflection shapes” (ODS) was selected for the observed part of the identified eigenvectors, as they are caused by periodic excitations and not a structural property of the gearbox. The research question remains whether structural modes can be identified by placing strain sensors in different locations and/or applying different loading conditions that could excite these structural modes.

Bibliography

References

[1] GWEC. Global wind report 2024. URL: https://https://gwec.net/global-wind-report-2024, 2024. Last accessed: 28 September 2024.

[2] GWEC. Global wind report: Annual market update 2013. URL: https://www.gwec.net/wp-content/uploads/2014/04/GWEC-Global-Wind-Report_9-April-2014.pdf, 2014. Last accessed: 28 September 2024.

[3] IRENA. International wind energy development: World market update. URL: https://www.irena.org/-/media/Files/IRENA/Agency/Publication/2013/GWEC/IRENA_GWEC_WindReport_Global-Wind-Market-Update.pdf, 2013. Last accessed: 23 May 2023.

[4] WindEurope. Wind energy in Europe: 2023 Statistics and the outlook for 2024-2030. URL: https://windeurope.org/intelligence-platform/product/wind-energy-in-europe-2023-statistics-and-the-outlook-for-2024-2030, 2024. Last accessed: 28 September 2024.

[5] Energy Institute Heriot-Watt University. Energy institute statistical review of world energy 2024. URL: https://www.energyinst.org/__data/assets/pdf_file/0006/1542714/684_EI_Stat_Review_V16_DIGITAL.pdf, 2024. Last accessed: 23 October 2024.

[6] IEA. Wind energy in europe: 2022 statistics and the outlook for 2023-2027. URL: https://www.iea.org/reports/net-zero-by-2050, 2023. Last accessed: 23 May 2023.

[7] G. A. M. van Kuik, J. Peinke, R. Nijssen, D. Lekou, J. Mann, J. N. Sørensen, C. Ferreira, J. W. van Wingerden, D. Schlipf, P. Gebraad, H. Polinder, A. Abrahamsen, G. J. W. van Bussel, J. D. Sørensen, P. Tavner, C. L. Bottasso, M. Muskulus, D. Matha, H. J. Lindeboom, S. Degraer, O. Kramer, S. Lehnhoff, M. Sonnenschein, P. E. Sørensen, R. W. Künneke, P. E. Morthorst, and K. Skytte. Long-term research challenges in wind energy - a research agenda by the european academy of wind energy. *Wind Energy Science*, 1(1): 1–39, feb 2016. DOI: 10.5194/wes-1-1-2016. URL: https://wes.copernicus.org/articles/1/1/2016/.

[8] W. Musial, P. Spitsen, P. Duffy, M. Beiter, P. Marquis, R. Hammond, and M. Shields. 2022 offshore wind market report. URL: https://www.energy.gov/sites/default/files/2022-09/offshore-wind-market-report-2022-v2.pdf, 2023. Last accessed: 23 May 2023.

[9] P. Veers, K. Dykes, E. Lantz, S. Barth, C. L. Bottasso, O. Carlson, A. Clifton, J. Green, P. Green, H. Holttinen, D. Laird, V. Lehtomäki, J. K. Lundquist, J. Manwell, M. Marquis, C. Meneveau, P. Moriarty, X. Munduate, M. Muskulus, J. Naughton, L. Pao, J. Paquette, J. Peinke, A. Robertson, J. Sanz Rodrigo, A. Maria Sempreviva, J. C. Smith, A. Tuohy, and R. Wiser. Grand challenges in the science of wind energy. *Science*, 366(6464): eaau2027, 2019. DOI: 10.1126/science.aau2027. URL: https://www.science.org/doi/abs/10.1126/science.aau2027.

[10] P. Veers, C. L. Bottasso, L. Manuel, J. Naughton, L. Pao, J. Paquette, A. Robertson, M. Robinson, S. Ananthan, T. Barlas, A. Bianchini, H. Bredmose, S. G. Horcas, J. Keller, H. A. Madsen, J. Manwell, P. Moriarty, S. Nolet, and J. Rinker. Grand challenges in the design, manufacture, and operation of future wind turbine systems. *Wind Energy Science*, 8(7): 1071–1131, 2023. DOI: 10.5194/wes-8-1071-2023. URL: https://wes.copernicus.org/articles/8/1071/2023/.

[11] M. Le Dain. Wind power companies struggle amid rapid industry growth. URL: https://www.forbes.com/sites/markledain/2023/06/25/wind-power-companies-struggle-amid-rapid-industry-growth, 2023. Last accessed: 29 September 2024.

[12] A. R. Nejad, J. Keller, Y. Guo, S. Sheng, H. Polinder, S. Watson, J. Dong, Z. Qin, A. Ebrahimi, R. Schelenz, F. Gutiérrez Guzmán, D. Cornel, R. Golafshan, G. Jacobs, B. Blockmans, J. Bosmans, B. Pluymers, J. Carroll, S. Koukoura, E. Hart, A. McDonald, A. Natarajan, J. Torsvik, F. K. Moghadam, P.-J. Daems, T. Verstraeten, C. Peeters, and J. Helsen. Wind turbine drivetrains: state-of-the-art technologies and future development trends. *Wind Energy Science*, 7(1): 387–411, 2022. DOI: 10.5194/wes-7-387-2022. URL: https://wes.copernicus.org/articles/7/387/2022.

[13] T. Stehly, P. Duffy, and D. Mulas Hernando. 2022 cost of wind energy review. Technical Report NREL/PR-5000-88335, National Renewable Energy Laboratory, 2023. URL: https://www.nrel.gov/docs/fy24osti/88335.pdf.

[14] H. Polinder, F.F.A. van der Pijl, G.-J. de Vilder, and P.J. Tavner. Comparison of direct-drive and geared generator concepts for wind turbines. *IEEE Transactions on Energy Conversion*, 21(3): 725–733, 2006. DOI: 10.1109/TEC.2006.875476. URL: https://ieeexplore.ieee.org/document/1677663.

[15] D. McMillan and G.W. Ault. Techno-economic comparison of operational aspects for direct drive and gearbox-driven wind turbines. *IEEE Transactions on Energy Conversion*, 25(1): 191–198, 2010. DOI: 10.1109/TEC.2009.2032596. URL: https://ieeexplore.ieee.org/document/5416624.

[16] H. Polinder, J.A. Ferreira, B.B. Jensen, A.B. Abrahamsen, K. Atallah, and R.A. McMahon. Trends in wind turbine generator systems. *IEEE Journal of Emerging and Selected Topics in Power Electronics*, 1(3): 174–185, 2013. DOI: 10.1109/JESTPE.2013.2280428. URL: https://ieeexplore.ieee.org/document/6588570.

[17] H. Arabian-Hoseynabadi, P. J. Tavner, and H. Oraee. Reliability comparison of direct-drive and geared-drive wind turbine concepts. *Wind Energy*, 13(1): 62–73, 2010. DOI: 10.1002/we.357. URL: https://onlinelibrary.wiley.com/doi/abs/10.1002/we.357.

[18] F. Harzendorf, R. Schelenz, and J. Georg. Method for holistic wind turbine drivetrain comparison exemplarily applied to geared and direct drive systems. *Forschung im Ingenieurwesen*, 86: 21–33, 2022. DOI: 10.1007/s10010-021-00564-w. URL: https://link.springer.com/article/10.1007/s10010-021-00564-w.

[19] A. Turnbull, C. McKinnon, J. Carrol, and A. McDonald. On the development of offshore wind turbine technology: An assessment of reliability rates and fault detection methods in a changing market. *Energies*, 15(9): 3180, 2022. DOI: 10.3390/en15093180. URL: https://www.mdpi.com/1996-1073/15/9/3180.

[20] G. Barter, L. Sethuraman, P. Bortolotti, J. Keller, and D.A. Torrey. Beyond 15 MW: A cost of energy perspective on the next generation of drivetrain technologies for offshore wind turbines. *Applied Energy*, 344: 121272, 2023. DOI: 10.1016/j.apenergy.2023.121272. URL: https://www.sciencedirect.com/science/article/pii/S0306261923006360.

[21] Wood Mackenzie. Global wind turbine technology trends 2023 market report. URL: https://www.woodmac.com/reports/power-markets-global-wind-turbine-technology-trends-2023-150187321, 2023. Last accessed: 11 October 2024.

[22] Bernd Bertsche. *Reliability in Automotive and Mechanical Engineering*. Springer Berlin, Heidelberg, 2008. ISBN 978-3-540-33969-4. DOI: 10.1007/978-3-540-34282-3. https://link.springer.com/book/10.1007/978-3-540-34282-3.

[23] J. Carroll, A. McDonald, and D. McMillan. Failure rate, repair time and unscheduled O&M cost analysis of offshore wind turbines. *Wind Energy*, 19(6): 1107–1119, 2016. DOI: 10.1002/we.1887. URL: https://onlinelibrary.wiley.com/doi/abs/10.1002/we.1887.

[24] T.N. Santel, C.M.R. de Oliveira, C.D. Maciel, and J.R.B. de A. Monteiro. Wind turbine failures review and trends. *Journal of Control, Automation and Electrical Systems*, 33 (2): 505–521, 2022. DOI: 10.1007/s40313-021-00789-8. URL: https://link.springer.com/article/10.1007/s40313-021-00789-8.

[25] E. Lantz. Operations expenditures: Historical trends and continuing challenges. Technical Report NREL/PR-6A20-58606, National Renewable Energy Laboratory, 2013. URL: https://www.nrel.gov/docs/fy13osti/58606.pdf.

[26] R.V. Pulikollu. Wind turbine reliability benchmarking to reduce O&M costs. *Drivetrain Reliability Collaborative Workshop*, 2023. URL: https://app.box.com/s/xti5nxixt4uwz2wtobqcvt7t1hgnmkb7.

[27] L. Haus, S. Sheng, and R.V. Pulikollu. Wind turbine major systems reliability trends and mitigation strategies. *Drivetrain Reliability Collaborative Workshop*, 2024. URL: https://app.box.com/s/75pdlad8731euyn2wkz26txse73vq3rp.

[28] J. Keller, Y. Guo, Z. Zhang, and D. Lucas. Comparison of planetary bearing load-sharing characteristics in wind turbine gearboxes. *Wind Energy Science*, 3(2): 947–960, 2018. DOI: 10.5194/wes-3-947-2018. URL: https://wes.copernicus.org/articles/3/947/2018.

[29] J. Keller. Gearbox reliability collaborative 1.5 (GRC1.5) project: Joint industry megawatt scale gearbox field tests. Technical Report NREL/TP-5000-81064, National Renewable Energy Laboratory, 2021. URL: https://www.nrel.gov/docs/fy21osti/81064.pdf.

[30] J. Keller. GRC1.5 project: Joint industry megawatt scale gearbox field tests. Technical Report NREL/TP-5000-88867, National Renewable Energy Laboratory, 2024. URL: https://www.nrel.gov/docs/fy24osti/88867.pdf.

[31] N.G. Demas, C. Lorenzo-Martin, R. Luna, R.A. Erck, and A.C. Greco. The effect of current and lambda on white-etch-crack failures. *Tribology International*, 189: 108951, 2023. DOI: 10.1016/j.triboint.2023.108951. URL: https://www.sciencedirect.com/science/article/pii/S0301679X23007399.

[32] Y. Guo, T. Parsons, R. King, K. Dykes, and P. Veers. Analytical formulation for sizing and estimating the dimensions and weight of wind turbine hub and drivetrain components. June 2015. DOI: 10.2172/1215033. URL: https://www.osti.gov/biblio/1215033.

[33] S. Tegen, E. Lantz, M. Hand, B. Maples, A. Smith, and P. Schwabe. 2011 cost of wind energy review. URL: https://www.nrel.gov/docs/fy13osti/56266.pdf, 2012. Last accessed: 23 May 2023.

[34] T. Stehly, D. Heimiller, and G. Scott. 2016 cost of wind energy review. Technical Report NREL/TP-6A20-70363, National Renewable Energy Laboratory, 2017. URL: https://www.nrel.gov/docs/fy18osti/70363.pdf. Last accessed: 23 May 2023.

[35] T. Stehly and P. Duffy. 2021 cost of wind energy review. Technical report, National Renewable Energy Laboratory, 2022. URL: https://www.nrel.gov/docs/fy23osti/84774.pdf. Last accessed: 23 May 2023.

[36] U. Gutierrez Santiago, A. A. W. van Vondelen, A. Fernández Sisón, H. Polinder, and J.W. van Wingerden. Identification of operational deflection shapes of a wind turbine gearbox using fiber-optic strain sensors on a serial production end-of-line test bench. *Wind Energy Science*, 10(1): 207–225, 2025. DOI: 10.5194/wes-10-207-2025. URL: https://wes.copernicus.org/articles/10/207/2025.

[37] ZF-Wind-Power. Zf wind power breaks 200 nm/kg torque density barrier with the modular gearbox platform shift 7k. URL: https://press.zf.com/press/en/releases/release_22016.html, 2020. Last accessed: 23 May 2023.

[38] Winergy. High density gear units winergy website. URL: https://www.winergy-group.com/en/Products/Gear-Units/High-Density/p/HighDensityX, 2020. Last accessed: 23 May 2023.

[39] Gamesa Gearbox. Torque density evolution. URL: https://www.gamesagearbox.com/wind-technology/, 2023. Last accessed: 23 Jan 2024.

[40] F. Oyague. Gearbox Reliability Collaborative (GRC) description and loading. Technical Report NREL/TP-5000-47773, National Renewable Energy Laboratory, 11 2011. URL: https://www.osti.gov/biblio/1030848.

[41] K. Dykes, P. Veers, E. Lantz, H. Holttinen, O. Carlson, A. Tuohy, A. Sempreviva, A. Clifton, J. Rodrigo, D. Berry, D. Laird, W. Carron, P. Moriarty, M. Marquis, C. Meneveau, J. Peinke, J. Paquette, N. Johnson, L. Pao, P. Fleming, C. Bottasso, V. Lehtomaki, A. Robertson, M. Muskulus, J. Manwell, J.O. Tande, L. Sethuraman, J. Roberts, and M. Fields. IEA Wind TCP: Results of IEA Wind TCP workshop on a grand vision for wind energy technology. Technical Report NREL/TP-5000-72437, National Renewable Energy Laboratory, April 2019. URL: https://www.osti.gov/biblio/1508509.

[42] J. Helsen, Y. Guo, J. Keller, and P. Guillaume. Experimental investigation of bearing slip in a wind turbine gearbox during a transient grid loss event. *Wind Energy*, 19 (12): 2255–2269, 2016. DOI: 10.1002/we.1979. URL: https://onlinelibrary.wiley.com/doi/abs/10.1002/we.1979.

[43] T. Egeling, E. Hidding, D. Hövelbrinks, N.and Endemann, M. Uhlending, R. Bonnet, P.and Dekkers, W. Hendicx, and W. Vandermeulen. Digital gearbox use case. 2018. URL: https://www.winergy-group.com/en/DigitalGearboxUseCase. Last accessed: 24 Nov 2021.

[44] J. Röder, G. Jacobs, T. Duda, D. Bosse, and F. Herzog. Investigation of dynamic loads in wind turbine drive trains due to grid and power converter faults. *Energies*, 14 (24): 8542, 2021. DOI: 10.3390/en14248542. URL: https://www.mdpi.com/1996-1073/14/24/8542.

[45] R. Santos and J. van Dam. Mechanical loads test report for the U.S. Department of Energy 1.5-Megawatt wind turbine. Technical Report NREL/TP-5000-63679, National Renewable Energy Laboratory, 2015. URL: https://www.nrel.gov/docs/fy15osti/63679.pdf.

[46] J. Rosinski and D. Smurthwaite. Troubleshooting wind gearbox problems. *Gear Solutions*, 2010. URL: https://gearsolutions.com/media/uploads/uploads/assets//PDF/Articles/Feb_10/0210_JRdynamics.pdf.

[47] N. Perišić, P. H. Kirkegaard, and B. J. Pedersen. Cost-effective shaft torque observer for condition monitoring of wind turbines. *Wind Energy*, 18(1): 1–19, 2015. DOI: 10.1002/we.1678. URL: https://onlinelibrary.wiley.com/doi/abs/10.1002/we.1678.

[48] B. Azzam, A. Baseer, R. Schelenz, and G. Jacobs. Development of a wind turbine gearbox virtual sensor using multibody simulation and artificial neural networks. *Forschung im Ingenieurwesen*, 85(1): 1–19, 06 2021. DOI: 10.1007/s10010-021-00460-3. URL: https://doi.org/10.1007/s10010-021-00460-3.

[49] C. Cappelle, M. Cattebeke, J. Bosmans, M. Kirchner, J. Croes, and W. Desmet. Sensor selection for cost-effective virtual torque measurements on a wind turbine gearbox. *Forschung im Ingenieurwesen*, 85: 325–334, 06 2021. DOI: 10.1007/s10010-021-00464-z. URL: https://link.springer.com/article/10.1007/s10010-021-00464-z.

[50] F. Mehlan, J. Keller, and A. R. Nejad. Virtual sensing of wind turbine hub loads and drivetrain fatigue damage. *Forschung im Ingenieurwesen*, 87: 207–218, 03 2023. DOI: 10.1007/s10010-023-00627-0. URL: https://link.springer.com/article/10.1007/s10010-023-00627-0.

[51] B. Mora, J. Basurko, I. Sabahi, U. Leturiondo, and J. Albizuri. Strain virtual sensing for structural health monitoring under variable loads. *Sensors*, 23(10): 4706, 2023. DOI: 10.3390/s23104706. URL: https://www.mdpi.com/1424-8220/23/10/4706.

[52] J. Bosmans, M. Kirchner, J. Croes, and W. Desmet. Validation of a wind turbine gearbox strain simulation model in service to virtual testing. *Forschung im Ingenieurwesen*, 87: 107–117, 2023. DOI: 10.1007/s10010-023-00635-0. URL: https://doi.org/10.1007/s10010-023-00635-0.

[53] J. Bosmans, S. Gallas, V. Smeets, M. Kirchner, L. Geens, J. Croes, and W. Desmet. Experimental validation of virtual torque sensing for wind turbine gearboxes based on strain measurements. *Wind Energy*, 28(2): e2955, 2025. DOI: 10.1002/we.2955. URL: https://onlinelibrary.wiley.com/doi/abs/10.1002/we.2955.

[54] Y. Guo and J. Keller. Validation of a generalized formulation for load-sharing behavior in epicyclic gears for wind turbines: Preprint. Technical Report NREL/CP-5000-76380, National Renewable Energy Laboratory, 2020. URL: https://www.osti.gov/biblio/1669557.

[55] A. Bodas and A. Kahraman. Influence of Carrier and Gear Manufacturing Errors on the Static Load Sharing Behavior of Planetary Gear Sets. *JSME International Journal Series C*, 47(3): 908–915, 2004. DOI: 10.1299/jsmec.47.908. URL: https://www.jstage.jst.go.jp/article/jsmec/47/3/47_3_908/_article.

[56] H. Ligata, A. Kahraman, and A. Singh. An Experimental Study of the Influence of Manufacturing Errors on the Planetary Gear Stresses and Planet Load Sharing. *Journal of Mechanical Design*, 130(4): 041701, 2008. DOI: 10.1115/1.2885194. URL: https://asmedigitalcollection.asme.org/mechanicaldesign/article-abstract/130/4/041701/461934/An-Experimental-Study-of-the-Influence-of?redirectedFrom=fulltext.

[57] A. Singh. Load sharing behavior in epicyclic gears: Physical explanation and generalized formulation. *Mechanism and Machine Theory*, 45(3): 511–530, 2010. DOI: 10.1016/j.mechmachtheory.2009.10.009. URL: https://www.sciencedirect.com/science/article/pii/S0094114X09001931.

[58] ISO 6336-1. Calculation of load capacity of spur and helical gears — Part 1: Basic principles, introduction and general influence factors. 2019. URL: https://www.iso.org/standard/63819.html.

[59] IEC 61400-4. Wind turbines — Part 4: Design requirements for wind turbine gearboxes. 2012. URL: https://www.iso.org/standard/44298.html.

[60] J. Calvo Irisarri, P. Olade Arce, U. Gutierrez Santiago, and A. Fernández Sisón. Load intensity distribution factor evaluation from strain gauges at the gear root. *Gear Solutions*, pages 42–51, 2021. URL: https://gearsolutions.com/features/load-intensity-distribution-factor-evaluation-from-strain-gauges-at-the-gear-root.

[61] W. Meeusen, W. Ceulemans, and M. Otto. Load distribution measurement on planetary gear systems. *International Conference on Gears FZG Munich*, October 2010.

[62] D. Daners and V. Nickel. More torque is better than torque, higher torque density for gearboxes. *Conference for wind power drives CWD*, 2021.

[63] M. Kreuzer. Strain measurement with fiber bragg grating sensors. *HBM*, 2006. URL: https://api.semanticscholar.org/CorpusID:5982070.

[64] L. Glavind, I. Olesen, B. Skipper, and M. Kristensen. Fiber-optical grating sensors for wind turbine blades: a review. *Optical Engineering*, 52(3): 1 – 10, 2013. DOI: 10.1117/1.OE.52.3.030901. URL: https://doi.org/10.1117/1.OE.52.3.030901.

[65] U. Gutierrez Santiago, A. Fernández Sisón, H. Polinder, and J.W. van Wingerden. Input torque measurements for wind turbine gearboxes using fiber-optic strain sensors. *Wind Energy Science*, 7(2): 505–521, 2022. DOI: 10.5194/wes-7-505-2022. URL: https://wes.copernicus.org/articles/7/505/2022.

[66] WindEurope. Wind energy in europe in 2018 - trends and statistics. URL: https://windeurope.org/intelligence-platform/product/wind-energy-in-europe-in-2018-trends-and-statistics, 2019. Last accessed: 30 April 2021.

[67] WindEurope. Wind energy in Europe 2020 - Statistics and the outlook for 2021-2025. URL: https://windeurope.org/intelligence-platform/product/wind-energy-in-europe-2020-statistics-and-the-outlook-for-2021-2025, 2021. Last accessed: 30 April 2021.

[68] G. A. M. van Kuik, J. Peinke, R. Nijssen, D. Lekou, J. Mann, J. N. Sørensen, C. Ferreira, J. W. van Wingerden, D. Schlipf, P. Gebraad, H. Polinder, A. Abrahamsen, G. J. W. van Bussel, J. D. Sørensen, P. Tavner, C. L. Bottasso, M. Muskulus, D. Matha, H. J. Lindeboom, S. Degraer, O. Kramer, S. Lehnhoff, M. Sonnenschein, P. E. Sørensen, R. W. Künneke, P. E. Morthorst, and K. Skytte. Long-term research challenges in wind energy - a research agenda by the european academy of wind energy. *Wind Energy Science*, 1(1): 1–39, 2016. DOI: 10.5194/wes-1-1-2016. URL: https://wes.copernicus.org/articles/1/1/2016.

[69] T. Stehly, P. Beiter, D. Heimiller, and G. Scott. 2017 cost of wind energy review. Technical report, National Renewable Energy Laboratory, 2018. URL: https://www.nrel.gov/docs/fy18osti/72167.pdf.

[70] F. Spinato, P.J. Tavner, G.J.W. van Bussel, and E. Koutoulakos. Reliability of wind turbine subassemblies. *IET Renewable Power Generation*, 3(4): 387–401, 2009. DOI: 10.1049/iet-rpg.2008.0060. URL: https://digital-library.theiet.org/doi/10.1049/iet-rpg.2008.0060.

[71] S. Sheng. Report on wind turbine subsystem reliability - a survey of various databases (presentation). Technical Report NREL/PR-5000-59111, National Renewable Energy Laboratory, 2013. URL: https://www.osti.gov/biblio/1090149.

[72] W. Musial, S. Butterfield, and B. McNiff. Improving wind turbine gearbox reliability. *European Wind Energy Conference Milan, Italy*, 2007.

[73] J. Helsen, F. Vanhollebeke, F. De Coninck, D. Vandepitte, and W. Desmet. Insights in wind turbine drive train dynamics gathered by validating advanced models on a newly developed 13.2 MW dynamically controlled test-rig. *Mechatronics*, 21(4): 737–752, 2011. DOI: 10.1016/j.mechatronics.2010.11.005. URL: https://www.sciencedirect.com/science/article/pii/S0957415810002059.

[74] S. Struggl, V. Berbyuk, and H. Johansson. Review on wind turbines with focus on drive train system dynamics. *Wind Energy*, 18(4): 567–590, 2015. DOI: 10.1002/we.1721. URL: https://onlinelibrary.wiley.com/doi/abs/10.1002/we.1721.

[75] I. Girsang, J. Dhupia, E. Muljadi, M. Singh, and L. Pao. Gearbox and drivetrain models to study dynamic effects of modern wind turbines. *IEEE Transactions on Industry Applications*, 50(6):3777–3786, 2014. DOI: 10.1109/TIA.2014.2321029. URL: https://ieeexplore.ieee.org/document/6807773.

[76] J. Peeters, D. Vandepitte, and P. Sas. Structural analysis of a wind turbine and its drive train using the flexible multibody simulation technique. *Proceedings of the International Conference on Noise and Vibration Engineering (ISMA2006)*, 2006.

[77] Y. Guo, J. Keller, Z. Zhang, and D. Lucas. Planetary Load Sharing in Three-Point-Mounted Wind Turbine Gearboxes: A Design and Test Comparison. Technical Report NREL/TP-5000-67394, National Renewable Energy Laboratory, 2017. URL: https://www.nrel.gov/docs/fy17osti/67394.pdf.

[78] H. Zhang, R. Ortiz de Luna, M. Pilas, and J. Wenske. A study of mechanical torque measurement on the wind turbine drive train — ways and feasibilities. *Wind Energy*, 21(12): 1406–1422, 2018. DOI: 10.1002/we.2263. URL: https://onlinelibrary.wiley.com/doi/epdf/10.1002/we.2263.

[79] DMT GmbH & Co. KG. URL: https://www.dmt-group.com/. Last accessed: 30 April 2021.

[80] Sensing 360 B.V. URL: https://sensing360.com. Last accessed: 30 April 2021.

[81] IEEE Standard for Information Technology - Portable Operating System Interface (POSIX(R)). *IEEE Std 1003.1-2008 (Revision of IEEE Std 1003.1-2004)*, pages 1–3874, 2008. DOI: 10.1109/IEEESTD.2008.4694976. URL: https://ieeexplore.ieee.org/document/4694976.

[82] W. Johnson. *Helicopter Theory*. Dover Publications, edition edition, 10 1994. ISBN ISBN 13: 9780486682303.

[83] G. Bir. Multiblade coordinate transformation and its application to wind turbine analysis: Preprint. Technical Report NREL/CP-500-42553, National Renewable Energy Laboratory, 2008. URL: https://www.osti.gov/biblio/922553.

[84] E. van Solingen and J.W. van Wingerden. Linear individual pitch control design for two-bladed wind turbines. *Wind Energy*, 18(4): 677–697, 2015. DOI: 10.1002/we.1720. URL: https://www.onlinelibrary.wiley.com/doi/abs/10.1002/we.1720.

[85] GWEC. Global wind report 2022. URL: https://gwec.net/global-wind-report-2022, 2023. Last accessed: 23 May 2023.

[86] U. Gutierrez Santiago, A. Fernández Sisón, H. Polinder, and J.W. van Wingerden. Input torque measurements for wind turbine gearboxes using fiber-optic strain sensors. *Wind Energy Science*, 7(2): 505–521, 2022. DOI: 10.5194/wes-7-505-2022. URL: https://wes.copernicus.org/articles/7/505/2022/.

[87] I. Bucher and D. Ewins. Modal analysis and testing of rotating structures. *Philosophical Transactions of the Royal Society of London. Series A: Mathematical, Physical and Engineering Sciences*, 359: 61–96, 2001. DOI: 10.1098/rsta.2000.0714. URL: https://royalsocietypublishing.org/doi/10.1098/rsta.2000.0714.

[88] H. Al-Khazali and M. Askari. System identification in rotating structures using vibration and modal analysis. In *Topics in Modal Analysis I, Volume 5. Proceedings of the 30th IMAC, A Conference on Structural Dynamics, 2012*, pages 481–497. Springer New York, 2012. ISBN 978-1-4614-2425-3. URL: https://link.springer.com/book/10.1007/978-1-4614-2425-3.

[89] L. Hermans and H. van der Auweraer. Modal testing and analysis of structures under operational conditions: Industrial applications. *Mechanical Systems and Signal Processing*, 13(2): 193–216, 1999. ISSN 0888-3270. DOI: https://doi.org/10.1006/mssp.1998.1211. URL: https://www.sciencedirect.com/science/article/pii/S0888327098912110.

[90] M. Ozbek, F. Meng, and D.J. Rixen. Challenges in testing and monitoring the in-operation vibration characteristics of wind turbines. *Mechanical Systems and Signal Processing*, 41(1): 649–666, 2013. DOI: 10.1016/j.ymssp.2013.07.023. URL: https://www.sciencedirect.com/science/article/pii/S0888327013003774.

[91] L. Thibault, T. Marinone, P. Avitabile, and C. Van Karsen. Comparison of modal parameters estimated from operational and experimental modal analysis approaches. In *Topics in Modal Analysis I, Volume 5*, pages 77–88. Springer New York, 2012. ISBN 978-1-4614-2425-3. URL: https://link.springer.com/book/10.1007/978-1-4614-2425-3.

[92] E Di Lorenzo. *Operational Modal Analysis for Rotating Machines: Challenges and Solutions*. PhD thesis, KU Leuven, University of Naples "Federico II", 2017. URL: http://www.fedoa.unina.it/id/eprint/11469.

[93] A. A. W. van Vondelen, S. T. Navalkar, A. Iliopoulos, D. C. van der Hoek, and J.W. van Wingerden. Damping identification of offshore wind turbines using operational modal analysis: a review. *Wind Energy Science*, 7(1): 161–184, 2022. DOI: 10.5194/wes-7-161-2022. URL: https://wes.copernicus.org/articles/7/161/2022/.

[94] M. Verhaegen and V. Verdult. *Filtering and system identification: a least squares approach*. Cambridge University Press, 2007. ISBN 9780511618888. DOI: 10.1017/CBO9780511618888. URL: https://www.cambridge.org/core/books/filtering-and-system-identification/D8589CB019CB233291427967DEE3EBE1.

[95] S. Greś, M. Döhler, P. Andersen, and L. Mevel. Kalman filter-based subspace identification for operational modal analysis under unmeasured periodic excitation. *Mechanical Systems and Signal Processing*, 146: 106996, 2021. DOI: 10.1016/j.ymssp.2020.106996. URL: https://www.sciencedirect.com/science/article/pii/S0888327020303824.

[96] A.A. W. van Vondelen, A. Iliopoulos, S. Navalkar, D. van der Hoek, and J.W. van Wingerden. Modal analysis of an operational offshore wind turbine using enhanced Kalman filter-based subspace identification. *Wind Energy*, 26(9): 923–945, 2023. DOI: 10.1002/we.2849. URL: https://onlinelibrary.wiley.com/doi/abs/10.1002/we.2849.

[97] M. Verhaegen and P. Dewilde. Subspace model identification part 1. the output-error state-space model identification class of algorithms. *International Journal of Control*, 56(5): 1187–1210, 1992. DOI: 10.1080/00207179208934363. URL: https://www.tandfonline.com/doi/abs/10.1080/00207179208934363.

[98] I. Houtzager. LTI System Identification Toolbox (Version 2.4). URL: https://www.dcsc.tudelft.nl/~jwvanwingerden/lti/ltitoolbox_product_page.html, 2012.

[99] U. Gutierrez Santiago. Video supplements, accompanying publication: Identification of operational deflection shapes of a wind turbine gearbox using fiber-optic strain sensors on a serial production end-of-line test bench, 2024. URL: https://data.4tu.nl/datasets/3761b933-b61a-4474-8492-9840cc70ed15.

[100] U. Gutierrez Santiago, J. Keller, A. Fernández Sisón, H. Polinder, and J.W. van Wingerden. Field validation of dynamic mechanical torque measurements using fiber-optic strain sensors for geared wind turbines. *Forschung im Ingenieurwesen*, paper accepted, awaiting publication: Preprint available in. URL: https://app.box.com/s/8s694zfcyw83k821vmov0y8cjigi8919.

[101] M.O. Siddiqui, P.R. Feja, P.B., H. Kyling, A.R. Nejad, and J. Wenske. Wind turbine nacelle testing: State-of-the-art and development trends. *Renewable and Sustainable Energy Reviews*, 188: 113767, 2023. DOI: 10.1016/j.rser.2023.113767. URL: https://www.sciencedirect.com/science/article/pii/S136403212300624X.

[102] U. Gutierrez-Santiago, J. Keller, A. Fernández Sisón, H. Polinder, and J.W. van Wingerden. Instantaneous mesh load factor (Kγ) measurements in a wind turbine gearbox using fiber-optic strain sensors. *Journal of Physics: Conference Series*, 2767: 042022, 2024. DOI: 10.1088/1742-6596/2767/4/042022. URL: https://iopscience.iop.org/article/10.1088/1742-6596/2767/4/042022.

[103] N. Riccobono, N. Danigelis, J. Keller, and U. Gutierrez-Santiago. Investigating main shaft loading in OpenFAST for a Gamesa G97-2MW wind turbine. Technical Report NREL/TP-5000-91332, National Renewable Energy Laboratory, 2024. URL: https://www.nrel.gov/docs/fy25osti/91332.pdf.

[104] M. Verhaegen, V. Verdult, and N. Bergboer. *Filtering and System Identification: An Introduction to using Matlab Software*. Delft University of Technology, 2007. URL: https://www.dcsc.tudelft.nl/~jwvanwingerden/lti/doc/companion.pdf.

[105] U. Gutierrez Santiago. Video supplements, accompanying publication: Field validation of dynamic mechanical torque measurements using fiber-optic strain sensors for geared wind turbines, 2025. URL: https://data.4tu.nl/datasets/10.4121/a03650e2-146d-4426-bb5d-61ce92d23bbd.

[106] T. Chai and R. R. Draxler. Root mean square error (RMSE) or mean absolute error (MAE)? – Arguments against avoiding RMSE in the literature. *Geoscientific Model Development*, 7(3): 1247–1250, 2014. DOI: 10.5194/gmd-7-1247-2014. URL: https://gmd.copernicus.org/articles/7/1247/2014/.

[107] A Krause, G Jacobs, J Röder, M. Zweiffel, and J Roth. Deviation of drive torque and rotational speed of a wind turbine drivetrain between test bench and wind turbine simulations. *Journal of Physics: Conference Series*, 2767(4): 042013, 2024. DOI: 10.1088/1742-6596/2767/4/042013. URL: https://iopscience.iop.org/article/10.1088/1742-6596/2767/4/042013.

[108] U. Gutierrez Santiago, A. Fernández Sisón, H. Polinder, and J.W. van Wingerden. Experimental evaluation of the mesh load factor ($K\gamma$) of a 6 MW wind turbine gearbox. *Journal of Physics: Conference Series*, 2265(3): 032003, 2022. DOI: 10.1088/1742-6596/2265/3/032003. URL: https://iopscience.iop.org/article/10.1088/1742-6596/2265/3/032003.

[109] Jonathan C. Lansey. Beautiful and distinguishable line colors + colormap, 2015. URL: https://www.mathworks.com/matlabcentral/fileexchange/42673-beautiful-and-distinguishable-line-colors-colormap.

[110] Fabio Crameri. Scientific colour maps, 2019. URL: https://zenodo.org/record/1243862.

Glossary

AGMA American Gear Manufacturers Association.

DFIG Doubly-Fed Induction Generator.

EMA Experimental Modal Analysis.

FGB Fiber Bragg Grating.

FOS Fiber-Optic Sensor.

GET Gamesa Energy Transmission.

GMF Gear Mesh Frequency.

GPS Global Positioning System.

GRC Gearbox Reliability Collaborative.

GWEC Global Wind Energy Council.

HSS High-Speed Shaft.

IEA International Energy Agency.

IEC International Electrotechnical Commission.

IRENA International Renewable Energy Agency.

ISO International Organization for Standardization.

LCoE Levelized Cost of Energy.

LDD Load Duration Distribution.

LRD Load Revolution Distribution.

LSS Low-Speed Shaft.

MBC Multi-Blade Coordinate Transformation.

MOESP Multivariable Output-Error State-Space subspace identification method.

NREL National Renewable Energy Laboratory.

O&M Operations and Maintenance.

ODS Operational Deflection Shape.

OMA Operational Modal Analysis.

P2P Peak-to-Peak.

PC Planet Carrier.

PMSG Permanent-Magnet Synchronous Generator.

POSIX Portable Operating System Interface.

PV Photovoltaic.

RMSE Root-Mean-Square Error.

SCADA Supervisory Control and Data Acquisition.

SGRE Siemens Gamesa Renewable Energy.

TRL Technology Readiness Level.

UTC Coordinated Universal Time.

VAF Variance Accounted For.

Curriculum Vitæ

Unai Gutierrez Santiago

1979/05/08	Date of birth in Getxo, Spain

Education

1997 - 2002	Ingeniero Industrial, Euskal Herriko Unibertsitatea, Spain
2003	Tribology course, University of Cambridge, United Kingdom
2004	Gear Design, University of Cranfield, United Kingdom
2011	Vibration Analyst ISO 18436 Cat.3, Prüftechnik - Mobius Institute, Ismaning, Germany
2014	Gear dynamics and gear noise short course, The Ohio State University, USA
2018 - 2025	Doctor of Philosophy in Mechanical Engineering Delft University of Technology, The Netherlands *Dissertation*: Measuring dynamic mechanical torque with fiber-optic sensors for geared wind turbines *Promotors*: prof. dr. ir. Jan-Willem van Wingerden and dr. ir. Henk Polinder

Career history

2001 - 2002	Mechanical process engineer, Aula Robotiker, Spain
2003 - 2006	Technical service engineer, Victrex Plc, United Kingdom
2006 - 2025	Gearbox validation section lead, Siemens Gamesa Renewable Energy, Spain

List of Publications

1. U. Gutierrez Santiago, A. Fernández Sisón, H. Polinder, and J.W. van Wingerden. Torque measurements from MW wind turbine gearboxes: a system identification approach. *Journal of Physics: Conference Series*, 1618(2) 022027, 2020. DOI: 10.1088/1742-6596/1618/2/022027. URL: https://iopscience.iop.org/article/10.1088/1742-6596/1618/2/022027.

2. Gutierrez Santiago, U., Fernández Sisón, A., Polinder, H., and J.W van Wingerden.Input torque measurements for wind turbine gearboxes using fiber-optic strain sensors, *Wind Energy Science*, 7(2):505–521, 2022. DOI: 10.5194/wes-7-505-2022. URL: https://wes.copernicus.org/articles/7/505/2022/.

3. U. Gutierrez Santiago, A. Fernández Sisón, H. Polinder, and J.W. van Wingerden. Experimental evaluation of the mesh load factor (Kγ) of a 6 MW wind turbine gearbox. *Journal of Physics: Conference Series*, 2265(3): 032003, 2022. DOI: 10.1088/1742-6596/2265/3/032003. URL: https://iopscience.iop.org/article/10.1088/1742-6596/2265/3/032003.

4. U. Gutierrez Santiago, A., Fernández Sisón, H., Polinder, and J.W. van Wingerden. Experimental evaluation of wind turbine gearbox structural models using fiber optic strain sensors. *Gear Technology*, October: 44-51, 2023. URL: https://www.geartechnology.com/articles/30495-experimental-evaluation-of-wind-turbine-gearbox-structural-models-using-fiber-optic-strain-sensors.

5. U. Gutierrez Santiago, A.A.W. van Vondelen, A. Fernández Sisón, H. Polinder, and J.W. van Wingerden. Identification of operational deflection shapes of a wind turbine gearbox using fiber-optic strain sensors on a serial production end-of-line test bench. *Wind Energy Science*, 10(1):207–225, 2025. DOI: 10.5194/wes-10-207-2025. URL: https://wes.copernicus.org/articles/10/207/2025/.

6. U. Gutierrez Santiago, J. Keller, A. Fernández Sisón, H. Polinder, and J.W. van Wingerden. Instantaneous mesh load factor (Kγ) measurements in a wind turbine gearbox using fiber-optic strain sensors. *Journal of Physics: Conference Series*, 2767: 042022, 2024. DOI: 10.1088/1742-6596/2767/4/042022. URL: https://iopscience.iop.org/article/10.1088/1742-6596/2767/4/042022.

7. U. Gutierrez Santiago, J. Keller, A. Fernández Sisón, H. Polinder, and J.W. van Wingerden. Field validation of dynamic mechanical torque measurements using fiber-optic strain sensors for geared wind turbines. Accepted for publication in *Forschung im Ingenieurwesen*, preprint available in https://app.box.com/s/8s694zfcyw83k821vmov0y8cjigi8919.

Included in this thesis.

Propositions

accompanying the dissertation

Measuring dynamic mechanical torque with fiber-optic sensors for geared wind turbines

by

Unai Gutierrez Santiago

1. In wind turbine gearboxes, the first stage ring gear has a relatively thin rim. Measuring torque from strain measurements of the static ring gear is more attractive than from strain in the main shaft (this thesis).

2. When wind turbine gearboxes are designed properly, harmonic excitations dominate the power spectrum of the strain signals from fiber-optic sensors placed on the ring gear. Under these conditions, quantifying dynamic mechanical torque based on data-driven methods is more advantageous than doing so based on physical principles (this thesis).

3. Wind turbines have a highly variable speed operation, which makes their behavior fail to comply with the periodicity requirement imposed by the method based on operational deflection shapes. Because gearboxes fulfill the linear time-invariant assumptions under normal operating conditions, the periodicity can be easily recovered by resampling the signals using fixed angular intervals defined from the rotor azimuth angle (this thesis).

4. As turbines grow larger, the cost and value of the gearboxes will increase. Meanwhile, technological developments are driving the cost of fiber-optic sensing down. Soon, it will be reckless not to monitor the mechanical torque of geared drivetrain using fiber-optic sensors.

5. Gearboxes in wind turbines are prone to failure due to the combination of the limitless power of the wind and the unfavorable inertial difference between the driving rotor and the driven generator. Successful operation is only possible through appropriate control actions.

6. Excessive focus on reducing the levelized cost of energy (LCoE) has led many wind turbine manufacturers into unsustainable financial situations. A paradigm change is needed that emphasizes increasing the value added to society rather than reducing the costs.

7. Imposing the same design life requirements on the drivetrain as on structural elements, such as the foundation and tower, is unrealistic and counterproductive.

8. Reducing carbon emissions is a necessary step but not sufficient. We should put at least the same amount of effort into restoring natural habitats. An added tariff for nonrenewable energy sources should be introduced to finance rewilding the planet.

9. Some European countries, like Spain, France and Germany, have started classifying vehicles based on their environmental impact and are issuing so-called emission badges. Because of their disproportionate manufacturing footprint, sport utility vehicles (SUVs) should never be awarded an eco-badge.

10. Usain Bolt is considered to be the greatest sprinter of all time and the fastest man on earth. In the Netherlands, "Sprinter" trains are slower than "Intercity" trains. This is a gross act of misleading advertisement from Nederlandse Spoorwegen (NS), who needs to change the name of their trains immediately.

These propositions are regarded as opposable and defendable, and have been approved as such by the promotors prof. dr. ir. J.W. van Wingerden and Dr. ir. H. Polinder.